KINETIC MONTE CARLO SIMULATIONS OF DEFECT EVOLUTION IN MATERIALS UNDER IRRADIATION BY ENERGETIC PARTICLES

A Thesis
Presented to
The Academic Faculty

by

Richard T. Hoffman III

In Partial Fulfillment
of the Requirements for the Degree
Doctor of Philosophy in the
Nuclear and Radiological Engineering Program
George W. Woodruff School of Mechanical Engineering

Georgia Institute of Technology
December 2016

KINETIC MONTE CARLO SIMULATIONS OF DEFECT EVOLUTION IN MATERIALS UNDER IRRADIATION BY ENERGETIC PARTICLES

Approved by:

Professor Chaitanya Deo, Advisor
Nuclear and Radiological Engineering Program
George W. Woodruff School of Mechanical Engineering
Georgia Institute of Technology

Professor Hamid Garmestani
School of Materials Science and Engineering
Georgia Institute of Technology

Professor David McDowell
George W. Woodruff School of Mechanical Engineering
Georgia Institute of Technology

Professor Yan Wang
George W. Woodruff School of Mechanical Engineering
Georgia Institute of Technology

Professor Bojan Petrovic
Nuclear and Radiological Engineering Program
George W. Woodruff School of Mechanical Engineering
Georgia Institute of Technology

Date Approved: 10 November 2016

To my wife and children,

Di Wu, Jeni A. Hoffman, and Rachael Y. Hoffman

without whom none of this would be possible.

ACKNOWLEDGEMENTS

I would like to express my appreciation and thanks to my advisor Professor Chaitanya Deo. I would like to thank you for your help and encouragement in completing my research. Your advice and guidance has been valuable.

I would like to thank the remaining members of my committee, Professor David McDowell, Professor Bojan Petrovic, Professor Hamid Garmestani, and Professor Yan Wang, for serving on my committee and for providing valuable guidance and input.

I would also like to thank all of my group members and fellow graduate students, who have provided me with tremendous help, support, and friendship during my time at Georgia Tech. Thank you for your support and generally putting up with me for this time.

Finally, I would like to thank my family who have helped me through the tough times and kept me focused on my goal. I would not have been able to complete this without you.

TABLE OF CONTENTS

LIST OF TABLES

LIST OF FIGURES

SUMMARY

Examination of the materials used in nuclear reactors is one of the most pressing issues of current nuclear engineering research. One of the primary focuses of research into Generation IV reactors and work to extend the life of today's commercial plants is developing new materials and examining the ability of currents materials to handle the harsh radiation environments found in nuclear reactors. These materials interact with their environment on an atomic scale, however, the properties important to choosing the right materials for an application are often seen on a continuum scale. Kinetic Monte Carlo (kMC) is a computationally intensive but extremely powerful tool for bridging the gap between these scales.

Five kMC simulations have been developed within the SPPARKS framework for use with different applications related to nuclear and energy materials. The behavior of each of the models was examined and compared to relevant literature or other methods of modeling where available. The models are based on three of the built in simplistic models available in SPPARKS, diffusion, Potts, and chemistry, and required extensive modification of the original code.

The first of the models created examines the diffusion behavior of vacancies in a doped fluorite lattice. The goal of this study was to examine the behavior of the diffusivity and ionic conductivity as well as examine the behavior of vacancy-dopant pairs across a wide range of dopant atoms.

In the second model, the behavior of defects in bcc metals was examined. In particular we examined the effect of increasingly complex vacancy clusters on the resulting defect concentrations using both kMC simulations and rate equations.

In the third simulation, a Potts model is developed to examine the evolution of gas bubbles and HBS formation in nuclear fuels. The model examines the behavior of the lattice constant under irradiation and the HBS formation over local burnups in the outer region of the fuel pellet consistent with use in a nuclear reactor.

The final two models that have been developed examines the formation of nanoporous materials through a dealloying process and combine cluster dynamics with the kMC algorithm in a method known as stochastic cluster dynamics to examine defect behavior on a larger scale.

Additionally sensitivity analysis was performed on three of the models in order to examine which of the input parameters are most important in the output of the simulation. Two types of sensitivity analysis were performed on the simulations. The first, MOAT examines changes in one parameter at a time while keeping the other parameters constant but performs this in an efficient manner that is known to approximate a global sensitivity analysis. The second, PRCC uses LHS which is an efficient method of sampling the input parameter space in order to rank each of the input parameters based on the importance of the parameter in determining the resulting outcome variable.

CHAPTER I

INTRODUCTION

1.1 kinetic Monte Carlo

Examination of the materials used in nuclear reactors is one of the most pressing issues of current nuclear engineering research. One of the primary focuses of research into Generation IV reactors and work to extend the life of today's commercial plants is developing new materials and examining the ability of currents materials to handle the harsh radiation environments found in nuclear reactors. These materials interact with their environment on an atomic scale, however, the properties important to choosing the right materials for an application are often seen on a continuum scale. Kinetic Monte Carlo (kMC) is a computationally intensive but extremely powerful tool for bridging the gap between these scales (figure 1).

The basis for using kMC is the fact that in general the fundamental processes and mechanisms observed in nature often appear to behave stochastically. Thus, with an appropriate deterministic equation stochastic phenomenon when viewed within a statistically large sample can yield deterministic results. In simple cases this behavior may be described analytically but more often approximations must be made to arrive at an analytical solution. KMC is often the only method for producing solutions with the minimum approximations necessary.

In this work we create 3 models using the SPPARKS [144] code for materials used in nuclear reactors and examine the sensitivity of the input parameters on the output parameters in each of these models. The models examine two types of applications that kMC has successfully been applied to in the past, diffusivity and grain growth,

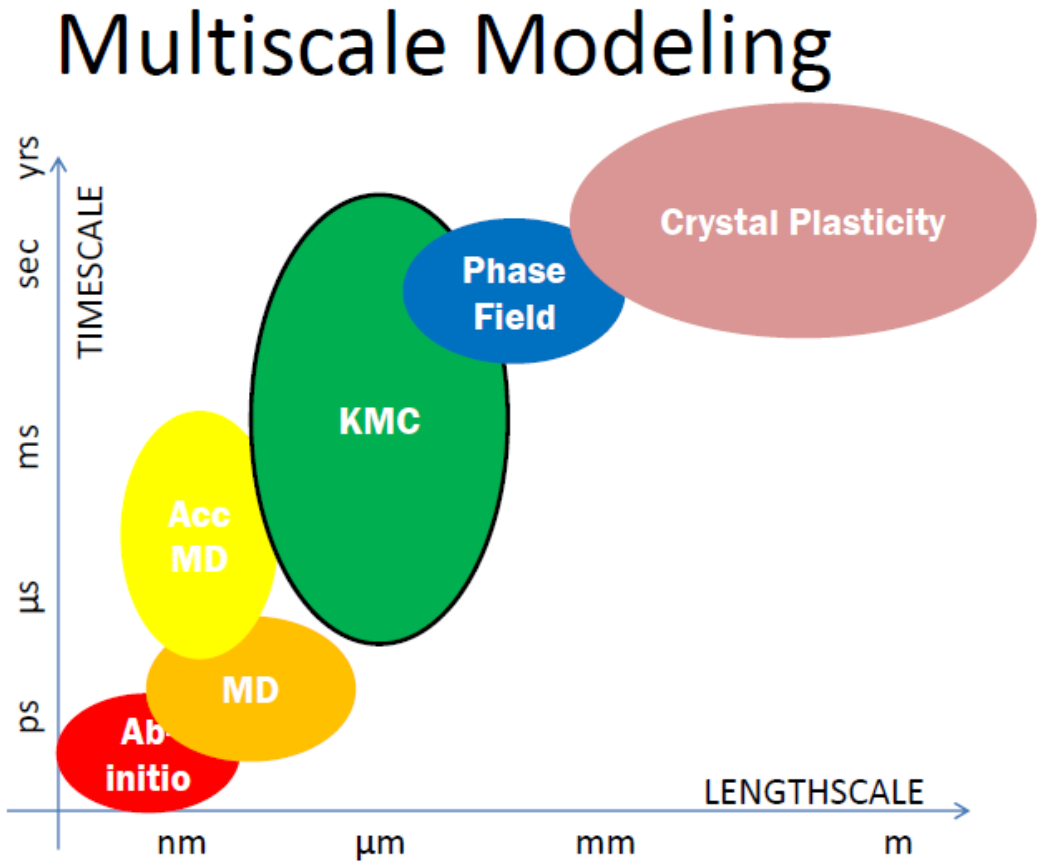

Figure 1: The types of models available at different length and time scales for simulation of nuclear materials.

using different methods. In addition, two models are presented that have been developed but have not had sensitivity analysis performed on them. The first of these models, examines the behavior of the formation of nanoporous foams. The second, examines a method that relies on the kMC algorithm but seeks to combine kMC with rate theory by reformulating cluster dynamics in a stochastic manner.

1.1.1 History

Since the introduction of the Monte Carlo method in 1946 it has been used to describe a large array of scientific problems. In 1953 Metropolis *et al.* [121] introduced an improvement to the modeling scheme which would become known as Metropolis Monte Carlo and form the basis for the rejection based algorithm available in SPPARKS. The original n-fold algorithm was introduced by Bortz, Kalos, and Lebowitz[27] and became the basis for the most common kMC algorithm. It was also the first method to introduce a stochastic method for the time incrementation, allowing for the measurement of time directly through rates instead of as an interpretation of the number of steps performed. This method was independently discovered by Gillespie[59] and has since been updated by Voter[194]. It has since been applied to a range of materials applications.

1.1.2 SPPARKS

SPPARKS is an open source parallel kMC code written and maintained by Plimpton *et al.* at Sandia National Labs. It is written in the C++ programming language and is therefore object oriented. SPPARKS is primarily meant to be used in on-lattice applications, although it does have off-lattice applications and one of the general applications (independent of spatial positioning) has been modified in this work and presented in the other model section (Section 6.2). In addition, it uses the message passing interface (MPI) to allow for parallelization of the lattice through the use of sublattices.

The code can be split into four groups of features (application styles, diagnostic styles, input script commands and solve styles) that may be updated by users in addition to the core components that drive the code. In general when creating new applications the application style and input script commands were the primary components of code that needed modification. For instance in each of the applications created for this work one of the basic application styles, i.e. diffusion, Potts, or chemical reactions, was modified to fit the particular parameters of the simulation. Due to the object oriented nature of C++ a new application is a class object that is then able to interact with the other objects with minimal modification of the original code. Thus, it is simple to modify and extend SPPARKS to fit new applications.

1.2 Sensitivity Analysis

Sensitivity analysis of models can be used to determine the most important input parameters when designing a simulation and thus direct studies in which parameters should be most accurately examined and refined. For example, sensitivity analysis has been used to prioritize data collection and research by identifying the important uncertainties[43]. In addition, sensitivity analysis has been used to examine the robustness of model results when making decisions [143, 199, 110, 112]. When going through the process of model development and refinement sensitivity analysis can play a role in model validation [96, 97, 53]. These methods have been applied across a variety of different fields [137, 8, 39, 17, 1, 89, 120, 40] and have been used in relation to nuclear and radiological engineering [75, 76, 77] and kinetic Monte Carlo [145, 6].

The method for performing sensitivity analysis is widely varied with more then ten different methods that have been studied in-depth [71]. The particular method chosen will depend on the complexity of the model both in terms of the number of input parameters and the computational time required to run the simulation, the monotonicity of the solution, and dependence of the input parameters on one another.

Therefore, in this study we attempt to present several forms of sensitivity analysis for each model studied without an attempt to judge which method is best suited for the particular model.

The first, the Morris One at a Time (MOAT) method is a modification of the simplest method of one at a time sensitivity analysis. It was proposed by Morris [130] in 1991 as a screening method through the use of Elementary Effects (EE), which measure the importance of a variable, and performs a group of one at a time analyses in order to present a hybridized version of local sensitivity analysis, which is more efficient [171] and can be considered as an approximation of a global sensitivity analysis [197].

The second method we use is a combination of Latin Hypercube Sampling (LHS), which is a method for choosing random values, for the input parameters introduced by McKay *et al.* [111] and Partial Rank Correlation Coefficient (PRCC) [82] which is a powerful method of sensitivity analysis. LHS presents an efficient tool to explore the entirety of the parameter space with a minimum number of computer simulations. PRCC is best suited for nonlinear relationships between the input parameters and the output which is vital when applied to the models presented in this work.

CHAPTER II

METHODOLOGY

2.1 kinetic Monte Carlo

2.1.1 n-fold method

For many applications the most efficient algorithm for evolving the system is a rejection free form of kMC. These methods are a modification of the n-fold way algorithm [27]. The modified version of this algorithm used by the simulation is given in table 1. The advantage of this method is that if the likelihood of events is varied, time is not wasted attempting to perform the low likelihood events, instead each event that is chosen occurs and the system is able to evolve efficiently. In addition, the time for each event can be calculated directly and does not need to be inferred. In this method for each event that can occur, a rate constant is computed [195]:

$$r_i = \nu_i e^{-\frac{\Delta Q}{k_B T}} \tag{1}$$

Where ΔQ is the change in energy of the system, k_B is Boltzmann's constant and T is the temperature of the system. In order to evolve the system a list of all events is compiled. Next, an event is chosen randomly from the list of possible events based on the probability of each individual event being chosen. In particular if there is M events and the mth event is chosen. The formula for calculating m is given by[16]:

$$\frac{\sum_{i=0}^{m-1} r_i}{\sum_{i=0}^{M} r_i} < \xi_1 < \frac{\sum_{i=0}^{m} r_i}{\sum_{i=0}^{M} r_i} \tag{2}$$

Table 1: General kMC algorithm used in simulations. Note that the addition of step 5 and step 6 are improvements on the original kMC method.

Step	Procedure
Step 0	Set the time $t = 0$
Step 1	Form a list of all the possible events at an individual site r_i
Step 2	Calculate the cumulative function $$R_N = \sum_{i=1}^{N} r_i$$ where N is the total number of sites
Step 3	Get a uniform random number $\mu \in [0, 1]$
Step 4	Find the site to perform an event r_i where: $$r_{i-1} < \mu R_N \leq r_i$$
Step 5	Choose an event on site i using a similar procedure to Step 4 and perform the event
Step 6	Recalculate all r_i that may have changed
Step 7	Get a new uniform random number $\mu \in [0, 1]$
Step 8	Update the time by adding: $$\Delta t = \frac{-log\mu}{R_N}$$
Step 9	Repeat from Step 2

Where r_i is event i's rate of occurrence and ξ_1 is a random number generated over the range [0,1). After the event is chosen it is performed, the time is advanced, and the list of events is updated appropriately. This process is repeated for a set simulation time or number of simulation steps. The time associated with each event is dynamic and stochastic and is based on the formula:

$$dt = -ln(\xi_2) \sum_{i=1}^{M} r_i \tag{3}$$

Where ξ_2 is a random number distributed uniformly from (0,1). An in depth explanation of how this formula is derived can be found in the literature[27, 16], an abbreviated form is given here.

In traditional kMC methods the system is sampled at regular time intervals and the time intervals are chosen so that only one or zero events has occurred in the time range, thus the timestep is limited by the most frequent event. Instead the method employed in this work determines the time increment since the last event occured, which is especially useful given the wide range of migration barriers which leads to a wide range of time steps over which events occur. In order to determine this time value we examine the probability no event occurs during a time $\Delta t + dt$, which is equivalent to the probability no event occurs during Δt and no event occurs during the following dt,

$$P(\Delta t + dt) = P(\Delta t)(1 - \Pi dt) \tag{4}$$

This can be rewritten as the differential equation,

$$\frac{dP}{dt} = -P(\Delta t)\Pi \tag{5}$$

which with the appropriate boundary conditions has the solution,

$$P(\Delta t) = \exp(-\Pi \Delta t) \tag{6}$$

If this equation is solved for Δt and the probability $P(\Delta t)$ is assigned a random probability this becomes analogous to the time value we used above.

2.1.2 rejection kMC

In particular applications the use of a rejection kMC algorithm is more common and potentially more efficient. The advantage of this method is that the simulation is evolved quickly if the probability of a state change is likely. However, it does not have a direct time component and thus the time is often described only as the number of steps, Monte Carlo Steps (MCS) taken by the simulation and cannot be compared directly to experimental times. In this method the probability of an event occurring is given by[78]:

$$P_i = \begin{cases} 1 & \text{if } \Delta E \leq 0 \\ e^{-\frac{\Delta E}{k_B T}} & \text{if } \Delta E > 0 \end{cases} \tag{7}$$

Where ΔE is the change in energy of the system, k_B is Boltzmann's constant and T is the temperature of the system. In order to evolve the system a loop is performed over each of the sites on which an event can occur. At each site an event is attempted with the probability calculated for the event. The probability is then compared to a random number $[0, 1)$ and accepted if the probability is larger than the random number. After a full cycle though all possible sites the time is incremented by 1/Q MCS where Q is the number of possible states for the system. The general algorithm for this method is given in table 2.

Table 2: General rkMC algorithm used in simulations. Note that the time is calculated only based on the number of possible states and the number of steps taken.

Step	Procedure
Step 0	Set the time $t = 0$
Step 1	Choose a site to attempt an event
Step 2	Calculate the probability the event will occur $$P_i = \begin{cases} 1 & \text{if } \Delta E \leq 0 \\ e^{-\frac{\Delta E}{k_B T}} & \text{if } \Delta E > 0 \end{cases}$$
Step 3	Get a uniform random number $\mu \in [0, 1)$ and accept the even if $P_i > \mu$
Step 4	Repeat from Step 1 until all sites have been chosen
Step 5	Update the time by adding: $1/Q$ MCS
Step 6	Repeat from Step 1

2.2 Sensitivity Analysis

2.2.1 Morris One at a Time Method

We use Morris One at a time sensitivity analysis[130, 197]. This method creates a series of Elementary Effects (EE) which are a measure of the importance of each of the parameters:

$$EE_i(x) = \frac{1}{\tau_y} \frac{y(x_1,...,x_{i-1},x_i+\Delta,x_{i+1},...,x_k)-y(x)}{\Delta} \tag{8}$$

Where τ is the normalization factor for the output, x_i is the parameter examined and Δ is the change in the parameter. An average of this is taken by performing r paths of k + 1 simulations, which is essentially one instance of local sensitivity method. By attempting multiple paths we are able to get an ensemble of EE values. Thus the total number of simulations required to analysis all the parameters is r(k+1) simulations. These can be improved upon by examining the absolute value of the EE, which eliminates cancellations of effect due to negative and positive changes in the output value. These $|EE|$ can then be plotted against the standard deviation of each

value to give a measure or the linearity and interaction of each of the parameters. As such it can be used as a good approximation of the S_{ti} found using global sensitivity method at a fraction of the computational cost [197].

2.2.2 Partial Rank Correlation Coefficients Using Latin Hypercube Sampling

Latin Hypercube Sampling (LHS) is a method for sampling a probability distribution function (PDF) that ensures each portion of the distribution is sampled in an efficient manner [111]. In this method the number of input parameters, k, that are uncertain are given distributions over which the values may be chosen. The number of simulations, N, to be run is then chosen based on the need to ensure a proper level of statistical certainty with a minimal value based on the empirically proven inequality N > (4/3)k[111]. A table of N by k random values are then chosen in the following manner:

- For each input parameter, v_i, the PDF is divided into N equal subgroups (s_0, s_1,...,s_N).
- From each of these subgroups a random value v_{im} is chosen such that $s_m < v_{im} < s_{m+1}$. When this is complete for each of the input parameters k vectors of N values is formed.
- The input parameters for each of the N simulations are then formed by choosing a random value from each of the k vectors to be used as the simulation value of each parameter. This combines to form a table of N by k values.

Partial Rank Correlation Coefficients (PRCC) provide a method for examining the effect parameter has on an outcome variable by performing statistical analysis on the ranks of the variables in different simulations relative to one another.

PRCC are calculated for each of the outcome and input values using the following method. For each outcome value the vector of its values is appended to the original

N by k table of values calculated from LHS. This results in an N by k + 1 matrix of values. For each of the k columns of the matrix an ordinal number between 1 and N is given to the values in the column based on the relative size of the value. From these ranks a k+1 by k+1 matrix (C) is formed where the elements c_{ij} are defined by the equation[168]:

$$c_{ij} = \frac{\sum_{n=1}^{N} (r_{in} - \mu)(r_{jn} - \mu)}{\sqrt{\sum_{n=1}^{N} (r_{in} - \mu)^2 \sum_{n=1}^{N} (r_{jn} - \mu)^2}} i, j = 1, 2, \ldots, k+1 \tag{9}$$

Where μ the average rank of the N simulations. We then define a matrix B such that it is the inverse of the C matrix.

The PRCC between the xth input parameter and the yth outcome variable is defined as:

$$PRCC_{xy} = \frac{-b_{x,k+1}}{\sqrt{b_{xx} b_{k+1,k+1}}} \tag{10}$$

Where b_{ij} is is an element of the matrix B. Each value of the PRCC (reported in the tables as γ) is a measure of the sensitivty of the model results on that parameter with +1 meaning very sensitive and directly correlated, -1 meaning very sensitive and inversely correlated, and 0 meaning insensitive. Each of these values are accompanied by a p-value which is a measure of the PRCC confidence interval.

CHAPTER III

FLUORITE LATTICE DIFFUSION MODEL

3.1 Introduction

Fluorite-structured oxide compounds are of interest as fuel cell electrolytes and oxygen sensors[83] as well as nuclear fuel [54, 139, 167]. When doped with trivalent cations charge compensating oxygen defects form [104, 105, 38, 2, 176, 177]. Experimental and computational research suggests energetic binding/clustering tendencies between cations and oxygen vacancies which correlates strongly with ionic radii [151, 170, 125, 26, 25, 150, 3, 204]. Strong oxygen vacancy-cation association affects the mobility of oxygen ions and therefore the ionic conductivity in aliovalently-doped fluorite oxides. A decrease in ionic conductivity adversely affects performance as fuel cell electrolyte and oxygen sensor [83] and reduces the concentration of mobile oxygen vacancies which facilitates oxidation and eventual dissolution of the nuclear fuel.Therefore understanding thermochemical and kinetic properties of such defects in fluorite structured oxides is of great interest.

The behavior of oxygen vacancies introduced into UO_2 is of interest due to its possible effects on next generational fuels and the oxidation behavior of the fuel during long term storage. The introduction of compounds that cause vacancies in the production of nuclear fuel provide many potential material benefits for the fuel. However, there may be downsides from the introduction of these dopants, in particular with the interaction of dopants, vacancies, and fission gases released during irradiation. Some experimental studies on potential replacements for UO_2 fuels suggest that the introduction of xenon from fission into UO_2 doped with chromium, introduced for its positive effects on UO_2 grains, results in migration of the chromium to grain

boundaries potentially mitigating its positive impact on the fuel. In addition to the introduction of these compounds during the production of uranium fuels, many fission products form trivalent ions that dissolve in UO_2. Understanding the defect ordering/clustering behavior can provide insight into how material properties are affected by these impurities.

In this study we have examined the influence of 12 aliovalent cation dopant (Ru, Lu, Yb, Er, Y, Gd, Eu, Sm, Nd, Pr, Ce, and La) in CeO_2 and UO_2. The ionic radius of six coordinated Ru^{3+} ion is 0.68 Å, while the ionic radius of eight coordinated 3+ ions for Lu, Yb, Er, Y, Gd, Eu, Sm, Nd, Pr, and La are 0.977, 0.985, 1.004, 1.019, 1.053, 1.066, 1.079, 1.109, 1.109, and 1.16 Å respectively. In order to examine such a large problem we have chosen to use an interatomic potential created by the Grimes research group. In order to capture the majority of effects associated with the local geometry we have chosen to use each nearest neighbor cations of both the vacancy and oxygen ion to determine the migrations barrier for diffusion. The resulting barriers are then compared to DFT literature where available in order to determine and assess the validity of these values as an input parameter for the kMC simulation. Energy barriers for oxygen diffusion are calculated by determining the minimum energy pathways for ionic migration. With this comprehensive analysis, we have presented the influence of various dopants, their size and concentration on oxygen diffusivity and ionic conductivity in aliovalent doped fluorite oxides.

3.2 Related Works

In this paper we study the kinetics of oxygen migration in aliovalent doped fluorite structured oxides using kinetic Monte Carlo (kMC) simulations. A kMC based prediction of oxygen ion conductivity in doped fluorites has received attention from several research groups. The kMC based studies of oxygen diffusion in doped fluorite structures so far can be broadly divided into three classes based on the complexity of

the model in terms of the number of neighbor cations used in calculating the barrier to migration of an oxygen vacancy. The first of which uses only the shared nearest neighbor cations of an oxygen and vacancy pair. The second group examined the shared nearest neighbor cations and at least some of the nearest neighbor cations exclusive to both the oxygen ion and vacancy. The third and final group used a larger local area to determine the migration barrier, in addition to the ions described in the previous groups these studies involved either additional cation neighbors or a blocking term due to the presence of other oxygen vacancies in the local vicinity of the oxygen ion and vacancy pair.

One class of researchers used only the two atoms located directly in the path of the oxygen vacancy migrations [47, 100, 62]. This configuration required the smallest number of barriers (three) as an input for the simulation. Krishnamurthy *etal.* [100] used DFT calculations to inform a KMC model of yttrium stabilized zirconium (YSZ). Grieshammer *etal.* [62] examined yttrium doped ceria and used Metropolis Monte Carlo in addition to the kMC to examine the effect of distribution of dopants on ionic conductivity.

The second class used each of the six nearest neighbor cations along the path of the oxygen vacancy migration [146, 68, 135]. These studies have either attempted to treat each neighbor atom separately requiring 30 unique barrier configurations or creating sub groups to reduce the number of barrier calculations further. Pornprasertsuk *etal.* [146] used DFT to estimate migration barriers for kMC in order to examine yttria stabilized zirconia. They made the assumption that no more than three dopant atoms were present in any local group of six atoms. Part of the study in Grope *etal.* [68] studied the ionic conductivity for three aliovalent cations (Y, Sm, and Sc in CeO_2) using calculated values for each of the possible cases in the first class of researchers while also examining the nearest neighbors of the oxygen vacancies as an additive value calculated from DFT. Oaks *etal.* [135] examined La-doped ceria and calculated

all barriers using molecular statics calculations with three interatomic potentials.

The final class of kMC and atomistic studies included explicit information about additional atoms such as other neighbors or additional oxygen atoms [45, 46, 109]. These studies calculated a large number of migration barriers and have focused on trends in these barriers rather than estimating the full ionic conductivity. For example Dholabhai *etal*. [45, 46] used a combination of DFT and kMC to calculate the effect of a dopant on an oxygen vacancy out to the 3rd nearest neighbor atom and then added the effect of each atom to come up with a migration barrier. Li *etal*. [109] examined the formation and growth of defect clusters such as $CeO_2 \cdot M_2O_3$ (M = La^{3+}, Pr^{3+}, Sm^{3+}, Gd^{3+}, Dy^{3+}, Y^{3+}, Yb^{3+}) and $CeO_2 \cdot DO$ (D = Cd^{2+}, Ca^{2+}, Sr^{2+}, Ba^{2+}) in ceria using molecular dynamics (MD) simulations.

In addition to the diffusivity we examine the grouping behavior of dopants and vacancies. Solomon *etal*. [176, 177] have recently provided significant insight into the thermochemical behavior of UO_2 doped with trivalent cations using density functional theory (DFT). They examined formation energetics and defect ordering tendencies in UO_2 compounds substituted with Y, Dy, Gd, Eu, Sm, Pm, Nd, Pr, Ce, and La cations, which are common soluble fission products in nuclear fuel. They considered substitutional configurations that are charge-compensated with oxygen vacancies, and found that phase separation is energetically favored for all compositions considered for UO_2 with Y, Dy, Gd, Eu, Sm, Pm, Nd, and Nd doping, whereas compound formation is favored for Ce and La-substituted UO_2. These calculations show dependence of relative cation size on stability of solid solutions.

3.3 Model

When a 3+ oxide M_2O_3 (M = Sm, Eu, Ce, Pr, Gd, La, Y, Er, Yb, Lu, Ru) is introduced in a fluorite structured QO_2 (Q = Ce or U), the charge imbalance may be compensated by the introduction of defects in the crystal. Charge compensating

defects could include anion vacancies on the O^{-2} sublattice or cation interstitials (host or dopant) on the Q^{+4} sublattice. In order to determine the correct charge compensating defect, we calculate and compare the solution energies of these defect structures when aliovalent dopants are added using interatomic potentials developed by Minervini *et al.* figure 2a and 2b shown the solution energies for each of the defect types in a M-doped QO2 where M = Al, Cr, Ga, Fe, Sc, In, Y, Gd, and La. If the size mismatch between M and Q is small, we find that the anion vacancy has lowest solution energy, suggesting that it is the dominant charge compensating defect when an aliovalent dopant is added. When ionic radius of M is much smaller than Q (e.g., Al, Cr dopants), we find that dopant interstititials may be an equivalent charge compensating mechanism.

In this work, we mainly consider dopants with large ionic radii. Thus we can safely assume that the anion vacancies compensate for the the charge imbalance when aliovant dopants are introduced in a fluorite structured QO_2 (Q = Ce or U). These additional vacancies provide opportunities for oxygen atoms to migrate via a vacancy exchange mechanism on the anion sublattice, thereby enhancing the ionic conductivity. Such an enhanced ionic conductivity has limits - as the dopant concentration and hence the vacancy concentration increases, the point defects impede each others migration as well as creating traps or clusters. Thus for each ionic dopant there is an optimum concentration that enhances ionic conductivity.

Figure 3a shows an oxygen ion and an oxygen vacancy along with their immediate neighboring cations in ceria. Six cation neighbors (marked Q-1 through Q-6) are indicated in the figure. These are neighbors of the oxygen ion (Q-1 and Q-2), neighbors of the vacancies (Q-5 or Q-6) and shared neighbors (Q-3 and Q-4) that represent a bond edge that must be crossed by the oxygen ion in order to complete the vacancy exchange. Thus, both the ion and the vacancy are tetrahedrally co-ordinated by four cations - Q-1 through Q-4 for the ion and Q-3 - Q-6 for the vacancy [68].

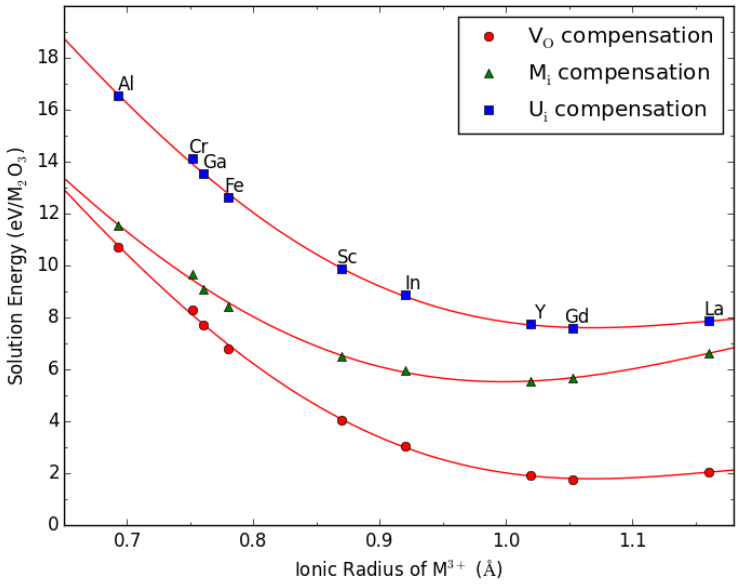

(a)

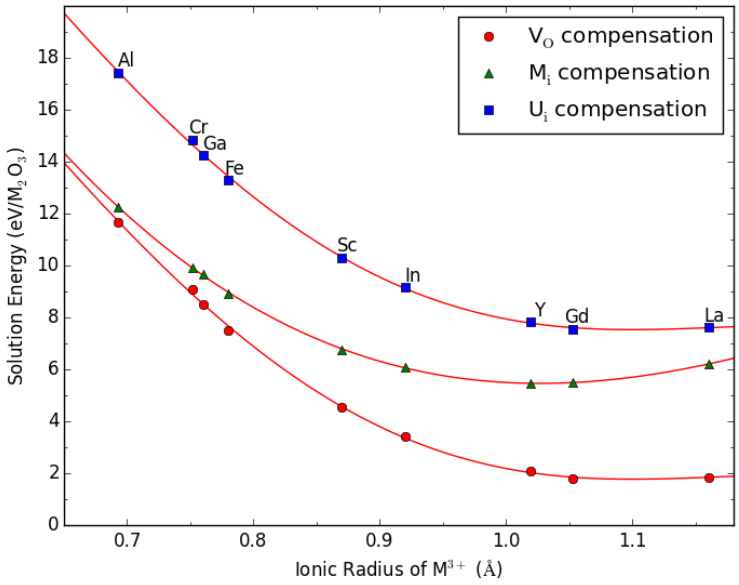

(b)

Figure 2: The solution energy was calculated for a range of dopant sizes for both ceria (a) and uranium dioxide (b). The values found for all but the smallest ionic radii show that the assumption of vacancy compensation as the only extrinsic mechanism available is valid for the dopants considered in this study

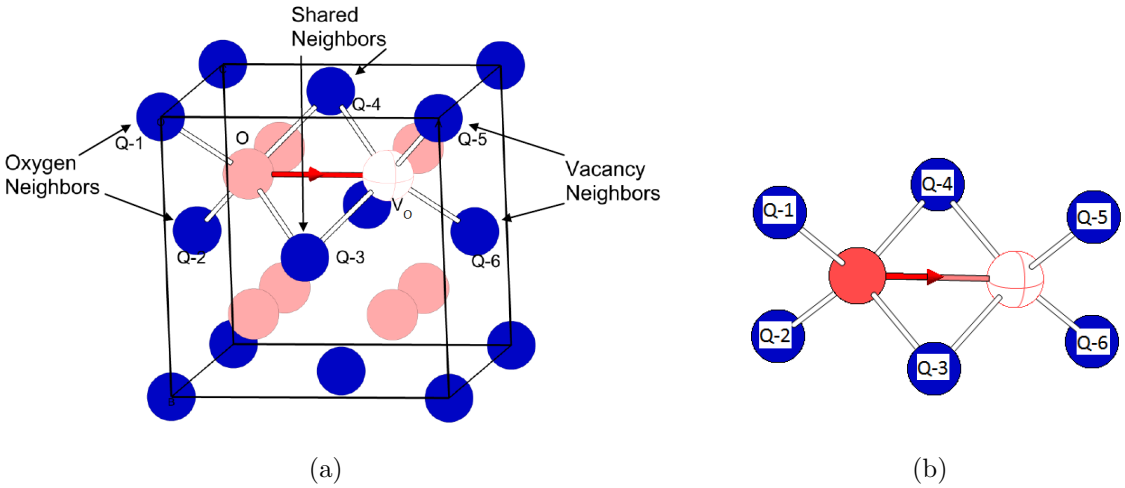

(a) (b)

Figure 3: The oxygen ion moves to a neighboring vacant site in the fluorite lattice (a). There are 6 neighbor ions which are used to calculate the migration barriers (b). These are separated into three groups: neighbors of the oxygen site only (1 and 2), shared neighbors (3 and 4), and neighbors of the vacancy only (5 and 6).

The oxygen ion can perform a jump into the oxygen vacancy by crossing the edge that is formed by the two adjacent tetrahedra [68]. This jump is thermally activated and has an activation energy that depends on the local environment, i.e. the occupation of the cation sites with dopant ions and the occupation of other oxygen sites with oxygen vacancies. In this paper, the dopant cations M or Ce are assumed to be randomly distributed and immobile, as it is well known that cation diffusion in fluorite structured oxides is extremely slow compared to oxygen diffusion. Furthermore, we will consider only nearest-neighbor interactions for which we had calculated the corresponding oxygen migration energies E_{mig} by means of the nudged elastic band (NEB) method for 12 dopants in UO_2 and CeO_2. We calculate for each of these systems how the barrier to the oxygen ion - vacancy exchange depends on the occupation of these 6 neighboring sites by the host or the dopant ion. Thus, there are $2^6 = 64$ configurations and corresponding energy barriers for the oxygen vacancy exchange.

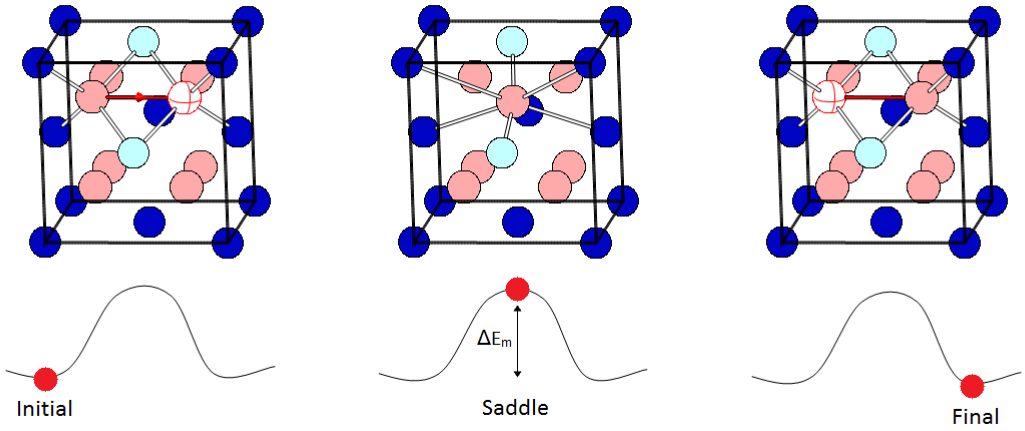

Figure 4: Migration path of an oxygen atom with nearest neighbors highlighted with bonds

3.3.1 kinetic Monte Carlo (kMC)

The algorithm for the Kinetic Monte Carlo (KMC) simulations was implemented using the SPPARKS package. In order to simulate an infinitely extended lattice a finite lattice with periodic boundary conditions in the rectilinear co-ordinate system was employed. A rigid fluorite lattice was created within this periodic box. For each fraction, x_M, of the the dopant cations, the corresponding number of dopant cations M^{+3} ions and oxygen vacancies were distributed on the fluorite lattice. The rest of the fluorite structure was populated with the host Q^{+4} and oxygen O^{-2} ions.

In order to evolve the system a list of all oxygen ions that can migrate to a neighboring vacant site is created. For each oxygen ion that can migrate, a rate constant is computed,

$$r_i = \nu_i e^{-\frac{E_{mig,i}}{k_B T}} \tag{11}$$

The migration energy depends on the local environment, namely, the presence or absence of dopants ions at sites Q-1 through Q-6 and is calculated using the nudged elastic band method described in the following section. The temporal evolution of

the oxygen ion concentration is accomplished by a kinetic Monte Carlo procedure in which one reaction is executed at one site during each time step. Only oxygen-vacancy exchanges are possible in the system and any of the oxygen ions adjacent to the vacancies can move with the rate constant specified in Equation 11. Thus, if there are N vacancies (each with 6 oxygen neighbors), there are a maximum of 6N oxygen migration events. The rate of each event is calculated by Equation 11 depending on the local environment of the ion-vacancy pair. The set of rates computed in this way comprise a rate catalog[194, 195] for the evolution of the system from state to state.

One of the possible events is chosen based on the rate associated with that event. More specifically, the probability of choosing an event is equal to the rate at which the event occurs relative to the sum of the rates of all of the possible events. Once an event is chosen, the system is altered appropriately and the set of events that can occur at the next time step is updated. So at each time step, one event denoted by m is randomly chosen from all of the M events that can possibly occur at that step, as follows:

$$\frac{\sum_{i=0}^{m-1} r_i}{\sum_{i=0}^{M} r_i} < \xi_1 < \frac{\sum_{i=0}^{m} r_i}{\sum_{i=0}^{M} r_i}, \tag{12}$$

where r_i is event i's rate of occurrence given by Equation 11 and ξ_1 is a random number uniformly distributed (U) on (0,1] i.e., $\xi_1 \in U(0,1]$. The event chosen is executed (e.g., the positions of the vacancy and the oxygen ion are interchanged), the time is advanced, and the list of events is updated appropriately. The time increment is sampled as the time increment for which no event occurred and is sampled from the Poisson distribution of the rates of all the events,

$$dt = ln(\xi_2) \sum_{i=1}^{M} r_i \tag{13}$$

where $\xi_2 \in U(0, 1]$. This process is repeated for the duration of the simulation.

Consider, as an example of the simulation, the diffusion of a vacancy in flourite structure CeO_2 as shown in figure 5. Consider two vacancies that can exchange with neighboring ions. In the fluorite structure, each vacancy can exchange positions with up to 6 oxygen ions. The rates of all possible events are calculated using Equation 11 In step 2, the cumulative rate function is calculated using Equation 12. In step 3, an event is chosen among all possible events. If, as shown in the example, vacancy exchange with ion at site 2 is chosen, this vacancy-ion exchange is executed (Step 5). Time is incremented by sampling from the Poisson distribution of the rate catalog (Equation 13). Finally all rates are recalculated based on the changed ensemble (Step 6) and the procedure is repeated. The procedure is repeated until the difference between peak diffusivity reaches within a value of $\epsilon < 3 \times 10^{-7}$ of the value at infinite time, which occurs at approximately 500,000 steps.

The kMC code is adapted from the SPPARKS framework developed by Plimpton *et al.* at Sandia National Laboratory and a Python based framework for dealing with multiple simulations and analyzing the results. The code, an adaptation of the standard diffusion method works with the framework in the following fashion:

1. Input data is passed into the python framework.

2. Each dopant concentration is read in.

3. A latttice of cations and anions is formed with the appropriate number of dopants and vacancies using python's built in random module.

4. A python dictionary is accessed or created containing the migration barriers in order to determine the values for each oxygen site.

5. A set of SPPARKS input files are created based on the initial conditions of the simulation.

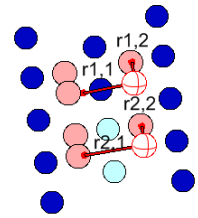

Step 1

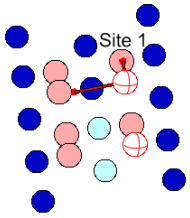

Step 3

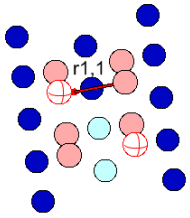

Step 4

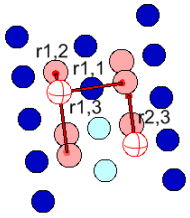

Step 5

Step	Procedure
Step 1	Form a list of all the possible vacancy migrations at each vacant site r_i
Step 2	Calculate the cumulative function $$R_N = \sum_{i=1}^{N} r_i$$ where N is the total number of sites
Step 3	Get a uniform random number $\xi_1 \in (0, 1]$ and select the migration event r_i where $r_{i-1} < \xi_1 * R_N \leq r_i$
Step 4	Exchange the vacancy and ion
Step 5	Recalculate all r_i that may have changed
Step 6	Get a new uniform random number $\xi_2 \in (0, 1]$ and increment time by $$\Delta t = \frac{-log\mu}{R_N}$$

Figure 5: KMC algorithm used in the simulation with pictorial explanation for the migration of one oxygen vacancy on a fluorite structured CeO_2 lattice

6. Multiple simulations can be run at once through the use of the python multi-threading module to execute a SPPARKS instance.

7. The SPPARKS run command has been altered to allow the simulations to be

run for a given number of events as opposed to the traditional use of time as an end parameter.

8. The code examines only the oxygen sublattice to save memory as the host and dopant atoms are fixed.

9. Post processing is performed in the python framework to calculate the diffusivity and ionic conductivity; with figures being produced in matplotlib.

3.3.2 Empirical Potential

We have used empirical potentials developed for various oxides by the Grimes group [196, 63, 30, 65, 64, 23, 31, 125, 126, 67, 41, 42, 189] in this study. The pair potentials can be described by a combination of long-range Coulombic interaction (V_{coul} - attractive), and short-range interaction (primarily repulsive). The short-range interaction is described by the Buckingham potential ($V_{buck,ij}$) for rigid ion model (ions are described as a rigid core). In the shell model, the ions are described by a core and shell which are coupled by a harmonic spring. The sum of the core and shell charge of each ion describes the ionic charge. The core and shell of each ion interacts with the core and/or shell of other ions via Coulombic interaction, whereas the short-range interaction is given by a combination of Buckingham and core-shell potential ($V_{buck,ij}$ + V_{cs}). The long-range and short-range potential equations are given as:

$$V_{coul} = \frac{1}{2}\sum_{i=1}^{N}\left\{\sum_{j=1}^{N}\frac{q_i q_j}{r_{ij}}\right\} \tag{14}$$

$$V_{buck,ij} = A\exp(-r_{ij}/\rho) - C/r_{ij}^6 \tag{15}$$

$$V_{cs} = \frac{1}{2}k\omega^2 \tag{16}$$

where, A, ρ, and C are the fitted parameters for each pair-potential, k is the harmonic spring constant, and ω is the core-shell displacement. Table 3 lists all the pair potential parameters used to describe CeO_2, UO_2, and all the 3+ ion doping.

Only Ce-O, U-O, and O-O pair potentials are described by shell model, while the rest of the interactions are represented as rigid ion model. We have first optimized the bulk CeO_2 and UO_2 structures with the empirical potentials. All the migration energies are calculated in fluorite supercell based on these optimized cell parameters using NEB within GULP [56].

3.3.3 Calculations of migration energy barriers

In order to examine the diffusivity of oxygen in doped fluorite oxides a catalog of migration energy barriers for each possible oxygen movement through the doped lattice structure was created. This catalog was then used by the kMC simulation to determine the probabilities that events would occur during the course of the simulation. The calculation of these energies was performed using the General Utility Lattice Program (GULP). The program perform molecular dynamics simulation based on calculations done with an interatomic potential.

In the first step the optimize subroutine where the lattice structure was assumed to maintain a constant volume and the system was allowed to relax until the lowest energy state was achieved. A 4x4x4 cell was used to avoid size effects in the simulation. In order to maintain a consistent approach one vacancy was introduced and the necessary number of dopants were inserted into the relevant lattice sites. Any charge imbalance that resulted was resolved with the introduction of a background charge by the GULP program itself.

The initial and final positions of the atoms were calculated for each of the 30 unique configurations. This resulted in a series of symmetric and asymmetric cases. We used the NEB method to create a series of "replicas" of the system along a path from the initial to final configuration [123, 124]. Each replica is chosen as a step on the path from the initial to the final configuration and is attached to the previous replica with a "spring" with a particular spring constant associated with it.

Table 3: Empirical potential parameters used to describe the short-range interactions in this study. The parameters are compiled from references [196, 63, 30, 65, 64, 23, 31, 125, 126, 67, 41, 42, 189]. The first paper to use the set of parameters is given in the reference column. Only O^{2-}, Ce^{4+}, U^{4+} are described by shell model, where the core and shell charges are +0.04e and -2.04e for oxygen, 4.20e and -0.20e for both host cations. All the 3+ ions are described by rigid ion model with an ion charge of +3.0e. The oxygen pair potential is the same for all oxide calculations.

Ion pair	A (eV)	ρ (Å)	C(eV.Å^6)	k (eV.Å^{-2})	Reference
O^{2-}-O^{2-}	9547.96	0.21920	32.0	O^{2-}: 6.30	[63]
Ce^{4+}-O^{2-}	1809.68	0.35470	20.40	Ce^{4+}: 177.84	[196]
U^{4+}-O^{2-}	1761.775	0.35642	0	U^{4+}: 160.00	[30]
Al^{3+}-O^{2-}*	1725.20	0.28971	0		[63]
Co^{3+}-O^{2-}*	1226.31	0.30870	0		[23]
Cr^{3+}-O^{2-}*	1204.18	0.31650	0		[64]
Ga^{3+}-O^{2-}*	1625.72	0.30190	0		[65]
Fe^{3+}-O^{2-}*	1414.60	0.31280	0		[65]
Sc^{3+}-O^{2-}*	1575.85	0.32110	0		[65]
Ru^{3+}-O^{2-}	2988.58	0.298210	0		[31]
U^{3+}-O^{2-}**	1165.65	0.37430	0		[41]
Pu^{3+}-O^{2-}**	1150.745	0.37430	12.1		[42]
In^{3+}-O^{2-}*	1495.65	0.33270	4.33		[65]
Lu^{3+}-O^{2-}	1618.80	0.33849	19.27		[67]
Yb^{3+}-O^{2-}	1649.80	0.33860	16.57		[126]
Er^{3+}-O^{2-}	1739.91	0.33890	17.55		[126]
Y^{3+}-O^{2-}	1766.40	0.33849	19.43		[65]
Gd^{3+}-O^{2-}	1885.75	0.33990	20.34		[125]
Eu^{3+}-O^{2-}	1925.71	0.34030	20.59		[126]
Sm^{3+}-O^{2-}	1944.44	0.3414	21.49		[126]
Nd^{3+}-O^{2-}	1995.20	0.34300	22.59		[126]
Pr^{3+}-O^{2-}	2055.35	0.34380	23.95		[189]
Ce^{3+}-O^{2-}	2010.18	0.34490	23.11		[125]
La^{3+}-O^{2-}	2088.79	0.34600	23.25		[65]

* Unable to obtain barriers for all cation combinations likely due to small size of ion

** Actinide values were not used in this study.

Table 4: Explicit representation of the 30 unique oxygen migration conditions (12 symmetric cases and 18 asymmetric cases) possible for M^{3+} doping in AO_2 lattice. Each digit in the configuration corresponds to the labels given in the figure (Q-1 to Q-6) with a 0 representing a host ion (A) and a 1 representing a dopant ion (M). For the asymmetric cases migration energy calculations can be further reduced to 9 due to mirror symmetry. Therefore only 21 different NEB calculations were performed to obtain E_m for the 30 configurations.

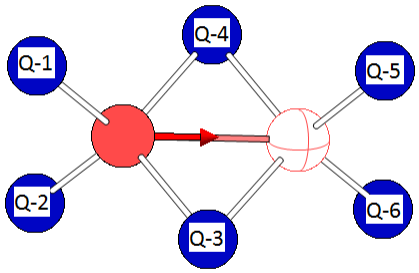

symmetric cases		asymmetric cases		
Case	Configuration	Case	Configuration	Mirror
1	000000	13	100000	000001
2	001000	14	110000	000011
3	001100	15	101000	001001
4	100001	16	111000	001011
5	100010	17	110010	100011
6	101001	18	101100	001110
7	101010	19	111100	001111
8	101101	20	111010	101011
9	101110	21	111110	101111
10	110011			
11	111011			
12	111111			

We then varied the atom positions in each replica until the path along the minimum energy curve from one configuration to the other is found. The difference between the minimum and maximum energy along this path correspond to the migration barrier required for the oxygen atom to move from its lattice site to a neighboring vacant site. From figure 4 for the asymmetric case it can be seen that by looking at the situation in reverse, i.e. the final configuration to the initial configuration, nine of the 30 unique cases are already calculated as they correspond to mirror images of other configurations. Thus the number of calculations in GULP can be reduced to 21 all of which are listed in table 4 including their respective mirror cases if applicable. This reduction in the number of calculations required along with NEB's ability to determine the maximum value with fewer replicas illustrate its benefit over manual minimization calculations like those done by Oaks et al.[135]

3.3.4 Diffusivity and Ionic Conductivity

In order to examine our model compared to other models and experimental data we calculated two values from the kMC simulation the first of these is the diffusivity or diffusion coefficient the equation for this is given by Kofstad[98] for vacancy diffusion as

$$D_{V_O} = \frac{\langle x^2 \rangle}{6t} \tag{17}$$

Where $\langle x^2 \rangle$ is the average distance squared transversed by a vacancy in time t and can be related to the oxygen diffusivity as

$$D_O = \frac{[V_O]}{[O_O]} D_{V_O} \tag{18}$$

Where $[V_O]$ and $[O_O]$ are the concentration of vacancies and oxygen atoms respectively. In this equation the oxygen concentration is often assumed to be one and the equation is reduced to

$$D_O = [V_O] * D_{V_O} \tag{19}$$

However, due to the large ranges of concentrations examined this approximation has not been used in this work unless otherwise noted to conform to previous publications. Since the diffusivity cannot be measured directly by experimentation it is often more convenient to determine the ionic conductivity as means of comparison with experimental methods. According to Kofstad[98] the Nerst-Einstein equation

$$v_i = \frac{z_i e}{kT} D_i \tag{20}$$

Can be combined with the equation for conductivity in terms of the charge mobility, v_i[98]:

$$\sigma_{ionic} = z_i e c_i v_i \tag{21}$$

To relate the ionic conductivity to the vacancy diffusivity[98]:

$$\sigma_{ionic} = \frac{c_v z_v^2 e^2}{kT} D_v \tag{22}$$

Where z_i is the valence, e is the charge of an electron, and kT is the Boltzmann temperature. For the case of oxygen difussion on the fluorite lattice stucture z_i is 2 and c_i reduces to $2x/a_0^3$ where x is the concentration of dopant fraction, $Ce_{1-x}M_xO_{2(1-x/4)}$ giving:

$$\sigma_i = \frac{8xe^2}{kTa_0^3} D_v \tag{23}$$

3.4 Results

3.4.1 Energy barriers

For each of the dopants studied, the migration barriers for each of the thirty unique cases were calculated for both CeO_2 and UO_2. Due to the large computational cost of using DFT the calculation of these energies was performed with molecular statics using empirical pair potentials within GULP [56]. The results of these calculations are then compared with available literature on DFT calculations to attempt to determine the difference between the two methods. The long-range interaction is given by the Coulombic interaction whereas the short-range interactions are described by the Buckingham potential.

A 4x4x4 cell was found to be sufficiently large enough to avoid size effects in the GULP simulation. In order to maintain consistency, one vacancy was introduced and the necessary number of dopants were inserted into the relevant lattice sites. Figures 6 and 7 represents all the 64 cases possible for oxygen migration in the presence of M^{3+} ion. There are 24 symmetric cases and 40 asymmetric cases. The symmetric cases indicate conditions where the configuration before and after migration are energetically equivalent. However, for asymmetric cases the energy of the initial and final configuration are different. Visual inspection of symmetry cases reduce the total number of configurations from 24 to 12. Similar analysis of asymmetric cases result in 18 unique configurations. For calculation purposes the 18 asymmetric cases can be further reduced to 9 as all the configurations have an equivalent mirror configuration. Therefore, only 12 symmetric and 9 asymmetric cases are calculated using NEB to obtain the E_m for the 30 unique configurations. The difference between the minimum and maximum energy along the oxygen motion pathway correspond to the migration barrier required for the oxygen atom to move from its lattice site to a neighboring vacant site. The calculated migration energies for CeO_2 are reported in table 5 and those for UO_2 are reported in table 6.

Table 5: Migration barriers in eV calculated by NEB method using empirical potential for 3+ ion doping in ceria. In the table ONN stands for Oxygen only nearest Neighbors, SNN stands for Shared Nearest Neighbors, and VNN stands for Vacancy only Nearest Neighbors to represent the cation. All the configurations listed in Table 4 can be obtained by reading ONN-SNN-VNN in this table for each dopant.

			Energy Value Ceria										
ONN	SNN	VNN	Ru	Lu	Yb	Er	Y	Gd	Eu	Sm	Nd	Pr	La
	00		0.3069	0.3069	0.3069	0.3069	0.3069	0.3069	0.3069	0.3069	0.3069	0.3069	0.3069
	10	00	0.5755	0.5733	0.5961	0.6375	0.6398	0.7051	0.7261	0.7456	0.7844	0.8171	0.8622
	11		1.0320	1.0040	1.0699	1.1970	1.2048	1.4237	1.4982	1.5677	1.7128	1.8387	2.0162
	00		0.4081	0.3601	0.3428	0.3098	0.3082	0.2622	0.2467	0.2318	0.2093	0.1909	0.1651
00	10	10	0.7139	0.6581	0.6607	0.6697	0.6706	0.6811	0.6824	0.6821	0.6803	0.6774	0.6722
	11		1.2053	1.1174	1.1715	1.2667	1.2738	1.4226	1.4704	1.5117	1.5923	1.6505	1.7122
	00		0.5900	0.4545	0.4025	0.3175	0.3131	0.2068	0.1777	0.1546	0.1100	0.0824	0.0479
	10	11	0.9410	0.7934	0.7616	0.7168	0.7137	0.6385	0.6196	0.5991	0.5567	0.5203	0.4898
	11		1.5672	1.3359	1.3538	1.3712	1.3722	1.3961	1.4153	1.4279	1.4551	1.4778	1.5033
	00		0.1544	0.1662	0.1868	0.2270	0.2302	0.2938	0.3110	0.3251	0.3573	0.3822	0.4072
	10	00	0.3943	0.3861	0.4268	0.5106	0.5164	0.6418	0.6783	0.7094	0.7680	0.8138	0.8677
	11		0.8138	0.7608	0.8502	1.0165	1.0276	1.2913	1.3750	1.4489	1.5937	1.7047	1.8330
	00*		0.2211	0.1992	0.2084	0.2233	0.2249	0.2347	0.2347	0.2317	0.2228	0.2127	0.1903
	00*		0.2329	0.2068	0.2160	0.2327	0.2343	0.2530	0.2571	0.2591	0.2617	0.2623	0.2579
	10*		0.5009	0.4554	0.4876	0.5411	0.5451	0.6062	0.6201	0.6286	0.6402	0.6445	0.6371
10	10*	10	0.5248	0.4682	0.4981	0.5496	0.5536	0.6199	0.6379	0.6517	0.6768	0.6960	0.7051
	11*		0.9756	0.8805	0.9543	1.0878	1.0971	1.2906	1.3466	1.3901	1.4628	1.5065	1.5346
	11*		1.0680	0.9232	0.9911	1.1118	1.1204	1.2975	1.3516	1.3962	1.4856	1.5590	1.6475
	00		0.3674	0.2752	0.2569	0.2288	0.2279	0.1851	0.1702	0.1541	0.1279	0.1038	0.0687
	10	11	0.7010	0.5723	0.5763	0.5742	0.5748	0.5689	0.5630	0.5529	0.5294	0.5064	0.4642
	11		1.3206	1.0758	1.1112	1.1713	1.2035	1.2746	1.2990	1.3136	1.3385	1.3522	1.3489
	00		0.0347	0.0276	0.0545	0.1223	0.1287	0.2552	0.2975	0.3389	0.4181	0.4902	0.5785
	10	00	0.2295	0.1852	0.2327	0.3439	0.3525	0.5213	0.5792	0.6285	0.7231	0.7987	0.9102
	11		0.6694	0.5269	0.6137	0.7725	0.7844	1.0391	1.1327	1.2134	1.3748	1.5084	1.6754
	00		0.0644	0.0420	0.0655	0.1182	0.1230	0.2048	0.2288	0.2481	0.2907	0.3223	0.3571
11	10	10	0.3078	0.2350	0.2807	0.3608	0.3677	0.4930	0.5293	0.5581	0.6118	0.6528	0.6946
	11		0.8125	0.6216	0.6911	0.8191	0.8480	1.0500	1.1134	1.1642	1.2613	1.3347	1.4090
	00		0.1330	0.0780	0.0916	0.1165	0.1195	0.1489	0.1561	0.1598	0.1657	0.1699	0.1671
	10	11	0.4415	0.3140	0.3437	0.3930	0.3979	0.4541	0.4677	0.4750	0.4872	0.4953	0.4936
	11		1.0901	0.7819	0.8353	0.9251	0.9333	1.0478	1.0791	1.0992	1.1372	1.1666	1.1871

Table 6: Migration barriers in eV calculated by NEB method using empirical potential for 3+ ion doping in uranium dioxide. In the table ONN stands for Oxygen only nearest Neighbors, SNN stands for Shared Nearest Neighbors, and VNN stands for Vacancy only Nearest Neighbors to represent the cation. All the configurations listed in Table 4 can be obtained by reading ONN-SNN-VNN in this table for each dopant.

			Energy Value Uranium Oxide											
ONN	VNN	SNN	La	Ce	Pr	Nd	Sm	Gd	Er	Eu	Lu	Yb	Y	Ru
00	00	00	0.3304	0.3304	0.3304	0.3304	0.3304	0.3304	0.3304	0.3304	0.3304	0.3304	0.3304	0.3304
	10		0.8503	0.8030	0.8057	0.7732	0.7341	0.6937	0.6257	0.7147	0.5612	0.5842	0.6281	0.5629
	11		1.8631	1.6866	1.6982	1.5808	1.4460	1.3123	1.1023	1.3812	0.9250	0.9854	1.1094	0.947
	00	10	0.2102	0.2359	0.2348	0.2549	0.2840	0.3128	0.3621	0.2981	0.4120	0.3962	0.3598	0.4630
	10		0.7057	0.7082	0.7089	0.7090	0.7076	0.7018	0.6848	0.7036	0.6768	0.6789	0.6860	0.7327
	11		1.6701	1.5842	1.5926	1.5254	1.4423	1.3538	1.2012	1.4009	1.0709	1.1116	1.2070	1.1499
	00	11	0.0994	0.1436	0.1410	0.1772	0.2287	0.2880	0.4170	0.2584	0.5705	0.5131	0.4112	0.7291
	10		0.5481	0.5982	0.5968	0.6294	0.6656	0.7058	0.7861	0.6826	0.8687	0.8416	0.7838	1.0276
	11		1.4974	1.4628	1.4695	1.4444	1.4134	1.3956	1.3770	1.3978	1.3269	1.3498	1.3787	1.5554
10	00	00	0.3987	0.3646	0.3692	0.3443	0.3162	0.2813	0.2145	0.3002	0.1536	0.1755	0.2173	0.1315
	10		0.8372	0.7726	0.7794	0.7302	0.6675	0.5887	0.4559	0.6299	0.3426	0.3759	0.4626	0.3383
	11		1.7162	1.5585	1.5732	1.4544	1.3088	1.1541	0.8879	1.2357	0.6586	0.7315	0.8988	0.6927
	00*	10	0.2263	0.2416	0.2436	0.2504	0.2551	0.2538	0.2361	0.2562	0.2079	0.2184	0.2379	0.2186
	00*		0.2759	0.2762	0.2787	0.2769	0.2728	0.2653	0.2432	0.2703	0.2169	0.2263	0.2450	0.2366
	10*		0.6635	0.6572	0.6616	0.6504	0.6305	0.5996	0.5224	0.6178	0.4281	0.4629	0.5267	0.4583
	10*		0.7142	0.6879	0.6929	0.6715	0.6433	0.6082	0.5322	0.6279	0.4458	0.4774	0.5363	0.4933
	11*		1.5146	1.4507	1.4611	1.3971	1.3056	1.1969	0.9903	1.2565	0.7859	0.8580	0.9993	0.8581
	11*		1.5675	1.4642	1.4769	1.4023	1.3117	1.2114	1.0251	1.2660	0.8382	0.9050	1.0336	0.9635
	00	11	0.1171	0.1513	0.1524	0.1744	0.2057	0.2336	0.2803	0.2205	0.3329	0.3136	0.2795	0.4296
	10		0.5263	0.5577	0.5605	0.5772	0.5935	0.6013	0.6066	0.5998	0.5923	0.6006	0.6076	0.7159
	11		1.3602	1.3380	1.3480	1.3234	1.2879	1.2396	1.1390	1.2687	1.0396	1.0786	1.1439	1.2717
11	00	00	0.5014	0.4077	0.4164	0.3409	0.2768	0.1987	0.0839	0.2409	0.0082	0.0283	0.0886	0.0110
	10		0.8147	0.7114	0.7224	0.6443	0.5457	0.4423	0.2738	0.4938	0.1307	0.1791	0.2823	0.1634
	11		1.5108	1.3257	1.3444	1.2120	1.0514	0.8978	0.6514	0.9706	0.4096	0.4941	0.6631	0.5359
	00	10	0.3326	0.2896	0.2964	0.2624	0.2245	0.1782	0.0955	0.2037	0.0271	0.0488	0.1002	0.0414
	10		0.6660	0.6099	0.6190	0.5737	0.5155	0.4453	0.3190	0.4841	0.1868	0.2345	0.3256	0.2451
	11		1.3338	1.2302	1.2459	1.1642	1.0603	0.9413	0.7254	1.0068	0.5325	0.6010	0.7351	0.7073
	00	11	0.1809	0.1772	0.1816	0.1764	0.1685	0.1560	0.1219	0.1643	0.0826	0.0963	0.1248	0.1285
	10		0.5086	0.4985	0.5055	0.4937	0.4769	0.4510	0.3827	0.4672	0.2973	0.3290	0.3877	0.4131
	11		1.1667	1.1249	1.1382	1.1027	1.0576	0.9994	0.8689	1.0342	0.7222	0.7760	0.8773	1.0144

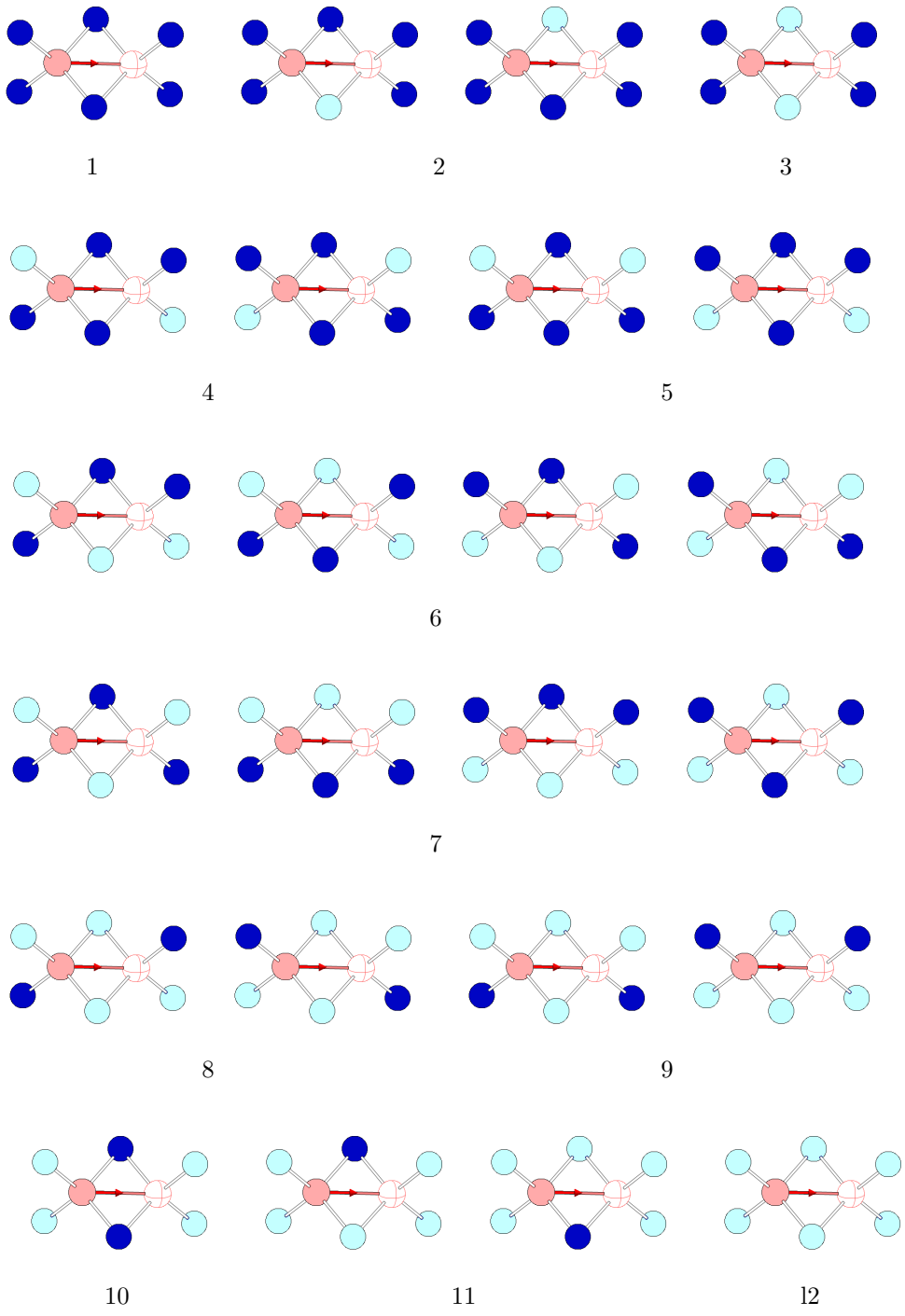

Figure 6: Nearest neighbor ball-and-stick model representation of all the 24 symmetric cases of M^{3+} ion doping in AO_2 lattice (host cations are illustrated darker than the dopant cations). The numbers correspond to the 12 unique cases where cases 1, 3, 10 and 12 have one unique configuration; cases 2, 4, 5, 8, 9, and 11 have two equivalent configurations; while cases 6 and 7 have four equivalent configurations. The configuration numbers are related to those described in Table 4.

13

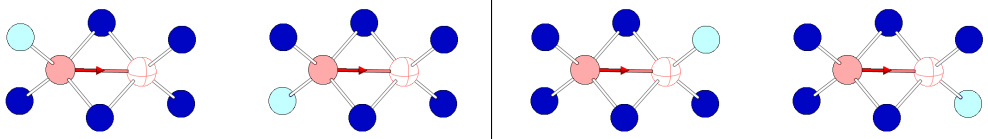

14

15

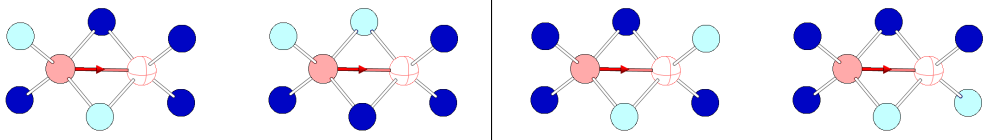

16

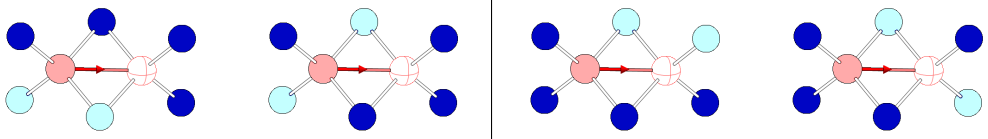

17

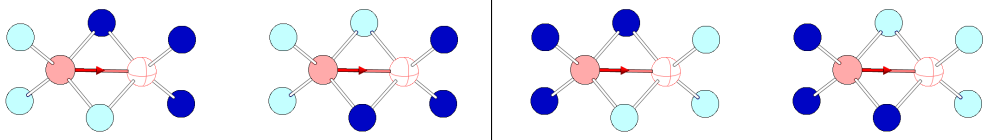

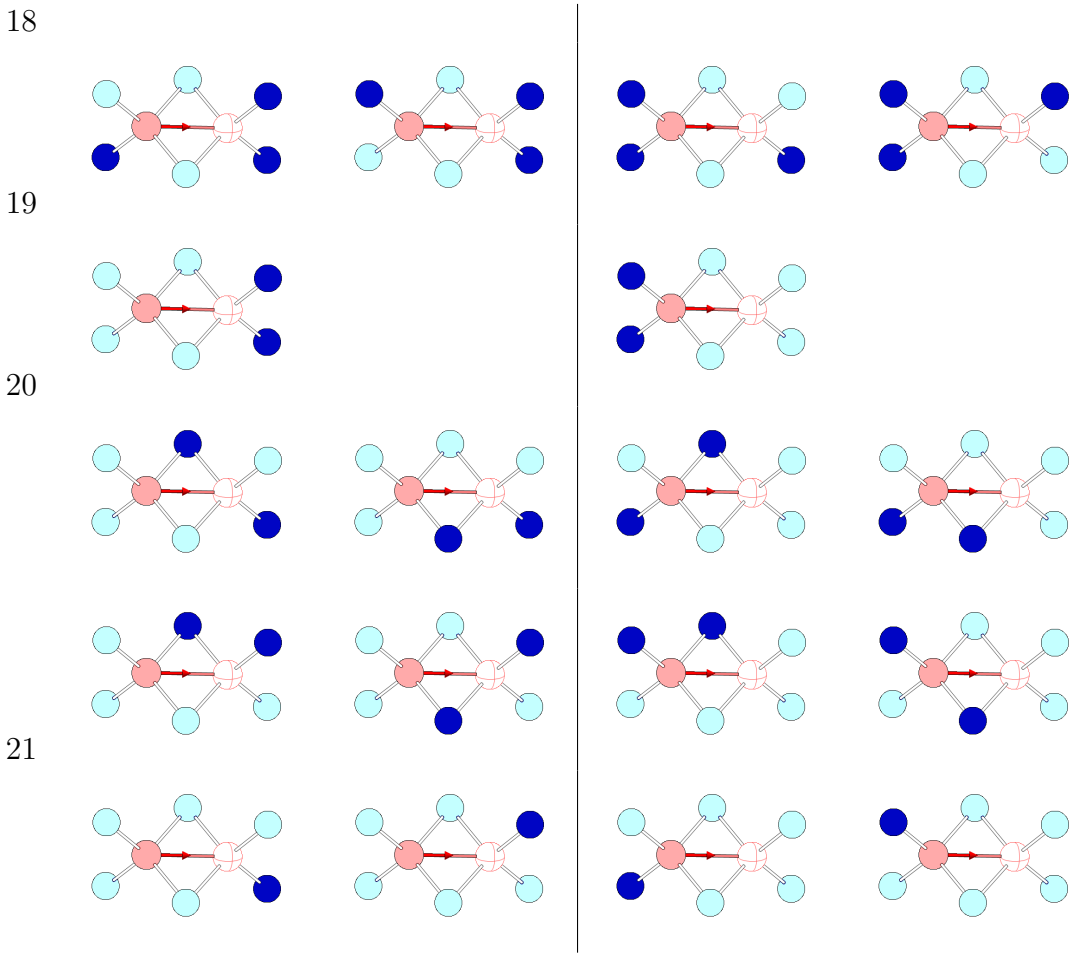

Figure 7: Nearest neighbor ball-and-stick model representation of all the 40 asymmetric cases of M^{3+} ion doping in AO_2 lattice (host cations are illustrated darker than the dopant cations). The numbers correspond to the 9 unique cases along with the mirror cases separated in the two columns. These asymmetric configuration numbers are related to those described in Table 4.

3.4.2 Comparison with Density Functional Theory

Andersson *et al.* [5] examined the migration barrier for 5 of the calculated barriers for 6 of the dopants (La, Pr, Nd, Sm, Gd, Er) studied here. These barriers were formed by inserting an M_2O_3 molecule into a CEO_2 lattice and examining the different configurations of the atoms. The cases studied in the work are 3, 14, 14m, 15, and 15m. In each case the trend of the barrier is the same, however, the values calculated from MD have a wider spread than those found from DFT with values farther from the undoped case spreading out farther relative to those close to this average. In addition there appears to be a trend in the relation with regard to the size of the dopant with smaller dopants causing a wider spread in large value migration barriers and larger dopants causing a wider spread in low value dopants.

Nakayama *et al.* [132] and Grieshammer *et al.* [62] published results for cases 1, 2, and 3 for Lu, Y, Gd, Sm, Nd, and La as a dopant in the case of Kakayama and Y as a dopant in Grieshammer. The result for case 1 suggests that the undoped migration energy is approximately 0.2 eV below the value predicted by DFT. In addition the results for case 2 and 3 confirm the comparison with Andersson that the interatomic potential over-predicts large energy barriers. In addition Kakayama examined cases 13, 13m, 14, and 14m for the case of Y dopant. When these cases are compared to those found with MD the same trends are established.

Combined these results suggest that the use of interatomic potentials will result in a good approximation of the trends of the diffusivity in different dopants but taking into account the exponential effect of large values that the absolute values should be scaled by a factor of 0.15-0.2eV, taking the lower of these values gives us:

$$e^{\frac{-0.15eV}{kbT}} \tag{24}$$

for comparison with DFT and experiment.

3.4.3 Influence of Dopant size on the migration energy barrier

From the energy barrier results some general trends in migration energy can be summarized based on the ionic radii of the dopants with eightfold coordination. Due to the lack of eightfold coordination ionic radius for Ru^{3+}, the results in this section are discussed for Lu, Yb, Er, Gd, Eu, Sm, Nd, Pr, and La dopant ions. The behavior of dopants in the oxygen neighbor positions (figure 3a) is given in figure 7a, which shows the migration energy as a function of dopant size with dopants in two representative asymmetric cases: case 13 and case 14. In case 13 there is one dopant ion as the first nearest neighbor of the oxygen ion in either position 1 or 2, while for case 14 there are two dopant ions as the first nearest neighbor of the oxygen ion in positions 1 and 2 (figure 7). Due to the increase in the dopant ionic radius (from Lu to La), the barrier for oxygen ion migration in ceria increases (figure 7a). This confirms that large dopant ions have a stronger affinity toward oxygen atoms and thus will trap the oxygen ions.

A similar set of calculations are repeated to examine the mirror cases for case 13 and 14, where the dopant ions are sitting in the first nearest neighbor position of the oxygen vacancy (vacancy neighbor positions (figure 3a)). Following figure 7, these are represented as dopant in either position 5 or 6 for case 13 and dopants in positions 5 and 6 for case 14. The results in figure 7b indicates that smaller ions have an affinity toward oxygen vacancies as the migration barrier increases with reduction in dopant ionic radius. In the presence of smaller dopant ions it is expected that oxygen vacancies would be trapped by these ions. The impact of large dopant ions in the oxygen neighbor positions and small dopant ions in the vacancy neighbor positions on diffusion is observed to be the same.

The behavior of dopants in the shared nearest neighbor positions (figure 3a) is examined by considering two symmetric cases: case 2 (dopant in either position 3 or 4) and case 3 (dopants in position 3 and 4) (figure 6). Consistent with the trend for

oxygen neighbor, the migration barrier increases with the increase in dopant ionic radius for shared nearest neighbor positions (figure 7c). In addition, the change in migration energy is observed to be the largest for the shared nearest neighbor positions. Based on these data it is evident that 3+ ion dopants has a tendency to trap either the oxygen or oxygen vacancy and hinder migration.

In order to examine the impact of considering the barriers only associated with the shared nearest neighbor positions (as performed by the first class of researchers, e.g. reference [100]), we have estimated the additional energy required to perform a migration event when one or two of the shared neighbors are occupied with the dopant ion in ceria. Energy comparisons between cases 1, 2, and 3 are performed for the symmetric case, while cases 13, 15, and 18 are considered for the asymmetric cases. Figure 9a shows the energy difference between cases 2 and 1, cases 3 and 2, cases 15 and 13 and cases 18 and 15. These data shows the increase in the barrier with the relative increase in the dopant ionic radius. However, comparing the energy difference between the two symmetric and two asymmetric cases it is clear that the increase in energy is not the same for the first and second added dopant to the shared neighbor positions. The migration energies are affected by the number of dopants in the nearest neighbor positions of the oxygen and vacancy.

Similar analysis has been performed for the oxygen neighbor positions (e.g., migration reported by [68]). Figure 9b shows the energy difference between cases 13 and 1, cases 14 and 13, cases 15 and 2 and cases 16 and 15. This shows the addition of dopants in the 1(5) or 2(6) position does not decrease(increase) the migration energy by a constant value. These results suggest the migration barriers are dependent on the number of dopants in the 3 or 4 position. Therefore, while the simplified models are valuable to investigate oxygen migration, it is necessary to explicitly include migration barriers based on all the six nearest neighbor cation positions to describe the system more accurately.

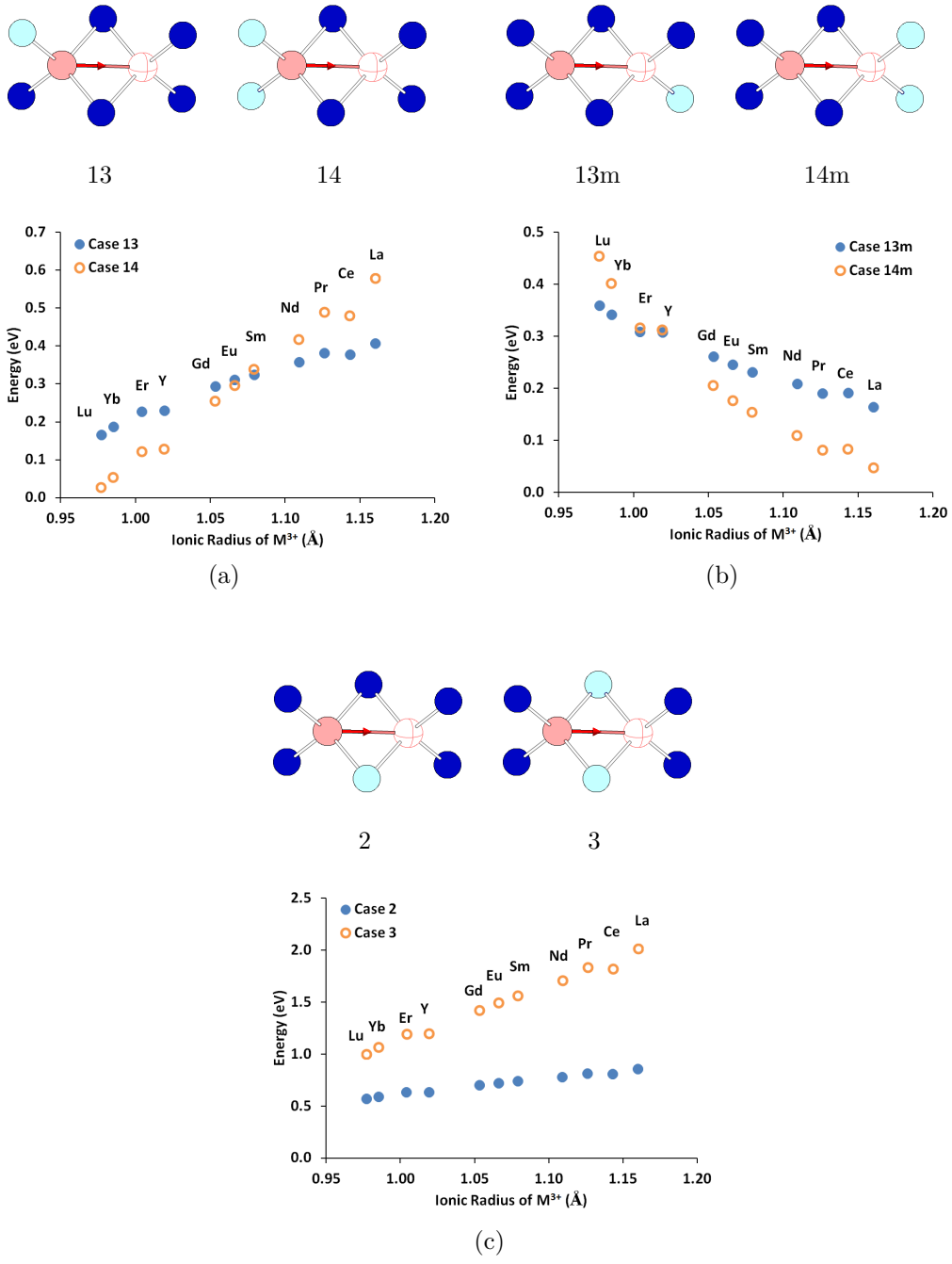

Figure 8: (Color online) The migration energy (in eV) calculated (a) for cases 13 and 14 , (b) for mirror image cases 13 and 14 , and (c) for cases 2 and 3.

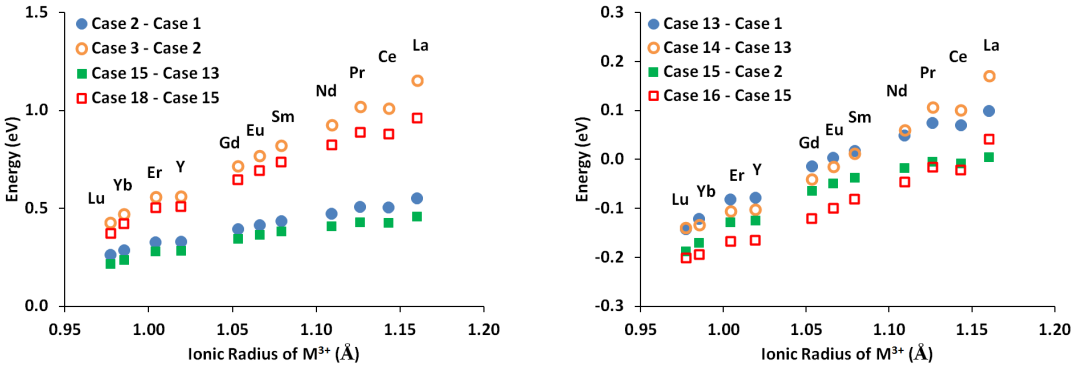

(a) (b)

Figure 9: (Color online) The difference in migration energy ΔE_m (a) for cases 2 and 1 (adding a dopant in position 3 to the undoped case), cases 3 and 2 (adding a dopant in position 4 to the previous case), cases 15 and 13 (adding a dopant in position 3 to the case with a dopant in position 1), and cases 18 and 15 (adding a dopant in position 4 to the previous case) (b) for cases 13 and 1 (adding a dopant in position 1 to the undoped case), cases 14 and 13 (adding a dopant in position 2 to the previous case), cases 15 and 2 (adding a dopant in position 1 to the case with a dopant in position 3), and cases 16 and 15 (adding a dopant in position 2 to the previous case).

3.4.4 Diffusivities and Ionic Conductivities calculated with kMC

The kMC simulation was performed using a periodic lattice with dimensions of $15 \times 15 \times 15$, which is larger than the mean distance traveled by vacancies, at two temperatures, 800 and 400 °C, for a dopant range $0 < x < 0.33$ with Cerium and Uranium used as the host ion. For each simulation the exponential prefactor related to the attempt frequency was assumed to be $\nu_o = 10^{13}/s$. There is evidence that this value may be different[88]. Each set of conditions was simulated ten times with different random seeds in order to provided good statistics. From these results the oxygen self diffusivity was calculated.

The oxygen diffusivity results for 800 °C using Cerium as the host lattice is given in figure 10. The results show that diffusivity increases with increasing concentration until it reaches a maximum value between $x = 0.1$ - 0.25 for all the 3+ ions investigated. This maximum suggests that the increase in vacancies results in more paths for oxygen mobility until the number of dopants added becomes large enough that

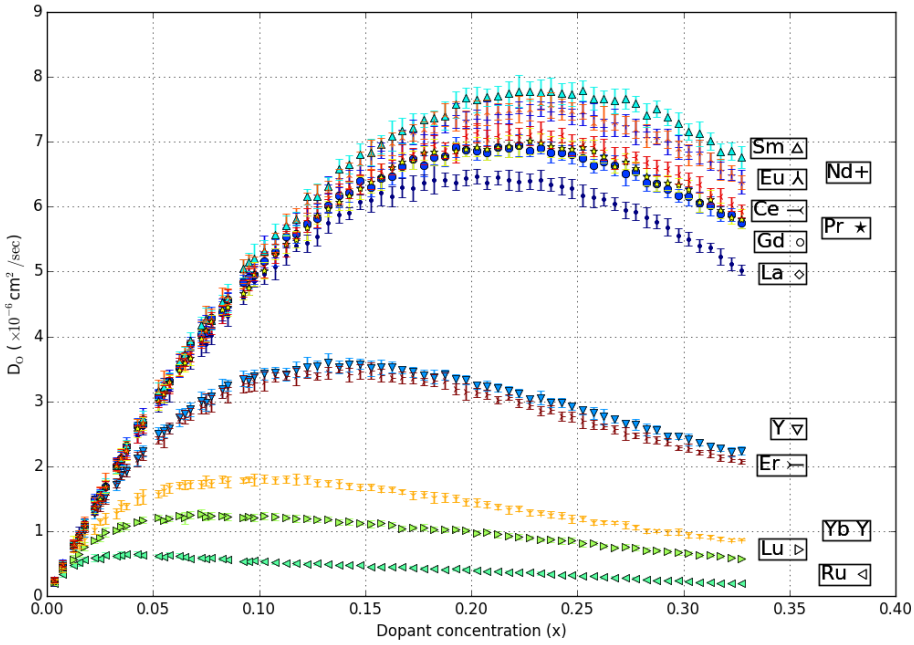

Figure 10: Concentration dependent diffusivity in doped ceria estimated at 800 °C. The highest diffusivity is observed for Sm with 10-20% doping ($x = 0.1$ - 0.25).

vacancies become trapped. This observation of reduction in diffusivity with the increase in defect concentration is in agreement with previous kMC results of vacancies in doped fluorites [100, 68, 135, 45, 46] and oxygen interstitials in hyperstoichiometric fluorites [21].

Since diffusivity is difficult to measure experimentally, it is often more convenient to determine the ionic conductivity therefore the ionic conductivity was calculated from Eq 23. The calculated results for the ionic conductivity are given in figure 11 for all the dopants. The results of several of the dopant ions at $x = 0.2$ concentration are compared with Eguchi *etal*. [51], which is representative of experimental results at this temperature [205, 87, 149]. The kMC results on ionic conductivity follow the same trend as experiment based on the dopant size figure 12. In addition, samarium (Sm) doping in ceria is predicted to achieve the highest ionic conductivity at 800 °C, which is consistent with experiment. The ratio of ionic radius of Sm^{3+} to Ce^{4+} is

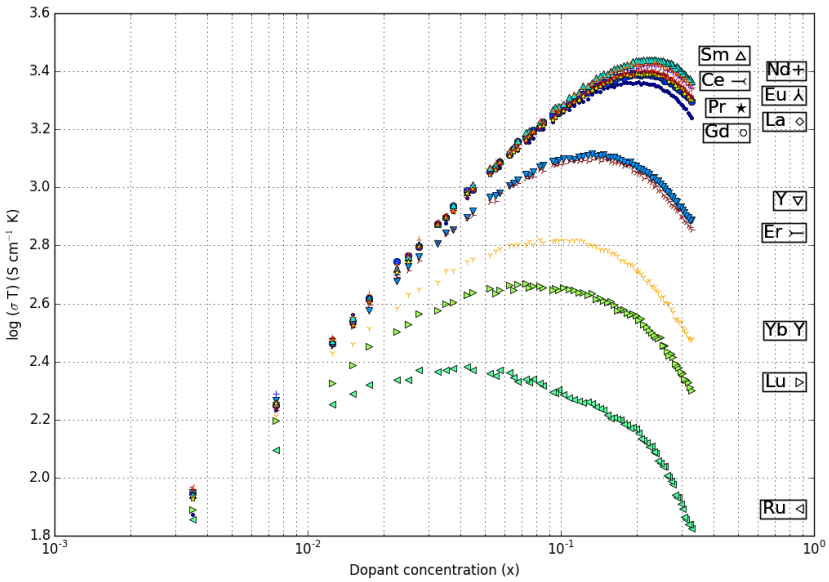

Figure 11: Concentration dependent ionic conductivity predicted by kMC in doped ceria at 800 °C. The highest conductivity is observed for Sm^{3+} doping in ceria.

calculated to be 1.112. Dopant ions smaller or larger than Sm^{3+} ionic radius results in lower ionic conductivity. While the kMC results accurately predicts the qualitative trend with experiment, the quantitative comparison results in an overestimation of ionic conductivity by 1.5-2.5 orders of magnitude at this temperature. For example, our kMC model predicted ionic conductivity of Sm doping in ceria is $2.521 Scm^{-1}$, compared to the experimental value of $0.0974 Scm^{-1}$.

In order to determine the influence of temperature, additional calculations were performed at 400°C. The results for oxygen self diffusivity and ionic conductivity at 400 °C are given in figure 13. Figure 14 illustrates the computational and experimental [7] comparison of ionic conductivity of several of the dopants at 20% concentration ($x = 0.2$). The ionic conductivity result at 400 °C also qualitatively follow the same trend as experiment with the highest conductivity predicted for ceria doped with europium or samarium (ionic radius ratio of Eu^{3+} with Ce^{4+} is 1.10). The experimental measurement of ionic conductivity for Eu is significantly smaller than Sm doping in

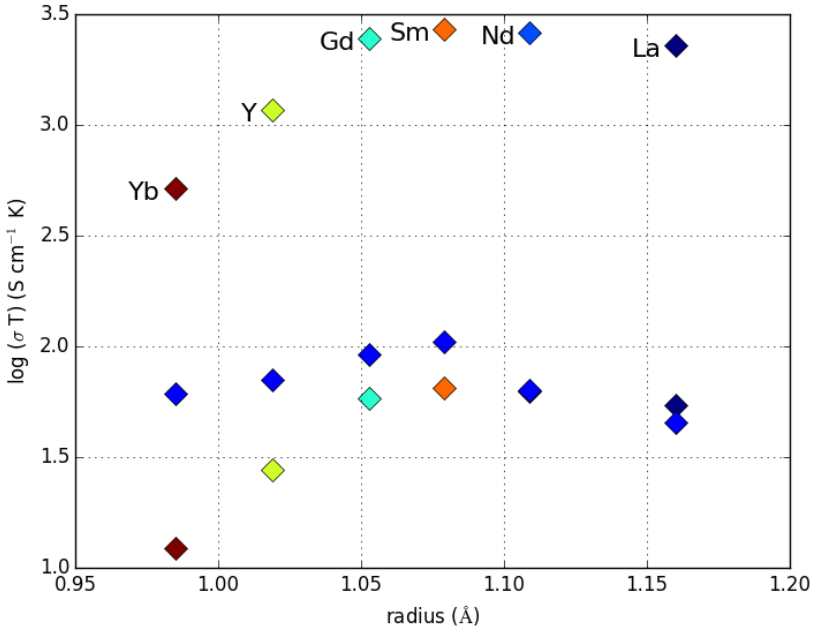

Figure 12: Comparison of ionic conductivity calculated by kMC simulation for 6 dopants at 800 °C at $x = 0.2$ dopant concentration with experiment[51]. The results are plotted as a function of dopant size ionic radius. The kMC results qualitatively match the experimental trend with a peak ionic conductivity occurring for Sm doping in ceria. In addition we have multiplied the results by the factor in eq 24 and found much better agreement.

ceria at 400 °C. Quantitative comparison of the kMC data with experiment show a relatively larger overestimation (3 - 4 orders of magnitude. For example, our kMC model predicted ionic conductivity of Sm doping in ceria is $0.5965 Scm^{-1}$, compared to the experimental value of $6.792 \times 10^{-4} Scm^{-1}$. Comparison of results at 400 °C and 800 °C with experiment emphasizes the temperature dependent nature of ionic conductivity. In order to improve the quantitative comparison, additional sophistication can be included to the existing kMC model such as temperature dependent attempt frequency, possibility of oxygen clustering, grain boundaries, and better migration barrier description (estimate from density functional theory rather than with empirical potential [68]). We have attempted this last result by multiplying our results in the experimental plots by the difference between our migration barriers and those

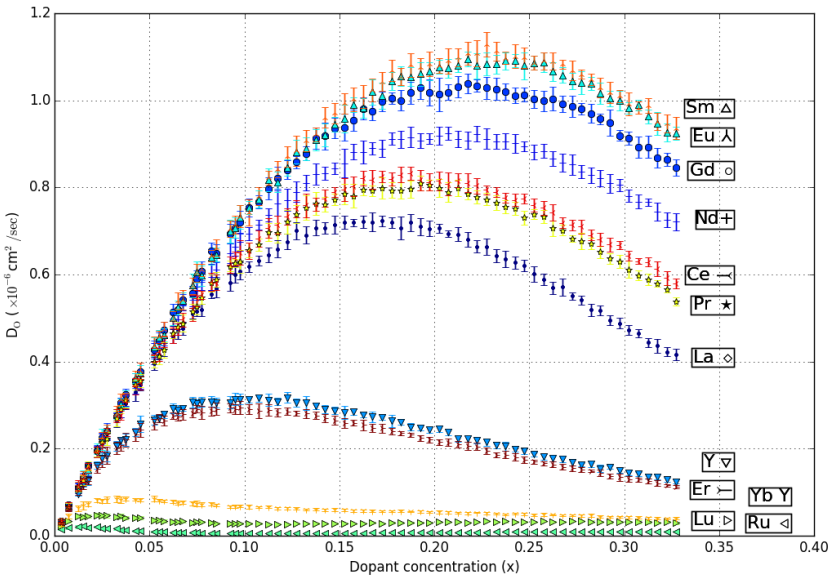

(a)

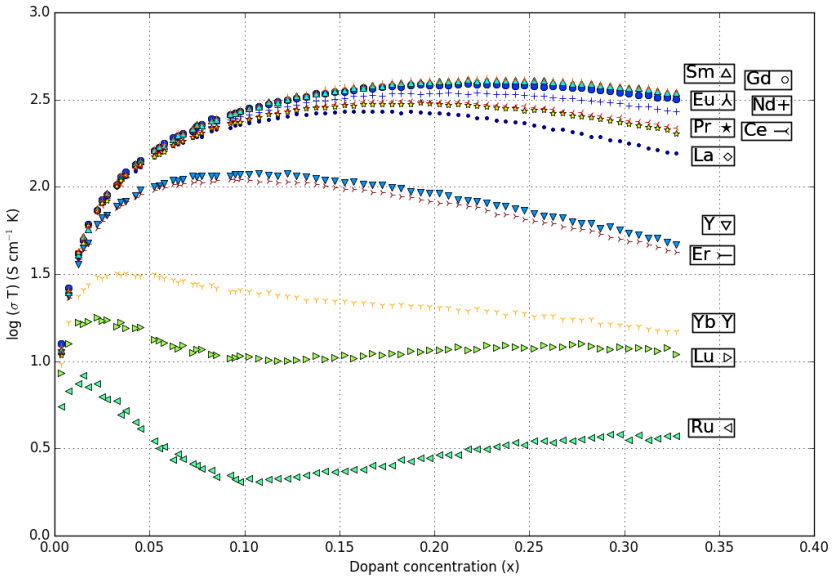

(b)

Figure 13: Concentration dependent (a) diffusivity, and (b) ionic conductivity estimated with kMC for doped Ceria at 400 °C. The highest conductivity is observed for Eu^{3+} doping in ceria.

found in DFT as shown in eq 24.

Finally we have performed the migration energy, diffusivity, and ionic conductivity

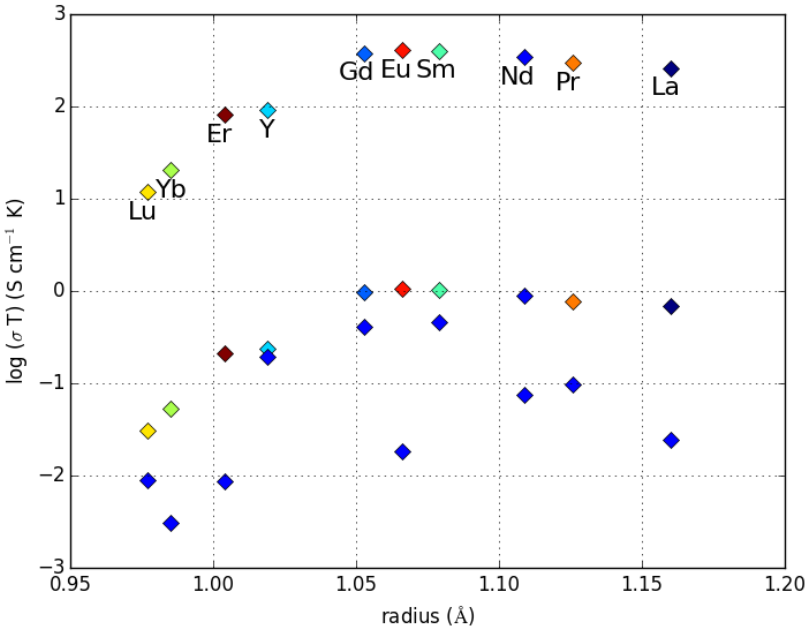

Figure 14: Comparison of kMC calculated ionic conductivity for 10 dopants at 400 °C at $x = 0.2$ dopant concentration with experiment[7]. The results are plotted as a function of dopant size ionic radius. The peak ionic conductivity is achieved for Eu and Sm doping in ceria. In addition we have multiplied the results by the factor in eq 24 and found much better agreement.

calculation for M^{3+} ion doping in urania. Only the oxygen self diffusivity estimated at 800 °C in Uranium Oxide are presented in figure 15. The self diffusivity data for most of the the 3+ ions show the expected initial increase and then decrease with concentration except for Lu. Thus the current model fails to describe Lu doping in urania. The maximum diffusivity in urania is observed to occur in either Pr, Ce or Nd doping at concentrations around $x = 0.225$. The ratio of ionic radius of Pr^{3+}, Ce^{3+}, and Nd^{3+} with U^{4+} results in the range of 1.126 ± 0.017, which is comparable to the ionic radius ratio of Sm^{3+} with Ce^{4+}. This suggests that care must be taken while estimating the diffusion in doped urania based on the diffusion response in doped ceria. Even though ceria is used as a surrogate to urania, the diffusion behavior with the same aliovalent dopant is expected to be different in ceria and urania. These results show a second maximum in the diffusivity of the smallest dopants, which

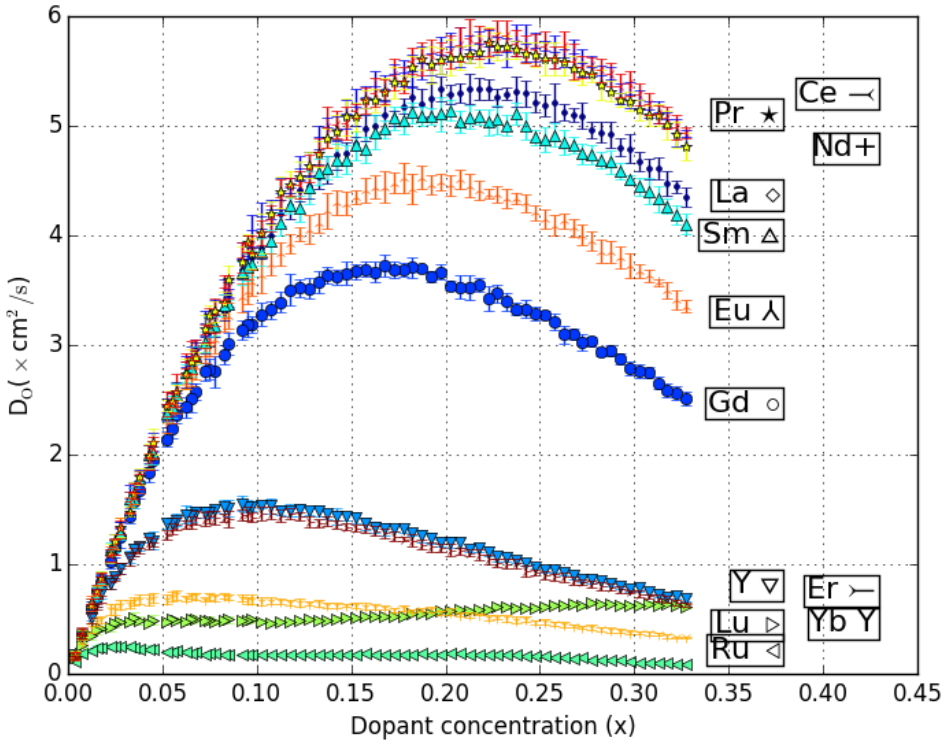

Figure 15: Concentration dependent oxygen self diffusivity in doped urania estimated at 800 °C. The highest diffusivity is obseved for Pr, Ce, and Nd with $x = 0.225$.

is most evident in Ru and Lu, at high concentrations in simulations involving small radius dopants. However, at these high concentrations the fluorite lattice would begin to break down with small dopant cluster forming.

3.4.5 Examination of dopant-vacancy interaction

We examined the location of dopants and vacancies on the fluorite lattice in UO_2 in order to determine if the results on the mesoscale corresponded with those on the atomistic scale [177]. Based on DFT simulations it is expected that as the size of the dopant increases the likelihood that oxygen vacancies would occupy nearest neighbor sites to the dopant would decrease. In order to get an idea of whether vacancies in a non-random configuration would occupy neighbor positions we examined the lattice structure of simulations where $x = 0.2$ both before and after the simulation was run.

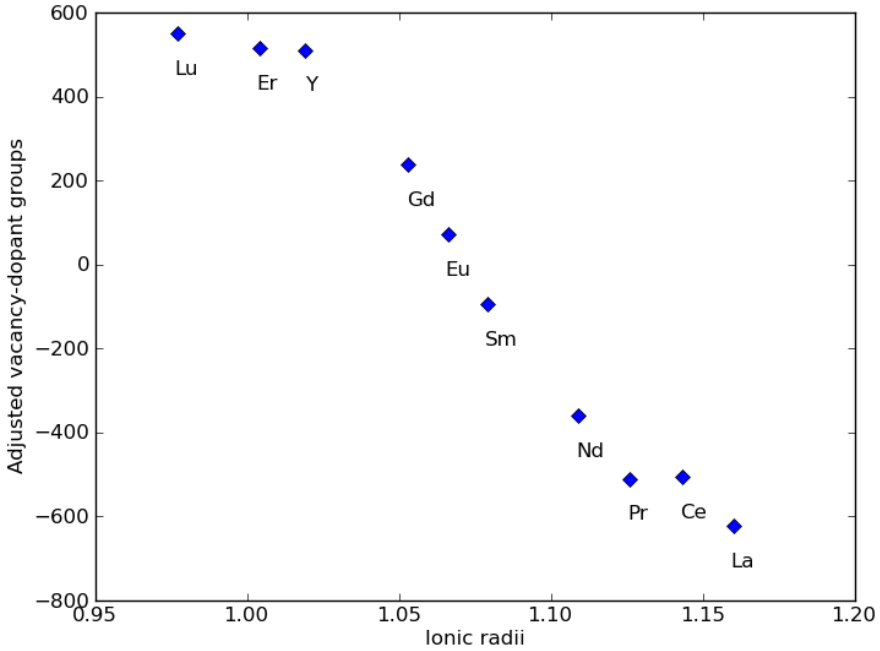

Figure 16: The average number of vacancy-dopant pairs after a simulation is run with the random configuration pairs subtracted out. A positive number means a dopant favors vacancy neighbors while a negative number means a dopant favors oxygen neighbors.

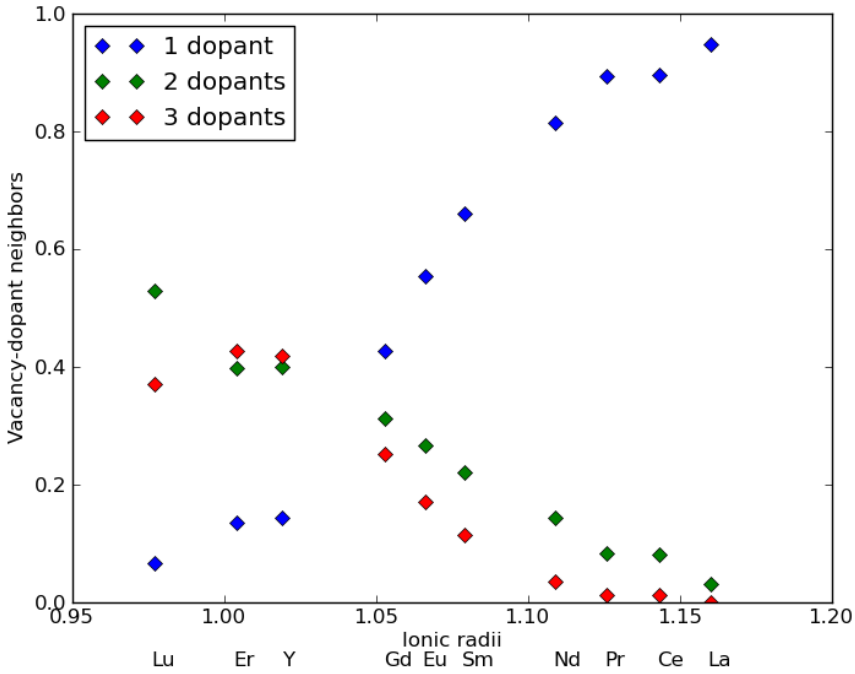

Figure 17: The percentage of vacancy-dopant pairs with 1, 2, or 3 dopant neighbors after a simulation is run.

We then took the average number of vacancies with dopant nearest neighbors in each case and subtracted the before number from the after number. This gave the average number of vacancies that migrated to or from a nearest neighbor position in the simulation. The results of this study are plotted in figure 16 for a range of different dopants. From these results it is clear that the larger dopants prefer more oxygen nearest neighbors. This is in line with the enthalpy of formation as calculated with DFT [177].

In addition we examined the percentage of vacancies that were neighbors to one, two, and three dopant ions. Based on the results of Solomon *et al.* we would expect that the larger the dopant ion the more likely that a vacancy would be positioned as a neighbor to only a single dopant. Conversely small dopants would have the majority of the vacancies with 3 dopant nearest neighbors. Based on the results for the same simulations plotted in figure 17 we see that for small dopants the percentage

of vacancies with one dopant neighbor is significantly less than the percentage of dopants with two or three dopant neighbors. For large dopant ions the percentage of vacancies with only one dopant neighbors is significantly higher than the percentage with two or three neighbors. These results correspond well with what is predicted by the formation enthalpies from DFT.

3.4.6 Sensitivity Analysis

3.4.6.1 MOAT

We have calculated the EE, average EE and standard deviation for the diffusivity in the fluorite lattice for each of the 30 unique input parameters at a dopant concentration of 0.20. We then normalized the values of diffusivity by dividing each EE and standard deviation value by the max EE, $max(EE_{diff})$, we then plot the resulting values.

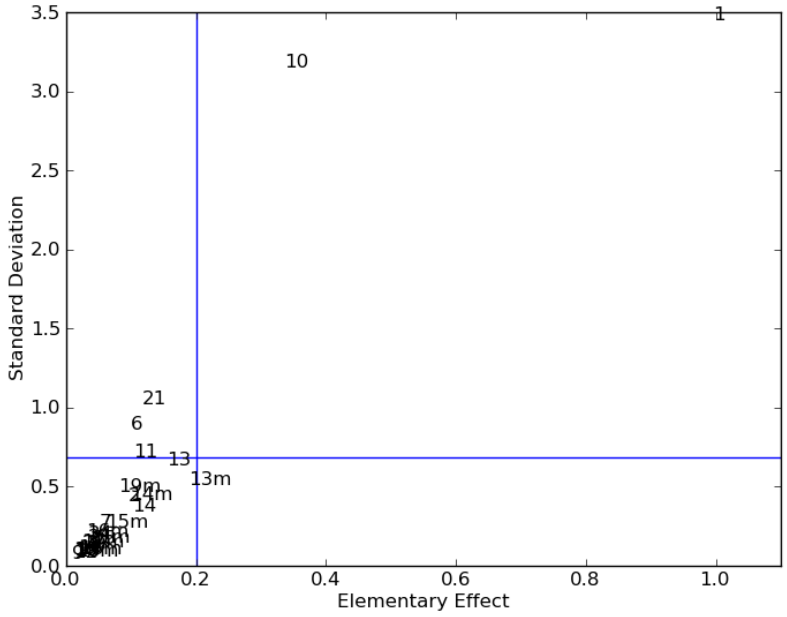

Figure 18: The $|EE|$ values for each of the input parameters for the fluorite model are calculated and plotted. The number markers correspond to those in table 4. The upper left region corresponds to those values which are important and non linear.

The $|EE|$ values are calculated for the model in figure 18. The marker correspond

to the numbers for each configuration given in table 4 and pictured in figures 6 and 7. The plot is divided into three sections to the left of the vertical line is the region with values that have a negligible effect on the output, below the horizontal lines are values that have linear effects without interactions, and the remaining region contains those parameters with non-linear effects and/or interactions. We find that the most important input parameter is the non doped case. This is logical as even at this high doping concentration this would be the most numerous of the configurations. The remaining input parameters have relatively low importance so we plot them without the non doped case.

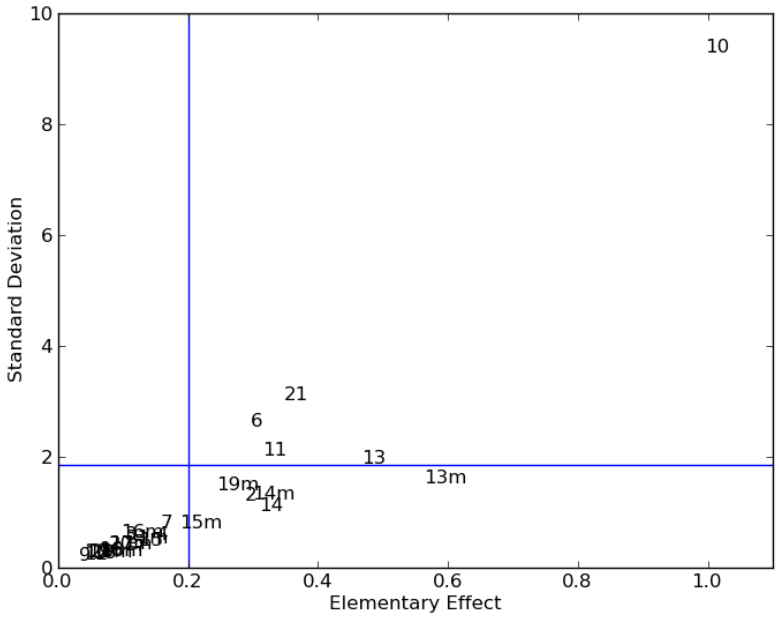

Figure 19: The EE values for each of the input parameters for the fluorite model. The number markers correspond to those in table 4. The upper left region corresponds to those values which are important and non linear.

The $|EE|$ values are calculated for the all the parameters that contain at least one dopant in figure 19. From this we can see that the important parameters with dopants each contain at least one oxygen or vacancy only neighbor. Thus, there does not seem to be any particular correlation between the shared neighbors and the

importance to the model. We examine the input parameters using PRCCs to see if the results correspond to those found with MOAT.

3.4.6.2 PRCC

In examining the importance of different input parameters on the diffusivity using PRCC a dopant concentration of $x = 0.2$ was chosen. Each of the input parameters were allowed to vary over the full range of values found from molecular statics for the dopants studied (0.05-2.0 eV). In order to accumulate accurate statistics 500 simulations were run. The results of the analysis are provided in table 7. From these results it is clear that the most important factor in determining the diffusivity is the non doped configuration. This was seen in the MOAT examination as well. In addition nearly all of the parameters are negative except for several that are positive but small. This result is also to be expected as an increase in a migration barrier would increase the time for an event to occur and thus decrease the diffusivity. Finally, it should be noted that there is no consistent difference in relative importance between configurations with the same number of dopants suggesting that each of the 6 nearest neighbor atoms are important in examining the behavior of the model.

Table 7: The results of PRCC sensitivity analysis on the fluorite model at $x = 0.2$ are given. From these results the most important parameter is the non dopant case. The remaining cases have low importance with a trend toward less importance as the number of dopants increases.

Input Parameter	γ	p value
1	-0.6434	8.87×10^{-60}
2	-0.2223	5.13×10^{-7}
3	-0.0146	7.44×10^{-1}
4	-0.1511	6.99×10^{-4}
5	-0.0666	1.37×10^{-1}
6	-0.0985	2.77×10^{-2}
7	-0.0685	1.26×10^{-1}
8	-0.0321	4.74×10^{-1}
9	-0.0098	8.28×10^{-1}
10	0.0246	5.84×10^{-1}
11	-0.0138	7.59×10^{-1}
12	0.0664	1.38×10^{-1}
13	-0.2197	7.01×10^{-7}
13m	-0.1518	6.62×10^{-4}
14	-0.0193	6.66×10^{-1}
14m	-0.1076	1.59×10^{-2}
15	-0.1945	1.18×10^{-5}
15m	-0.2073	2.93×10^{-6}
16	-0.0749	9.42×10^{-2}
16m	-0.1275	4.28×10^{-3}
17	-0.1154	9.80×10^{-3}
17m	-0.0496	2.69×10^{-1}
18	0.0083	8.52×10^{-1}
18m	-0.0281	5.30×10^{-1}
19	-0.0901	4.42×10^{-2}
19m	-0.0046	9.19×10^{-1}
20	-0.0329	4.62×10^{-1}
20m	-0.0076	8.66×10^{-1}
21	0.0307	4.93×10^{-1}
21m	0.0479	2.85×10^{-1}

3.5 Conclusions

In this section we have used kinetic Monte Carlo (kMC) simulation (within the SPPARKS framework) to examine the defect kinetics in aliovalent doped fluorite lattice. With the aim of examining the influence of 3+ ion doping (Ru, Lu, Yb, Er, Y, Gd, Eu, Sm, Nd, Pr, Ce, and La) in CeO_2 and UO_2, we used empirical potentials to estimate the energy for all possible charge compensating mechanisms. Our results predicted oxygen vacancy compensation as energetically the most favorable mechanism for both CeO_2 and UO_2. In order to establish the effect of doping on oxygen migration, we calculated an extensive list of migration barriers using pair potentials, which are used as the input for the kMC simulations. Based on the occupancy of the six nearest neighbor cation positions with respect to the migrating oxygen ion and vacancy, the migration barriers for all the 3+ ions were computed by the NEB method. The occupancy of the six nearest neighbor cations (oxygen neighbor, vacancy neighbor, or shared neighbor positions) is observed to have a significant influence on the migration barrier. For each dopant, the kMC model used 64 possible migration barriers, which are reduced to 30 unique pathways for examining oxygen diffusion over a large range of dopant concentration ($x < 0.33$).

The qualitative comparison of our kMC results confirms that with the increase in dopant concentration both diffusivity and ionic conductivity initially increase, reach a maximum, and then decrease for very high concentration. This trend is consistent with previous experimental and computational investigation of defect migration in fluorite lattice. The initial increase can be assigned to the increase in vacancy concentration, while the decrease can be explained by the defect interactions and trapping. For both CeO_2 and UO_2, the highest diffusivity for all the dopants investigated is observed to be in the range of $x = 0.1$ - 0.25. Further analysis based on the ionic radius of the dopant ions indicate that the maximum diffusivity/ionic conductivity is obtained for Sm doping in ceria, which is consistent with experimental

measurements. Similar analysis on urania indicates Nd, Pr, and Ce doping results in comparable highest diffusivity. The ratio of ionic radius of dopant showing the highest conductivity to the host ions is calculated to be 1.112 for ceria and 1.126 ± 0.017 for urania. In addition, quantitative comparison of the kMC results with experiment show a significant overestimation of the predicted ionic conductivities for all the dopants. These overestimation in comparison to experimental results is observed to improve with the increase in temperature (comparing ionic conductivities at 400 and 800 °C). Based on this fact and examination of available DFT results the migration barriers calculated by the interatomic potential are about $0.15eV$ low. By adjusting these values upward we get better agreement with experimental results.

Our results provide a comprehensive investigation of 3+ ion doping in fluorite lattice. These results can be used in selecting alliovalent dopants to achieve particular level of relative ionic conductivity for single doping in various applications such as fuel cells. Improvement of the model to investigate the effect of more than one dopant in the fluorite lattice will be valuable for guiding experimental design of materials with desired diffusivity and conductivity.

In addition we have examined the behavior of vacancy-dopant paris and compared the results to atomistic studies on the behavior of dopants in UO_2. We find that as the size of the dopant ion increases the likelihood of vacancies to be located in the nearest neighbor positions decreases. This is consistent with DFT studies that suggest large dopants require higher oxygen coordination. We also examined the percentage of vacancies that neighbored 1, 2, or 3 dopant ions and found that as the size of the dopant ion increased vacancies were more likely to be positioned near a single dopant ion. Again this is consistent with the results of DFT studies[177].

Finally, we performed sensitivity analysis on the 30 input parameters that constitute the different initial configurations. We discovered that MOAT shows that the non doped case is the most important input parameter. Other configurations are

significantly less important, however, there is no distinguishable difference in importance for configurations involving dopants in the shared nearest neighbor positions and those without such dopants. Consistent with these results our examination using PRCCs found that the non doped configuration is the most important configuration, that the majority of configurations were inversely related to the output variable, and that within each group of configurations with the same number of dopants there was no indication that any dopant location was consistently more important than any other positions suggesting that the 6 neighbors positions carry equal importance in determining the behavior of the system.

CHAPTER IV

BCC METAL DIFFUSION MODEL

4.1 Introduction

BCC metals provide significant material advantages in the formation of structural materials for use in nuclear applications. Fe-Cr alloys are used as radiation tolerant alloys in both current generation and next generation nuclear facilities[50]. In addition, Tungsten's high melting point makes it an ideal material for use in plasma facing components of fusion devices and is seen as one of the main components of ITER divertor armor[192]. Due to the need for modern reactors to replace the current commercial fleet of generation III reactors and research into generation IV and fusion reactors the need to focus on nuclear materials is increasing[66].

BCC metals are of interest for their material properties in radiation environments such as low defect accumulation, reduced swelling, and improved creep behavior compared to fcc metals under similar irradiation[58, 136]. However, constant irradiation can cause defects which affect the performance of these metals. The behavior of voids is particularly important as they may form in nearly all materials under irradiation[203]. The most common method for performing simulations into the macroscopic behavior of metals under irradiation is through crystal plasticity models that examine the physical properties of the metals by using rate equations to determine the statistical concentrations of relevant defects. However, through this approach of informing the crystal plasticity model with rate equations we lose information related to the geometry of the metal thus we look at kMC as a way of reconciling the rate equations to the behavior of the material in question[166].

Models of irradiation in metals in order to provide concentrations of defects for

use in continuum scale models have historically consisted of the use of rate equations. The increase in computational power over the past several decades has resulted in the possibility of using kMC models to capture a more complete picture of the defect structure. Due to the complex nature of these models coupled with the uncertainty in the values for input parameters requires the use of uncertainty analysis and sensitivity analysis in order to examine the variability and the effect of input parameters on output parameters.

4.2 Related Works

4.2.1 kMC models of bcc metals

The behavior of defects in bcc metals has been studied in depth using rate equations[28, 101, 175, 200] and kMC simulations. We examine in more detail the groups that have studied the behavior using kMC simulations. Different groups focused on the behavior of different defect types and examined the effect of defect production on the simulation.

The following studies focused on the behavior of defects within pure bcc metals with increasing defect complexity. Studies by Heinisch *et al.* [57, 73, 72, 74] focused on the behavior of interstitials and the formation of interstitial clusters. Barashev *et al.* [9, 10] focused on the behavior of interstial clusters. Cai *et al.* [33, 32] examined the behavior of dislocation loops in bcc metals and the applied it to the specific case of bcc-Mo. This study is unique in that the dislocation behavior is examined directly instead of studying the interaction of various defects together. Soneda *et al.* [179] examined the behavior of defects in bcc-Fe with the inclusion of boundary conditions to simulate grain boundaries. In particular the examined the effects of temperature, dose rate and neutron spectrum on cluster formation. KMC studies done by Becquart and Domain *et al.* [48, 20] focused on the mobility of larger defect clusters. Rottler *et al.* [166] examined the results of various models with both simple defects and clusters

vs their rate equations counterparts.

The focus of studies then shifted to the implantation of other elements into the metals and their clustering behaviors. Caturla [35] focused on alloys and the behavior of voids. Deo *et al.* [44] introduced Helium atoms into the voids. Morishita *et al.* [129] examined the behavior of voids and He clusters in bcc-Fe as an extension of previous MD-MC studies on the subject. Du *et al.* [49] examined the behavior of grain boundaries and Hydrogen clusters in bcc-Fe at various temperatures. Guo *et al.* [69] examined the behavior of He clusters in bcc-Fe with a focus on the temperature and its effect on the size distribution of the resulting clusters. Oaks *et al.* [134] presented a simple study on the formation of voids in bcc-Fe for two different models for the size of the cluster radius.

4.2.2 atomistic studies of defect migration energies

The literature provides a wide range of values and behavior for bcc metals and in particular the behavior of defects in iron has been studied extensively. Vincent *et al.* [193] examined the behavior of self interstitial iron defects in both α-Fe and solid solutions of iron and common alloying metals using VASP. Ventelon *et al.* [192] examined the migration behavior of mono-vacancies in tungsten using SIESTA. Huang *et al.* [81] examined the behavior of vacancy defects and impurity migration of a range of bcc metals in α-Fe using VASP. Satta *et al.* [173, 172] examined the behavior of vacancies in various bcc metals using DFT-LDA methods. Fu *et al.* [55] examined the behavior of vacancies and interstitials in α-Fe using the SIESTA method. Olsson [140] examined the behavior of self interstitial and vacancies in a range of bcc transition metals using an EAM interatomic potential. Pasianot *et al.* [141] examined the behavior of self interstitial defects in bcc Molybdenum using EAM and ED potentials. Mishin *et al.* [128] determined the migration barrier for vacancy migration in bcc Tantulum using ADP. Johnson [86] examined the migration of interstitials and

vacancies in α-Fe using a simple interatomic potential. Shimomura *et al.* [174] examined the behavior of defects and clusters in α-Fe and found the migration energy of vacancies using EAM. Soneda *et al.* [178] used a combination of MD and kinetic Monte Carlo methods to calculate the vacancy and interstitial migration energies in α-Fe.

Based on a review of these sources (Tables 8, 9 and 10) the following ranges were chosen for the input parameters in the different models for sensitivity analysis used:

E_i =0.02 - 0.6 eV

E_r = 1- 5 E_i

E_v = 0.6 - 2.0 eV

Table 8: Table of interstitial migration barriers of bcc metals found in literature

Interstitial Migration Barrier		
First Author	Value	Metal
Soneda [178]	0.17	Fe
Fu [55]	0.34	Fe
Pasianot [141]	0.62	Mo
Pasianot [141]	0.6	Mo
Olsson [140]	0.022	Ta
Olsson [140]	0.016	V
Olsson [140]	0.1	W

Table 9: Table of interstitial rotational barriers of bcc metals found in literature

Rotation Barrier		
First Author	Value	Metal
Soneda [178]	0.16	Fe
Fu [55]	0.56	Fe
Pasianot [141]	0.71	Mo
Olsson [140]	0.1	Ta
Olsson [140]	0.059	V
Olsson [140]	0.43	W

Table 10: Table of vacancy migration barriers of bcc metals found in literature

Vacancy Migration Barrier		
First Author	Value	Metal
Chamati [36]	0.477	Fe
Olsson [140]	0.83	Fe
Fu [55]	0.67	Fe
Olsson [140]	0.96	Ta
Satta [173]	0.81	Ta
Satta [173]	0.75	Ta
Satta [173]	0.83	Ta
Satta [173]	0.67	Ta
Olsson [140]	0.51	V
Ventelon [192]	1.78	W
Becquart [19]	1.66	W
Mundy [131]	1.7 ± 0.1	W
Olsson [140]	1.61	W
Satta [173]	1.82	W

4.3 Model

4.3.1 Simple Defects

For the simplest case where only point defects are considered explicitly and all larger defects are considered to be part of a generic sink concentration the change in defect concentrations with respect to time are governed by the following particle balance equations [166]:

$$\frac{dn_i}{dt} = \sigma F - \kappa_v \omega_{iv} n_i - \kappa_i \omega_{vi} n_v - \kappa_s \omega_{is} n_i \tag{25}$$

$$\frac{dn_v}{dt} = \sigma F - \kappa_v \omega_{iv} n_i - \kappa_i \omega_{vi} n_v - \kappa_s \omega_{is} n_v \tag{26}$$

where σF is the Frankel pair production rate, $\kappa_v \omega_{iv} n_i$ and $\kappa_i \omega_{vi} n_v$ are pair recombination due to the diffusion of an interstitial and vacancy respectively, and $\kappa_s \omega_{is} n_i$ and $\kappa_s \omega_{is} n_v$ are the loss of interstitials and vacancies to sinks respectively. Relationship between the encounter rate, ω, and the diffusivity D (from random walk):

$$\omega = \frac{nD}{a^2} \tag{27}$$

In all bcc metals except iron the ground state intersitial configuration is the $\langle 111 \rangle$ dumbbell interstitial. This configuration results in interstitials that move in a 1D random walk with the ability to rotate into another (111) plane giving a modified random walk term:

$$\omega_{1D/3D} = \omega_{3D} \sqrt{\frac{\gamma_r a^2}{D_i}} \tag{28}$$

where γ_r is the rate at which rotations occur. In order to simplify the simulation and provide results that would cover the full range of bcc metals only the dumbbell interstitial motion was incorporated into the rate equation and kMC models. These give a modified point defect balance equation:

$$\frac{dn_i}{dt} = \sigma F - n_i n_v (\kappa_v \sqrt{\beta} \frac{D_i}{a^2} + \kappa_i \frac{1}{\alpha} \frac{D_i}{a^2}) - \kappa_s n_i n_s \frac{D_i}{a^2} \tag{29}$$

$$\frac{dn_v}{dt} = \sigma F - n_i n_v (\kappa_v \sqrt{\beta} \frac{D_i}{a^2} + \kappa_i \frac{1}{\alpha} \frac{D_i}{a^2}) - \kappa_s n_v n_s \frac{1}{\alpha} \frac{D_i}{a^2} \tag{30}$$

where $\beta = \gamma_r \frac{a^2}{D_i}$ and $\alpha = \frac{D_i}{D_v}$

For direct comparison with kMC we use E_i, E_v, and E_r instead of D_i, β, and α:

$$D_i = e^{\frac{-E_i}{kT}} \tag{31}$$

$$\beta = a^2 e^{\frac{E_i - E_r}{kT}} \tag{32}$$

$$\alpha = e^{\frac{E_v - E_i}{kT}} \tag{33}$$

4.3.2 Irreversible Voids

In the second model we add immobile, irreversible voids to the list of defects. These voids are created by 2 vacancies diffusing to nearest neighbors. They can grow to

larger sizes by incorporating more neighboring vacancies. However, the vacancies cannot leave the void except by annihilation with a neighboring interstitial, thus the only way a vacancy that has entered a void can return to a mobile vacancy is if the remaining vacancies in the void are annihilated. The final restraint on the voids in the kMC model is that no assumptions is made on the shape of the void thus the void's shape encompasses all of the lattice points that the vacancies occupied when they became a member of the void. The defect balance equations for this case are:

$$\begin{aligned} \frac{dn_i}{dt} &= \sigma F - n_i n_v(\kappa_v\sqrt{\beta}\tfrac{D_i}{a^2} - \kappa_i\tfrac{1}{\alpha}\tfrac{D_i}{a^2}) - \kappa_s n_i n_s\tfrac{D_i}{a^2} \\ &\quad - \sum_m \kappa_i n_i n_c(m)\sqrt{\beta}\tfrac{D_i}{a^2} \end{aligned} \tag{34}$$

$$\begin{aligned} \frac{dn_v}{dt} &= \sigma F - n_i n_v(\kappa_v\sqrt{\beta}\tfrac{D_i}{a^2} - \kappa_i\tfrac{1}{\alpha}\tfrac{D_i}{a^2}) - \kappa_s n_v n_s\tfrac{1}{\alpha}\tfrac{D_i}{a^2} \\ &\quad -2\kappa_v n_v n_v\tfrac{1}{\alpha}\tfrac{D_i}{a^2} - \sum_m \kappa_v n_v\tfrac{1}{\alpha}\tfrac{D_i}{a^2} n_c(m) + \kappa_i n_c(2)\sqrt{\beta}\tfrac{D_i}{a^2} n_i \end{aligned} \tag{35}$$

$$\begin{aligned} \frac{dn_c(m)}{dt} &= n_v(\kappa_v n_c(m-1) - \kappa_v n_c(m))\tfrac{1}{\alpha}\tfrac{D_i}{a^2} \\ &\quad + n_i(\kappa_i n_c(m+1) - \kappa_i n_c(m))\sqrt{\beta}\tfrac{D_i}{a^2} \end{aligned} \tag{36}$$

where in equation (34) a term for the annihilation of an interstitial with a void of size m is given by $\sum_m \kappa_i n_i n_c(m)\sqrt{\beta}\frac{D_i}{a^2}$ and in equation (35) terms for the addition of a vacancy to a void of size m is given by $-2\kappa_v n_v n_v\frac{1}{\alpha}\frac{D_i}{a^2} + \sum_m \kappa_v n_v n_c(m)\frac{1}{\alpha}\frac{D_i}{a^2}$ and a term for the formation of vacancies from the annihilation of one member of a divacancy by an interstitial is given by $\kappa_i n_i n_c(2)\sqrt{\beta}\frac{D_i}{a^2}$. Finally, equation (36) is a series of infinite equations with four terms describing the behavior of the voids of size m. The former two terms describe the voids interaction with vacancies with the first term, $\kappa_v n_v n_c(m-1)\frac{1}{\alpha}\frac{D_i}{a^2}$ describing the formation of a void of size m from the addition of a vacancy to a void of size m-1 and the second term, $\kappa_v n_v n_c(m)\frac{1}{\alpha}\frac{D_i}{a^2}$, describing the loss of a void of size m due to the addition of a vacancy which results in a void of size m+1. The latter two terms describe the formation of a void of size m due to annihilation of an interstitial and void of size m+1, $\kappa_i n_i n_c(m+1)\sqrt{\beta}\frac{D_i}{a^2}$, and the loss

of a void of size m due to annihilation of one of its member from interaction with an interstitial $\kappa_i n_i n_c(m)\sqrt{\beta}\frac{D_i}{a^2}$, respectively.

4.3.3 Reversible Voids

The final model introduces a possibility for vacancies to leave the void spontaneously with some rate given by $\gamma_{detached}$ This rate is in addition to the normal diffusion barrier for a vacancy to move. The rate can be calculated from the binding energy of voids of different sizes. In this paper the rate is calculated one of two ways, either by averaging the binding energy over a range of void sizes or by examining a power law found using a best fit of the binding energies over the same range of void sizes. This leads to modification of the previous equations for irreversible voids:

$$\begin{aligned}\frac{dn_i}{dt} &= \sigma F - n_i n_v(\kappa_v\sqrt{\beta}\tfrac{D_i}{a^2} - \kappa_i\tfrac{1}{\alpha}\tfrac{D_i}{a^2}) - \kappa_s n_i n_s\tfrac{D_i}{a^2} \\ &\quad - \sum_m \kappa_i n_i n_c(m)\sqrt{\beta}\tfrac{D_i}{a^2}\end{aligned} \tag{37}$$

$$\begin{aligned}\frac{dn_v}{dt} &= \sigma F - n_i n_v(\kappa_v\sqrt{\beta}\tfrac{D_i}{a^2} - \kappa_i\tfrac{1}{\alpha}\tfrac{D_i}{a^2}) - \kappa_s n_v n_s\tfrac{1}{\alpha}\tfrac{D_i}{a^2} \\ &\quad -2\kappa_v n_v n_v\tfrac{1}{\alpha}\tfrac{D_i}{a^2} + \sum_m (\kappa_{d(m)}\tfrac{\gamma_{detached}(m)}{a^2} - \kappa_v n_v\tfrac{1}{\alpha}\tfrac{D_i}{a^2})n_c(m)\end{aligned} \tag{38}$$

$$\begin{aligned}\frac{dn_c(m)}{dt} &= n_v(\kappa_v n_c(m-1) - \kappa_v n_c(m))\tfrac{1}{\alpha}\tfrac{D_i}{a^2} \\ &\quad +n_i(\kappa_i n_c(m+1) - \kappa_i n_c(m))\sqrt{\beta}\tfrac{D_i}{a^2} \\ &\quad +(\kappa_{d(m)} n_c(m+1-\kappa_{d(m)} n_c(m)))\tfrac{\gamma_{detached}(m)}{a^2}\end{aligned} \tag{39}$$

4.3.4 Molecular Dynamics

In addition to size independent binding energies based on values found in literature, molecular dynamics simulations were conducted with four different interatomic potentials as shown in table 11 in order to produce equations for calculating a void size dependent detachment rate, $\gamma_{detached}(m)$.

In each case, In order to estimate the void stability and formation energy, a periodic super-cell consisting of 10x10x10 body centered cubic (bcc) unit-cells (2000

Table 11: Semi-empirical Iron Potentials used to calculate a size dependent detachment rate for vacancies.

Potential	Type	Why Developed
Mendelev *et al.* 2003 [119]	EAM	Developed for both crystalline and liquid iron
Lee *et al.* 2001 [103]	MEAM-0	Developed to mimic 0K elastic constants and formation energies of iron at 0K
Lee *et al.* 2012 [106]	MEAM-T	Developed to mimic correct structural phase behavior of iron with respect to temperature
Lee *et al.* 2012 [106]	MEAM-P	Developed to mimic correct structural phase behavior of iron with respect to pressure

atoms in the defect free system) was simulated. We performed energy minimization in order to achieve the energy of a perfect bcc lattice. Then in order to calculate the defect formation energy of a vacancy, an atom was removed from the perfect bcc lattice creating a vacancy in the system. This new system with the vacancy then underwent another energy minimization to find the relaxed structure. Then the vacancy formation energy can be calculated using these relaxed structure energies:

$$E_{f,vac} = E_{n-1} - \frac{n-1}{n} E_n \tag{40}$$

The formation energy of a void can be calculated similar to that of a vacancy, but now you have multiple clustered vacancies creating a void. The formation energy of a void can be calculated by:

$$E_{f,void}(x) = E_{n-x} - \frac{n-x}{n} E_n \tag{41}$$

where x is the number of vacancies in the void. The formation energies can then be used to find the vacancy binding energy to an existing void. The binding energy can be obtained by:

$$BE_{vac}(x) = E_{f,void}(x-1) + E_{f,vac} - E_{f,void}(x) \tag{42}$$

where x is the size of the existing void. This binding energy of the vacancy to a void can be directly incorporated into the rate equations formulation.

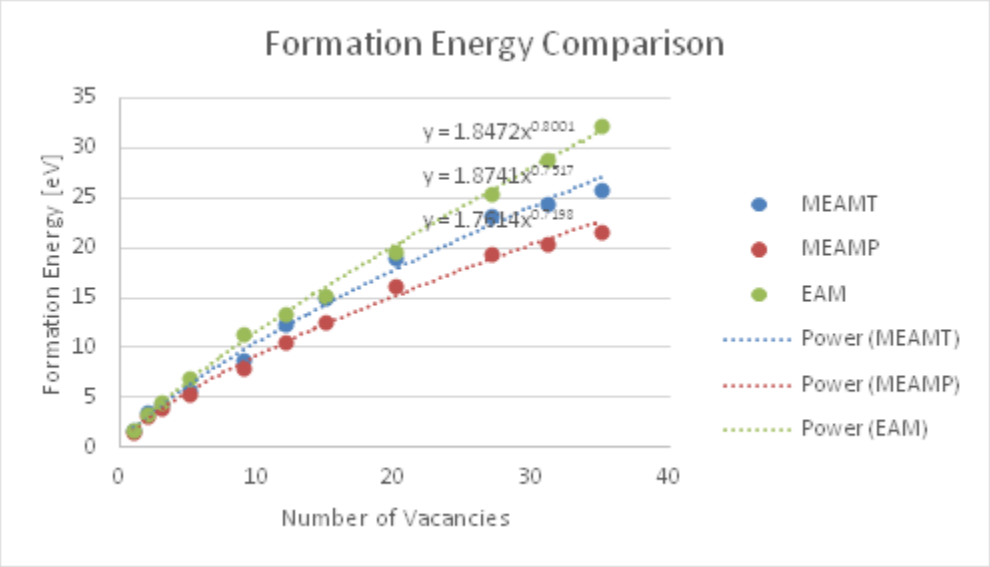

Figure 20: MD results of void formation for different potentials. Void sizes up to 35 were considered which is beyond the size formed in kMC simulations of reversible voids with constant detachment rates. In addition power law equations were fitted to the results for use in the kMC simulations.

Figure 20 shows the void formation energy for the three potentials namely the EAM, MEAM-T and the MEAM-P. The formation energy difference between the three potentials can be seen in the figure above. The MEAM-0 potential was found to be unstable after the introduction of defects and could not be used. The epistemic uncertainty from the differing semi-empirical potential used in a 35 vacancy void is seen to be as large as approximately 10eV. Each semi-empirical potential formation energy versus number of vacancies in the void was fit to a power law equation. The power law fit has been used by previous simulations[178] and been shown to work reasonably well.

4.4 Results

4.4.1 Examination of Void Behavior in Models

4.4.1.1 Simple Defect Model

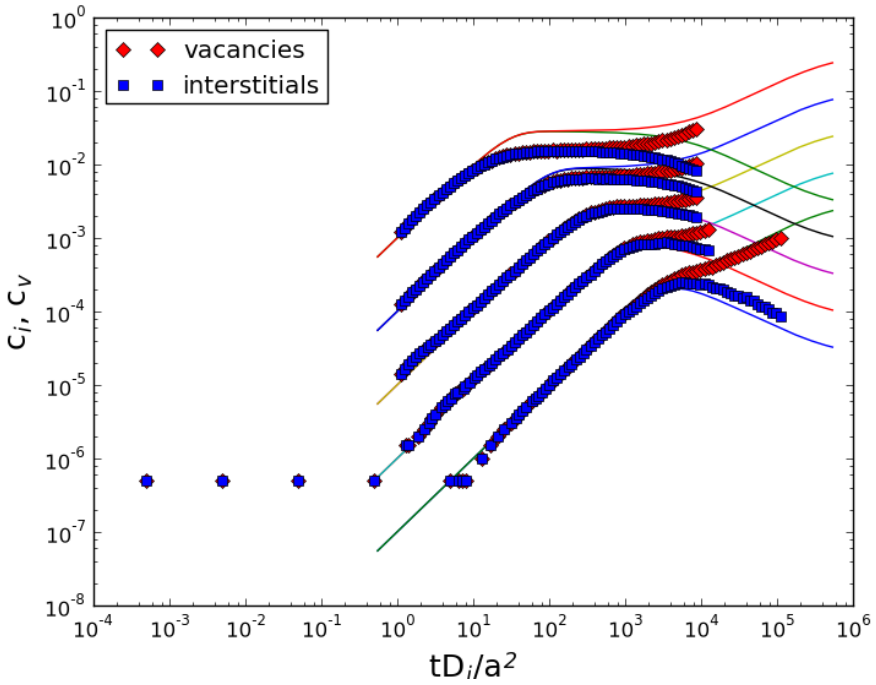

Figure 21: Results of the simple defect model for 5 different values for the Frankel-pair production rate (σF): 5.55×10^7, 5.55×10^6, 5.55×10^5, 5.55×10^4, and 5.55×10^3 dpa/s (From top to bottom). The rate equations assumed that all defects within one lattice constant of a sink or opposite defect type were annihilated giving a value of 4π for the capture radius.

Table 12: Input parameters for the simple defect model of bcc metals and all subsequent models.

	kMC	Rate Equations	
E_i	0.1 eV	D_i	0.055
E_r	0.258 eV	β	0.01
E_v	0.338 eV	α	1000
T	400K	a^2	1

The kMC model and equivalent rate equations for the model that only accounts for simple defects is given in figure 21 for 5 different values for the Frankel-pair

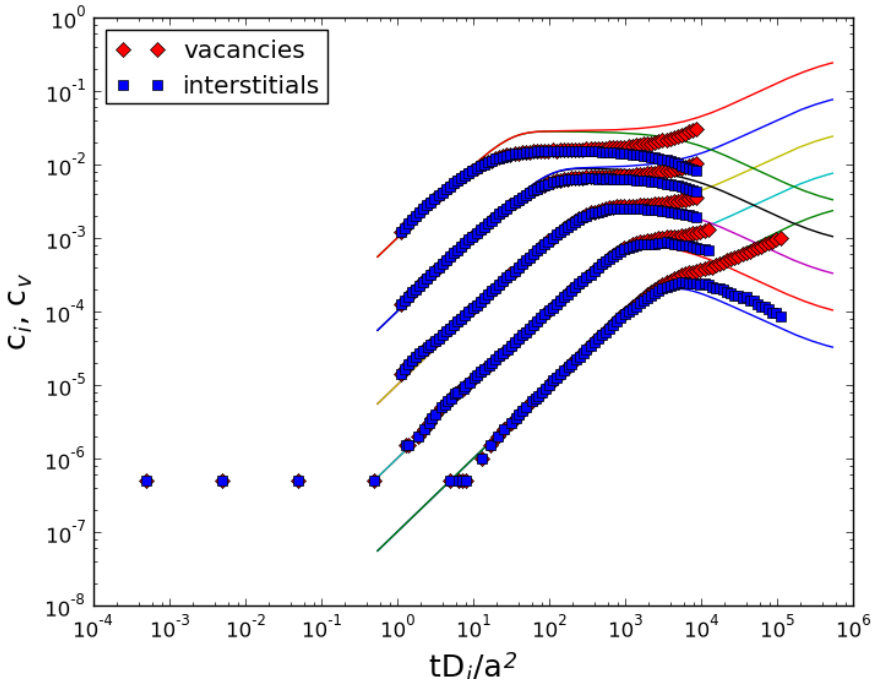

Figure 22: Results of the simple defect model for 5 different values for the Frankel-pair production rate (σF): 5.55×10^7, 5.55×10^6, 5.55×10^5, 5.55×10^4, and 5.55×10^3 dpa/s (From top to bottom). The rate equations assumed that all defects were annihilated by a sink or opposite defect type only upon reaching the nearest neighbor position giving a value of $4\pi\sqrt{3}/2$ for the capture radius.

production rate (σF): 5.55×10^7, 5.55×10^6, 5.55×10^5, 5.55×10^4, and 5.55×10^3 dpa/s. These values are well above the range of those found in experiment but were chosen to correspond to those performed by Rottler *et al.* [166] for comparison of the models. The other parameters for this example are given in Table 12. In general the results are in agreement, however, in order to fit the rate equations to the kMC the choice of the rate constants, κ, is different. According to Rottler *et al.* their model corresponds to a value for κ of 21 for all species interactions. In our model the value for κ is chosen based on the definition of this term as found in *Fundamentals of Radiation Materials Science: Metals and Alloys* [200] which is $4\pi R$ where R is the radius of the interaction. Based on the fact our models assumes only defects in the nearest neighbor position interact this value should be between 4π, which is the closest next nearest neighbor distance in the bcc lattice and $4\pi \times \sqrt{3}/2$, which is the nearest neighbor distance. The value for the closest next nearest neighbor distance was used in figure 21 and shows good agreement, while the value for the nearest neighbor position is given in figure 22 and also shows good agreement. Since there is no indication in Rottler *et al.* as to why 21 was chosen as this value, in general our kMC results correspond with those in Rottler, *et al.* and our value is chosen based on the established definition of κ, we assume that our model is accurate and that 4π is an appropriate value to use for κ in future studies.

4.4.1.2 Irreversible Voids Model

The next set of simulations introduced irreversible voids to the simple defects examined in the previous section. The addition of voids creates an infinite set of equations to describe the behavior of voids of size m we must therefore choice a maximum void size (m_{max}) when using the rate equations method. However, this approximation is unnecessary for the kMC model as voids of any size may form if the vacancies diffuse to neighboring locations on the lattice. Thus we expect some divergence of the two

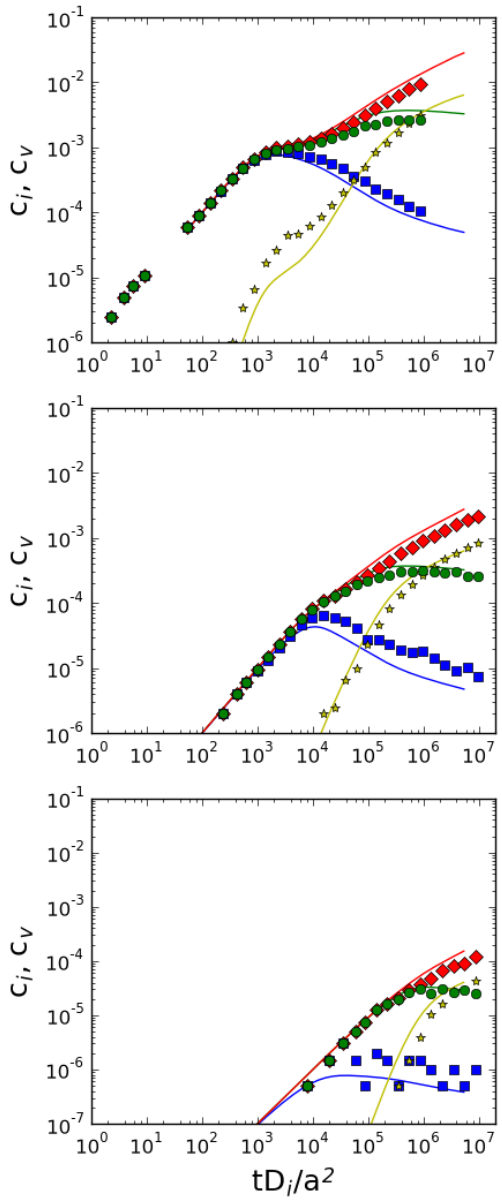

Figure 23: The results of the irreversible voids simulation for three different values of σF (5.55×10^4, 5.55×10^2, and 5.55×10^0). The rate equations for voids are truncated after a void size of 20. The capture radius for voids is set to 2 times the value for simple defects.

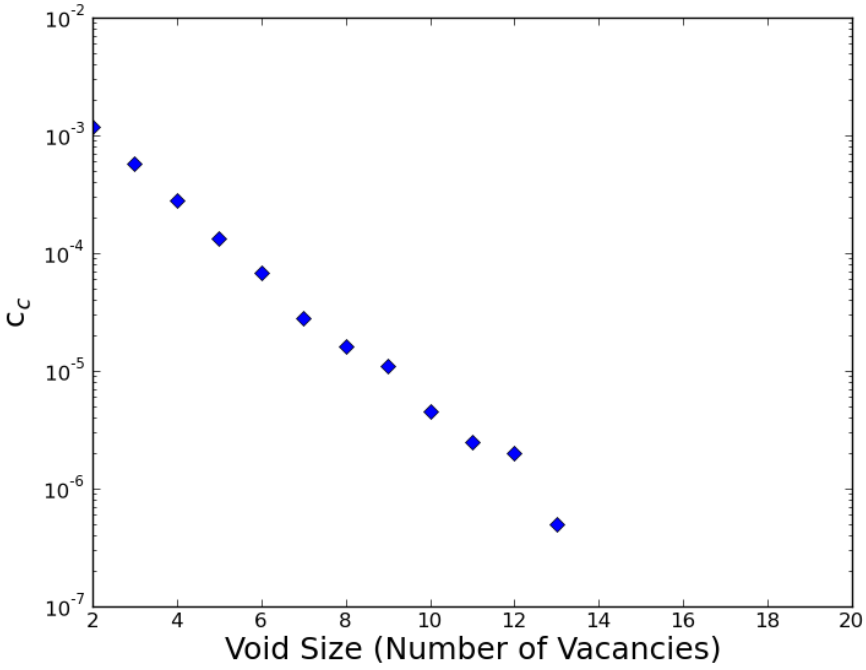

Figure 24: The results void size distribution for the irreversible voids simulation for $\sigma F = 5.55 \times 10^4$.

models if the value of m_{max} is not chosen to be large enough to encompass the largest void sizes found from kMC. For comparison with Rottler *et al.* we choose a value of 20 for m_{max} in the simulations. The results of the simulation for three different values of σF (5.55×10^4, 5.55×10^2, and 5.55×10^0) are given in figure 23. From these results we see good agreement between the kMC and rate equation results at lower values of σF, however, in order for this agreement we have chosen a capture radius of all cluster sizes of $2 \times \kappa$ which is similar to the value used in Rottler *et al.* This choice of κ_m is arbitrary and done only to match the kMC results. In addition it appears that at low values of the production rate this assumption begins to break down. Thus it appears that examination of the interaction of vacancies with the voids is an important point to study and may be dependent on the rate of irradiation. We have plotted the void size distribution for the highest production rate (figure 24) and we will compare this to more complicated models.

4.4.1.3 Reversible Voids Model - Constant Barrier

In the next simulation the voids are now assumed to be reversible, requiring vacancies to overcome an additional barrier in order to detach from a void. Initially this barrier is assumed to be a constant value independent of the size of the void. Again we examine the difference in the kMC simulation and the rate equations we assume the same parameters as in the previous section with the detachment rate set at the same value as the vacancy barrier and examine only two production rates (5.55×10^4 and 5.55×10^2). The results are shown in figure 25. Again there is good agreement between the kMC simulation and the rate equations and between previously published values. In addition we examine the size of the resulting vacancy clusters for the production rate 5.55×10^4 (figure 27 with results of size dependent barriers included) and find that the size of clusters is similar to those found using the irreversible voids suggesting that the irreversible voids model is likely the highest level of complexity need to examine bcc metals.

4.4.1.4 Reversible Voids Model - MD generated power law

In our final simulation we examine the behavior of size dependent barriers for the detachment rates in the voids. The power law equations for the three atomistic models examined in 4.3.4 were inputted into the kMC model as the values for the barriers of vacancies attempting to leave a void. The results of each simulation at a production rate of 5.55×10^4 are compared to the results for a constant barrier in figure 26, from these results it is clear that there is minimal difference in the resulting concentrations of both simple defects and voids between the different models. In addition we examined the frequency of different sized clusters in the different models (figure 27) and found that the void size distribution is nearly independent of the method for calculating the detachment rate and that they are nearly identical to the values produced using a constant barrier. This suggests that a constant barrier is

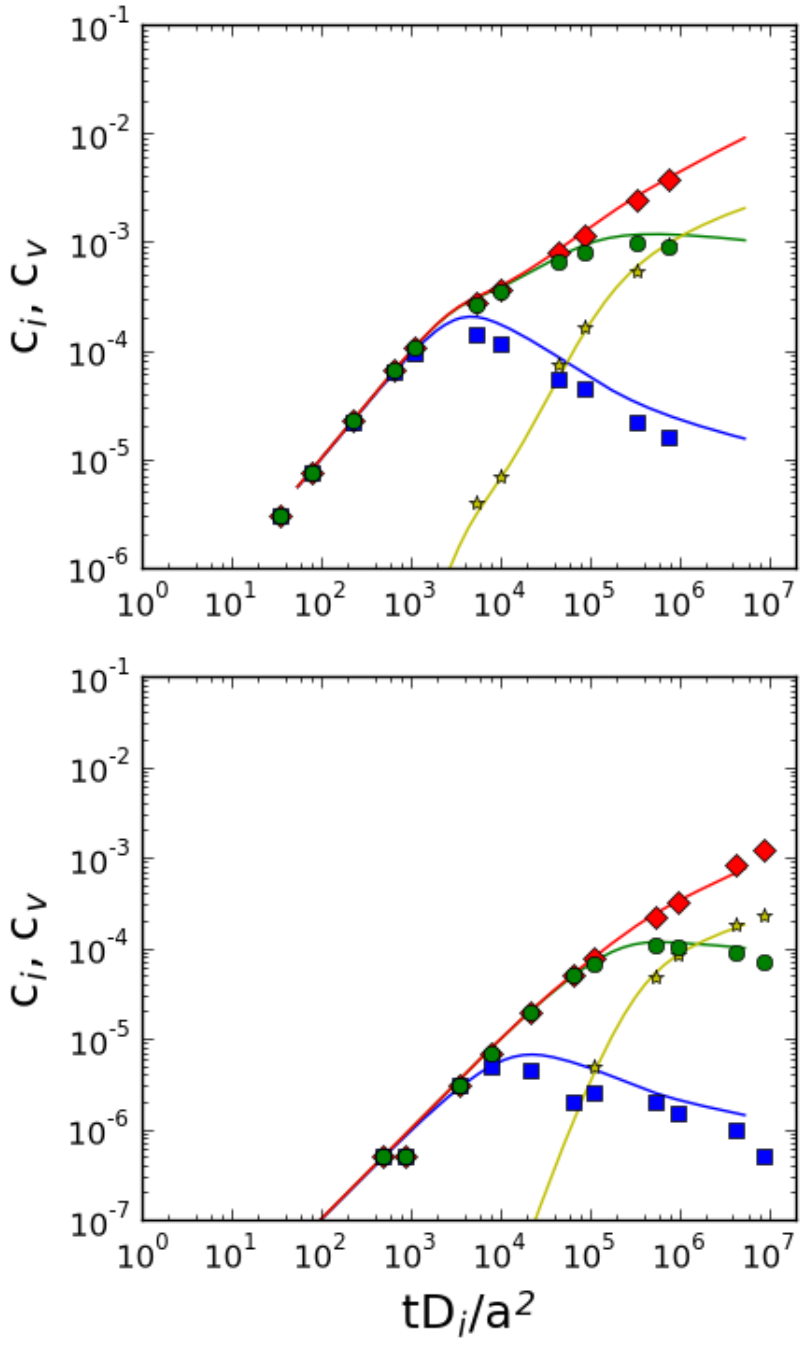

Figure 25: The results of the reversible voids simulation for two different values of σF (5.55×10^4 and 5.55×10^2). The detachment rate is assumed to be constant for all void sizes and is equal to $0.01 \times D_v$. The rate equations for voids are truncated after a void size of 20. The capture radius for voids is set to 2 times the value for simple defects.

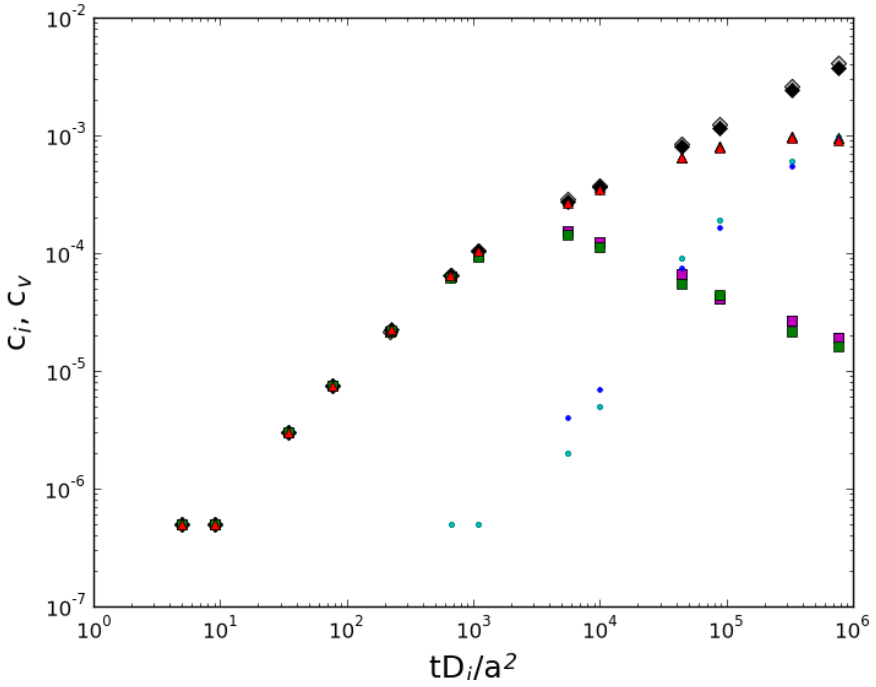

Figure 26: The results of the void detachment rates for different interatomic potentials are compared to the results for the constant barrier model and it is found that the difference between potentials and the constant barrier is minimal especially at long times.

likely sufficient for studies of both the concentrations of defects in bcc metals and the distribution of the size of voids.

4.4.2 Sensitivity Analysis

4.4.2.1 Simple Defects Model MOAT

We have calculated the average EE and standard deviation for both the concentration of interstitials n_i and vacancies n_v for each of the four parameters examined in the simple defect model: interstitial barrier $|EE|_{int}$, rotational barrier $|EE|_{rot}$, vacancy barrier $|EE|_{vac}$, and $|EE|_{sink}$. We then normalized the values of n_i and n_v by dividing each EE and standard deviation value by the average of the concentrations $mean(n_i)$ and $mean(n_v)$, respectively. Finally, we normalize all the concentrations and standard deviations by dividing by the max concentration $max(max(n_i), max(n_v))$ we then plot

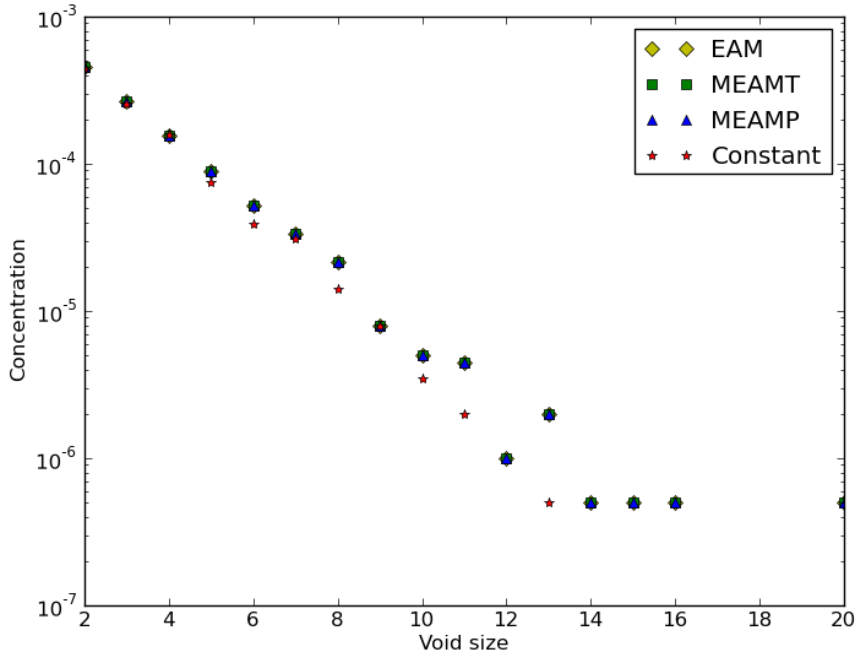

Figure 27: The results for the void sizes formed by different interatomic potentials are compared to the results for the constant barrier model and it is found that the difference between potentials and the constant barrier is minimal especially at long times.

the resulting values.

The $|EE|$ values are calculated for the KMC model in Figure 28. The plot is divided into three sections to the left of the vertical line is the region with values that have a negligible effect on the output, below the horizontal lines are values that have linear effects without interactions, and the remaining region contains those parameters with non-linear effects and/or interactions. Examination of the results shows that the model is most sensitive to the effect of the interstitial barrier on the concentration of interstitials. In addition the vacancy concentration is most dependent on the sink concentration input and the value for the interstitial barrier. These results also suggests the value of rotational barrier is largely irrelevant to the simulation. For the concentration of vacancies it has some importance when compared to other values effect on the vacancy concentration but the effect on the concentration of interstitials

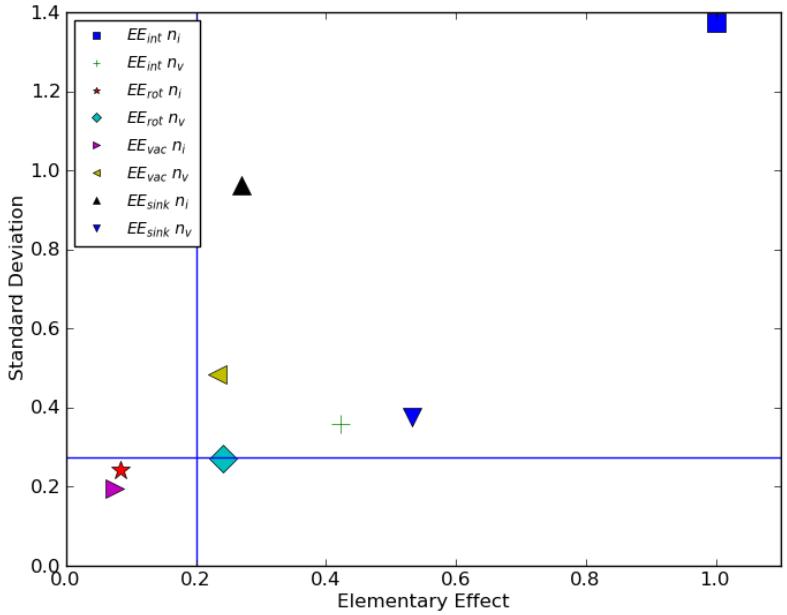

Figure 28: The $|EE|$ were calculated for the simple defect model using kMC. The most important factors are located in the upper left quadrant of the simulation.

is insignificant. Some of the remaining factors have some effect on the results but these are minor compared to the previously discussed factors.

Next we calculated the $|EE|$ values for the rate equations in order to compare the results to that of the kMC model. The results of these calculations are presented in figure 29. It is clear from these results that the sink concentration is too low to affect the mathematical model. In addition because of the low value the third term on the right side of Equation 26 is so small that the effect is negligible. This means that the results of the other parameters on the vacancy and interstitial concentrations are correlated. This suggests the use of $|EE|$ to examine the sensitivity of the model to input parameters is inadequate. Thus PRCCs will be used to better gauge the sensitivity of the model to input parameters.

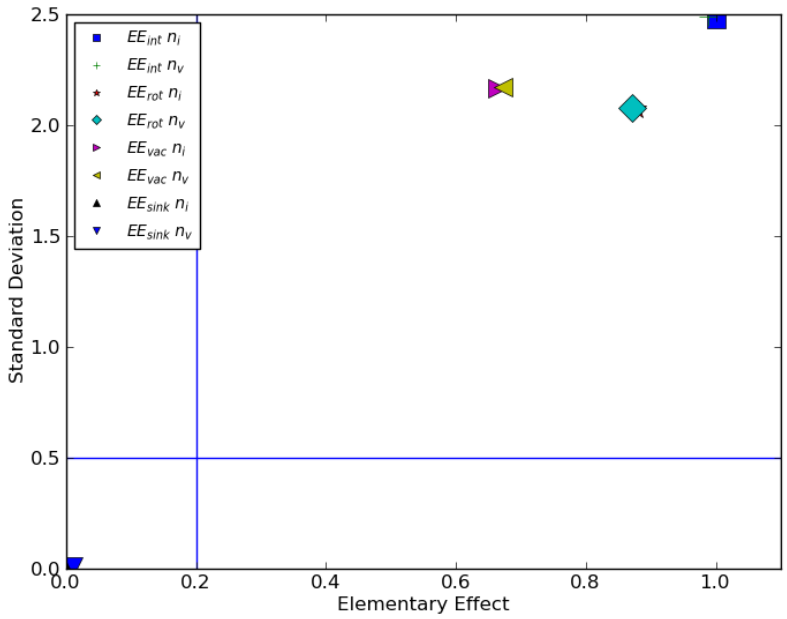

Figure 29: The $|EE|$ are calculated for the simple defect model using rate equations. Note that each of the input parameters have the same effect on the vacancy and interstitial terms this is due to the small value of the sink concentration which limits the third term in the equations.

4.4.2.2 Simple Defects Model PRCC

In order to examine the effect of input parameters on the concentration of vacancies and interstitials in rate equation models the PRCC between each input parameters and the outcome variables were calculated. The results of these calculations are contained in Table 13. Based on the results of these calculations it can be seen that for the vacancy concentration the sink concentration is the most important variable while the interstitial and vacancy barriers also have significant importance. However, for the interstitial concentration the interstitial and vacancy barriers are of the highest importance while the sink concentration also has a high importance. In both cases the rotational barrier is of little importance to the final result. These results are similar to those found using MOAT sensitivity analysis on kMC simulations. Perhaps the most important result from this is that the low importance for the rotational barrier suggests that the mechanism for the interstitial migration is generally not important for multiscale simulations and that models of bcc metals can be used independent of the particular metal attempting to be studied.

4.4.2.3 Irreversible Voids Model MOAT

We have calculated the average EE and standard deviation for both the concentration of interstitials, n_i, vacancies, n_v, and clusters, n_c, for each of the four parameters examined in the simple defect model: interstitial barrier $|EE|_{int}$, rotational barrier $|EE|_{rot}$, vacancy barrier $|EE|_{vac}$, and $|EE|_{sink}$. We then normalized the values of n_i, n_v, and n_c by dividing each EE and standard deviation value by the average of the concentrations $mean(n_i)$, $mean(n_v)$ and $mean(n_c)$, respectively. Finally, we normalize all the concentrations and standard deviations by dividing by the max concentration $max(max(n_i), max(n_v), max(n_c))$ we then plot the resulting values.

The $|EE|$ values are calculated for the KMC model in Figure 30. The plot is divided into three sections to the left of the vertical line is the region with values that

Table 13: PRCC values for the simple defect model using rate equations. The gamma value is the importance of the input parameter with positive meaning a direct relationship and negative meaning an inverse relationship. The p value is a measure of the confidence of the value.

	Vacancy Concentration	
Input Parameter	γ	p value
Rotational Barrier	-0.1623651	-0.0265
Interstitial Barrier	0.5333	9.336×10^{-9}
Vacancy Barrier	0.4544	1.809×10^{-6}
Sink Concentration	0.8776	2.208×10^{-33}
	Interstitial Concentration	
Input Parameter	γ	p value
Rotational Barrier	7.925484×10^{-1}	1.0476×10^{-1}
Interstitial Barrier	0.9806	7.070×10^{-72}
Vacancy Barrier	0.8341	2.491×10^{-27}
Sink Concentration	-0.6660	6.156×10^{-14}

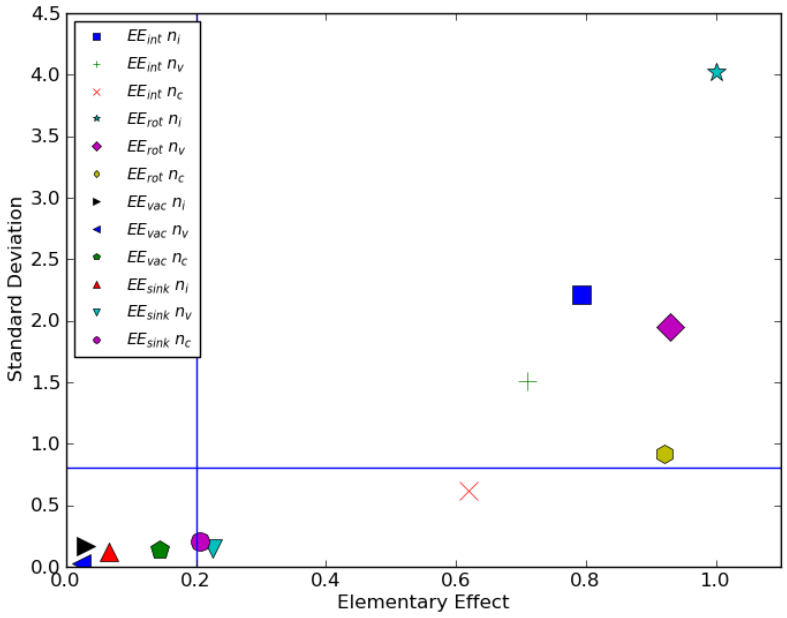

Figure 30: The $|EE|$ were calculated for the irreversible voids model using kMC. The most important factors are located in the upper left quadrant of the simulation.

have a negligible effect on the output, below the horizontal lines are values that have linear effects without interactions, and the remaining region contains those parameters with non-linear effects and/or interactions. Examination of the results shows that the model is most sensitive to the effect of the rotational barrier on the concentration of interstitials, vacancies, and clusters. This is in contrast to the simple model and suggests when clusters are included the behavior of the interstitial movement is important, thus the behavior of iron vs. other bcc metals should be accounted for. In addition the interstitial barrier is important for each of the defect types. These results also suggests the value of rotational barrier and sink concentration is largely irrelevant to the simulation. The change in importance of the rotational barrier is interesting and the use of rate equations may determine if this effect is consistent independent of the simulation model.

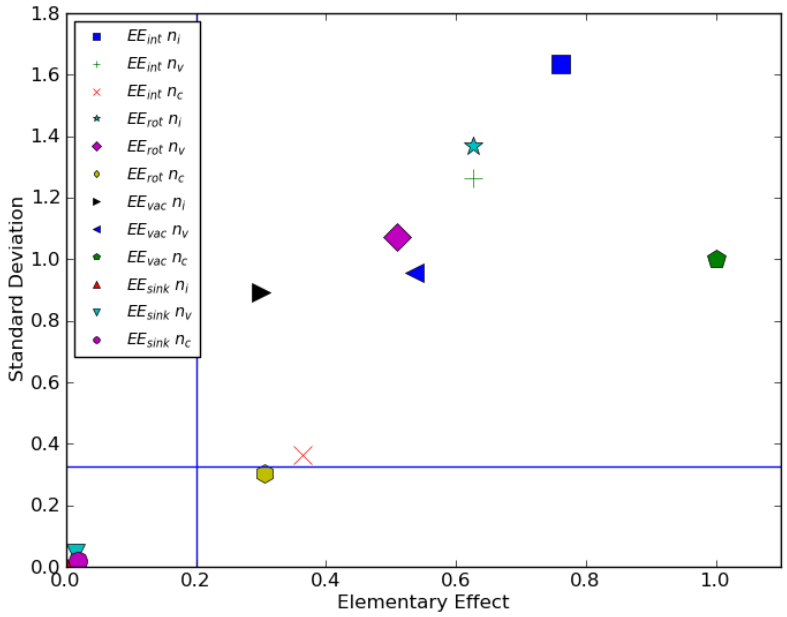

Figure 31: The $|EE|$ were calculated for the irreversible voids model using rate equations. The most important factors are located in the upper left quadrant of the simulation.

The $|EE|$ values are calculated for the rate equations in Figure 31.

4.5 Conclusions

In this section we have used kinetic Monte Carlo (kMC) simulations, within the SPPARKS framework, of increasing complexity to examine the behavior of defects in bcc metals with a particular interest in the treatment of voids. The simulations are compared to rate equations and previous published studies to determine the validity of the models. In addition, sensitivity analysis is performed on the simplest two models in order to determine the importance of the various input parameters and to begin an examination of how the introduction of increasingly complex defect structures affect the resulting importance of the parameters. The first model studied examines only the behavior of simple defects and shows excellent agreement with rate equations studies.

The second model introduces irreversible vacancy clusters and again provides excellent agreement at low concentrations, however, some discrepancies arise in the behavior of the capture radius for the rate equations that merits further investigation. The third model introduces the possibility of vacancies spontaneously being emitted by clusters. It is found that the results for a constant barrier are nearly identical for both the kMC simulation and rate equations assuming the same capture radius from the irreversible voids model. It should be noted that the size distribution of this model results in an average value of void size nearly identical to the irreversible model suggesting that this level of complexity does not gain in accuracy at long time intervals over simpler models. As a final addition we assume that the rate at which vacancies leave clusters is not a constant but instead dependent on the size of the cluster. For this method the rate for different cluster sizes is found through several different interatomic potentials using Molecular Dynamics.

The final two methods are compared to one another in order to determine the sensitivity of the model to size dependent cluster detachment rates. It is found that due to the small size of the resulting cluster there is little difference in the resulting

cluster densities. In addition examination of the cluster size using both methods suggests there is little difference between constant barrier and size dependent barriers for void detachment rates. These results suggests that a constant barrier, informed by the results from atomistic studies is generally sufficient to model the behavior of voids in bcc metals.

Sensitivity analysis was performed using MOAT on both the rate equation and kMC models for the models involving only simple defects and simple defects with irreversible voids. While the results of each model varied there were some similarities between the models. In all cases the effect of the interstitial migration barrier on the concentration of interstitials was moderately to very important. In addition the sink density had a low importance in each of the models. Based on the results of MOAT analysis the rotational barrier was only highly important on any defect concentration in the irreversible voids model with kMC. Otherwise it was of moderate to little importance.

Additionally, sensitivity analysis using PRCCs was performed on the simple defect model using rate equations as the MOAT analysis was unable to accurately separate the different input parameters' importance due to the small effect from the sink concentration. This analysis showed similar results to those of the MOAT analysis for the kMC model suggesting that the results from the MOAT when able to be performed correctly is an accurate measurement of the sensitivity of input parameters in this model.

CHAPTER V

NUCLEAR FUEL POTTS MODEL

5.1 Introduction

As nuclear fuel is irradiated in reactors the lattice experiences a high number of displacements per atom. This process is not uniform throughout the fuel and due to geometrical considerations of the reactor setup the outer edges of the fuel experiences significantly more irradiation damage then the center of the fuel. Over time this creates a localized burn-up level higher on the rim of the fuel. In turn this damage causes a restructuring of the grains in the outer edge of the fuel. The new grain structure is known as High Burn-up Structure (HBS) [165]. This structure was initially discovered in the 1950s and 1960s [13, 22, 24] during initial experimentation in nuclear fuels. At this time it was not studied in detail due to fears it caused release of fission gases and the low Burn-up levels reached in commercial reactors of the time [113, 165]. It was examined again in the 1980s and 1990s in a series of works looking to examine its properties [14, 12, 142, 99, 94, 180].

Based on recent studies [93, 191, 183, 185] there is general agreement that the release of fission gases in reactors does not occur in the HBS region. In fact the interconnection of intergranular bubbles formed by the fission gases in this region is conducive to retention of these gases. There is also additional evidence that HBS provides other characteristics for UO_2 fuel that is either beneficial or neutral to its performance. One advantage is that the restructured grains are softer and tougher then traditional fuels which can relieve mechanical stresses from the fuel cladding interaction [181]. Another concern of HBS was a reduction in thermal conductivity due to increased grain boundary and porosity. However, this effect is mitigated by a

reduction in the amount of defects contained in the new grains [164].

The formation mechanism of HBS structure is still a mystery [165]. In this work we propose to extend a model of the formation based on the Potts model [138]. Our model will focus on the behavior of the lattice parameter expansion in order to create a model that simulates the behavior of the lattice under irradiation appropriately. Finally, we will present results of the new model for uranium silicide fuel in addition to the standard uranium dioxide fuel.

5.2 Related Works

5.2.1 Mathematical Models

Previous studies involving the formation and behavior of HBS in nuclear fuels have primarily focused on mathematical models, in particular the use of rate equations is prevalent. While many of these models are able to accurately predict the behavior of the HBS and fission gas bubbles on the macroscopic scale they lack the ability to examine the evolution of HBS on a step by step scale. Presented here is a brief examination of mathematical models that have been performed on the behavior of HBS and fission gases in nuclear fuels to date.

Rest [158, 152, 153, 155, 157] presents a series of increasingly complex models using coupled differential equations to examine the behavior of bubbles, porosity and HBS in U_3Si, U_3Si_2, UO_2, and U-Mo fuels.

Lassmann *et al.* [102] present a simple model to determine the thickness of the HBS zone and the Xe depletion using the differential equation based TUBRNP model, part of the TRANSURANUS model.

Rest and Hofman [159, 161, 162, 156] present models using coupled differential equations to examine the bubble distribution, change in lattice parameter, grain size, and other properties of HBS formation in U_3Si_2, UO_2, and U-Mo fuels.

Kinoshita [92] presents a model which uses differential equations to examine defect

behavior in UO_2 fuels. In addition Kinoshita *et al.* [95] suggests using density functional theory and molecular dynamics calculations to examine the defect behavior in these fuels.

Baron *et al.* [15] present a mathematical model for simulating the behavior of xenon in UO_2 fuels.

Spino *et al.* [184] presents a model which uses differential equations to examine the fuel density, porosity, and retained Xe-concentration in UO_2 fuels.

Xiao and Long [202] present a model on the coarsening behavior of fission gas pores in the HBS structure of UO_2 fuels based on a mathematical model using differential equations.

5.2.2 Potts Model

Our model is an extension of the Potts model which is a generalized form of the Ising model originally applied to magnetic domain problems[147]. However, it has since been applied to the problem of grain growth[169, 4, 61, 80, 37, 201, 79]. In addition it has been used to model recrystallization[187, 188, 163, 78, 84] which will be implemented in this model. Additionally it has been used to simulate porosity and bubble migration in materials, in particular UO_2[190].

5.3 Model

The model in its current form has been implemented for a 2D triangular lattice and would need modification of the energy term to work on a wider range of geometries. As such each site is hexagonal in shape. The model is a modification of the Potts model where each lattice site is a part of a grain with a particular spin representing the orientation of the grain. In addition the model incorporates HBS grains, which follow the same dynamics as the ordinary grains, and bubble sites, which incorporate diffusion dynamics instead. The size of a site is determined by the size of a nanobubble found in UO_2 grains [138], which is assumed to be 40 nm.

Each grain site has two integer values associated with it. The first value is associated with the orientation of the grain and there are assumed to be Q states with which this value can take, where Q is large enough that the grains can assumed to be independent. The second integer value is related to the type of grain, thus it can have two values: one for an ordinary grain and one for an HBS grain. Thus there are a total of 2Q states that the grains can occupy. Any neighboring sites with the same state are assumed to be part of the same grain. An example of this is given in Figure 32 In addition bubble sites are given there own state for a total of 2Q +1 possible states within the system.

As mentioned in literature, due to their smaller size and the recrystallization process, HBS grains have a lower dislocation density [165] then normal grains under irradiation. Thus, the energy of the system and as a result, the evolution of the HBS grain structure is controlled by two competing factors: the increased grain boundary energy and decreased stored strain energy. The total energy of the system, G, is given by [138]:

$$G = \sum_{i}^{M} \left[Hf(S_i) + \frac{J}{2} \sum_{j}^{nn} (1 - \delta_{S_i S_j}) \right] \tag{43}$$

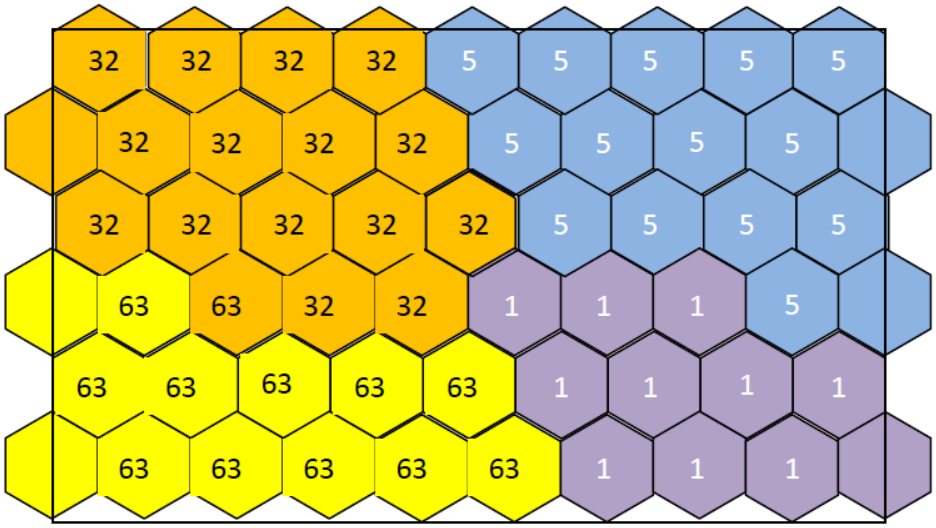

Figure 32: The grains (different colors) are represented on the triangular lattice. Each site is hexagonal in shape and has a value associated representing the grain boundary angle.

where M is the total number of lattice sites, nn is the number of nearest neighbors, f is 1 for ordinary grains and 0 for HBS grains S_i is the current site and S_j a neighboring site. J and H are the boundary energy and stored energy respectively. The equation for J and H are given by:

$$J = \begin{cases} \sqrt{2}\gamma_S b_v \sqrt{\rho_N} S & \text{for grain boundary} \\ \gamma_S S & \text{for pore surface} \end{cases} \tag{44}$$

$$H = \frac{1}{2}\left(\frac{\Delta a}{a}\right) EA \tag{45}$$

where γ_S is the surface energy, b_v is the burgers vector ρ_N is the dislocation density, S is the contact length between sites, $\Delta a/a$ is the change in lattice parameter, E is the elastic modulus and A is the site area. The values for these input parameters for UO_2 and U_3Si_2 are given in Table 14. It is important to note that because the simulation is only 2 dimensional the units of these values do not match those of the thermal energy and thus this value requires reduced units which are mentioned whenever applicable.

Table 14: Input parameters and source for UO_2 and U_3Si_2. Several of these parameters are dependent on Temperature (T) which is assumed to be 923K, a typical value for reactors.

Parameter	UO_2 value	source	U_3Si_2 value	source
γ_S	$0.85 - 1.4 \times 10^{-4}$T	[70]	$0.7eV$	[154]
b_v	$\frac{\sqrt{2}}{2}a$	[157]	3.9Å	[a]
ρ_N	$\begin{cases} 10^{0.022 \cdot \mathrm{Bu}+13.8} & \text{for Bu} \leq 44 \\ 5.86 \times 10^{14} & \text{for Bu} > 44 \end{cases}$	[133]	1.43×10^9	[160]
S		[a]		[a]
$\frac{\Delta a}{a}$	$12.43 \times 10^{-4}(1 + \frac{0.060e^{-0.042 \cdot \mathrm{Bu}} - 0.042e^{-0.060 \cdot \mathrm{Bu}}}{0.042-0.060})$	[182]	$(3.88008 \cdot \mathrm{Bu}^2 + 0.79811 \cdot \mathrm{Bu})^{1/3}$	[122]
E	$2 \times 10^{11}(1 - 1.09154 \times 10^{-4}T)$	[157]	1.63×10^{11}	[198]
A		[a]		[a]

[a] from geometric considerations

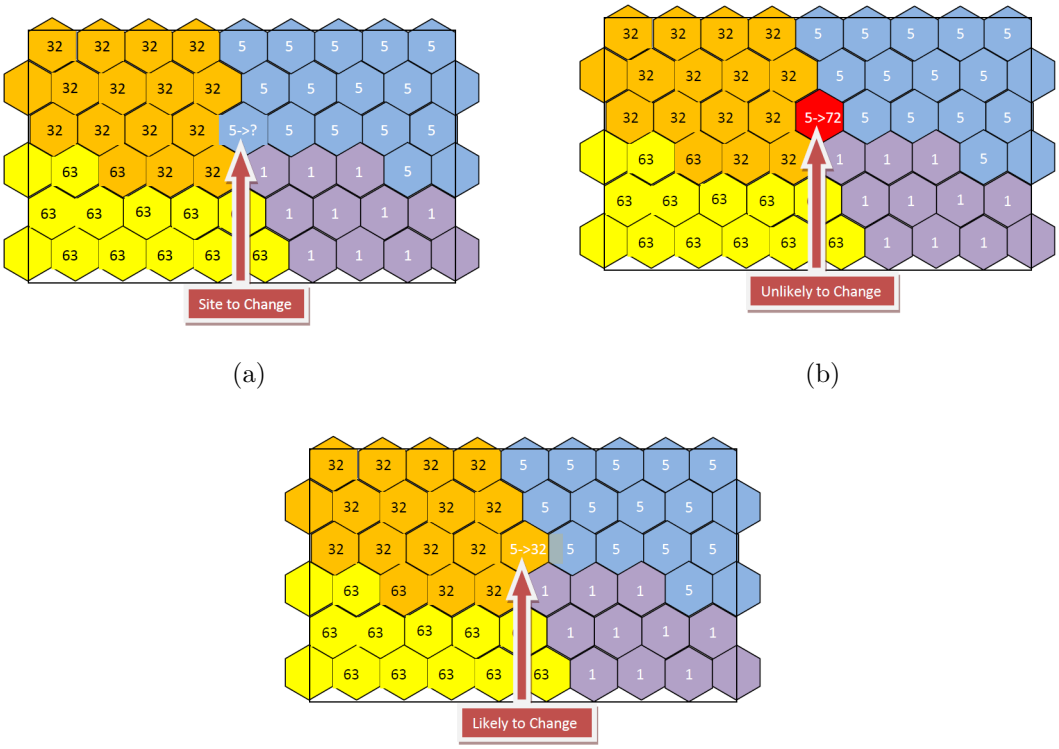

(a) (b) (c)

Figure 33: (a) A site is chosen on which to perform a grain growth/HBS recrystallization event. First there is an attempt to convert the site to a fission gas bubble. Then the energy of the site is calculated. (b) A new site value is chosen and the new energy is calculated. For wild flips the site will only change when the internal energy surpasses the boundary energy. (c) However, if the new state is the same as a neighbor site the event will be accepted as long as the energy of the system is lowered.

In this model we use a rejection based kMC method to compare with other similar simulations. In this case each site is tested and the probability of a state change is determined based on equation 7. As with other Potts model simulations of grain growth [190] it is assumed that only those grain growth events which lower or leave unchanged the total energy of the system are successful (this corresponds to a 0 temperature simulation). A pictorial representation of this process is presented in figure 33.

In addition to the grain growth elements described previously, the bubbles are now inserted into the simulation. Bubbles are inserted as part of the standard rkMC procedure. The probability of a bubble insertion occurring is based on the experimentally measured porosity, which for UO_2[185] and U_3Si_2[158] is given respectively by the equations:

$$P(\%) = \begin{cases} 0.06 \cdot \text{Bu} & \text{for} \quad \text{Bu} \leq 60 \\ -6.6 + 0.17 \cdot \text{Bu} & \text{for } 60 < \text{Bu} \leq 100 \\ 4.4 + 0.06 \cdot \text{Bu} & \text{for} \quad \text{Bu} > 100 \end{cases} \tag{46}$$

$$P(\%) = 0.044 \cdot \text{Bu} \tag{47}$$

If a bubble event is chosen the bubble is randomly inserted into the lattice. Bubble migration occurs differently in the simulation then grain growth. The migration is a diffusion event. This means that the energy of the system is calculated and an attempt is made to switch the bubble site with a neighboring site, thus leaving the number of bubble sites unchanged. As mentioned in previous works [190] if the original bubble site is changed to the neighboring site this assumes that the system retains knowledge of what was at that site which is not a physical result. Thus instead of simply switching sites, the state of the old bubble site is chosen by selecting one of the neighboring sites' state that results in the minimum energy and the new system

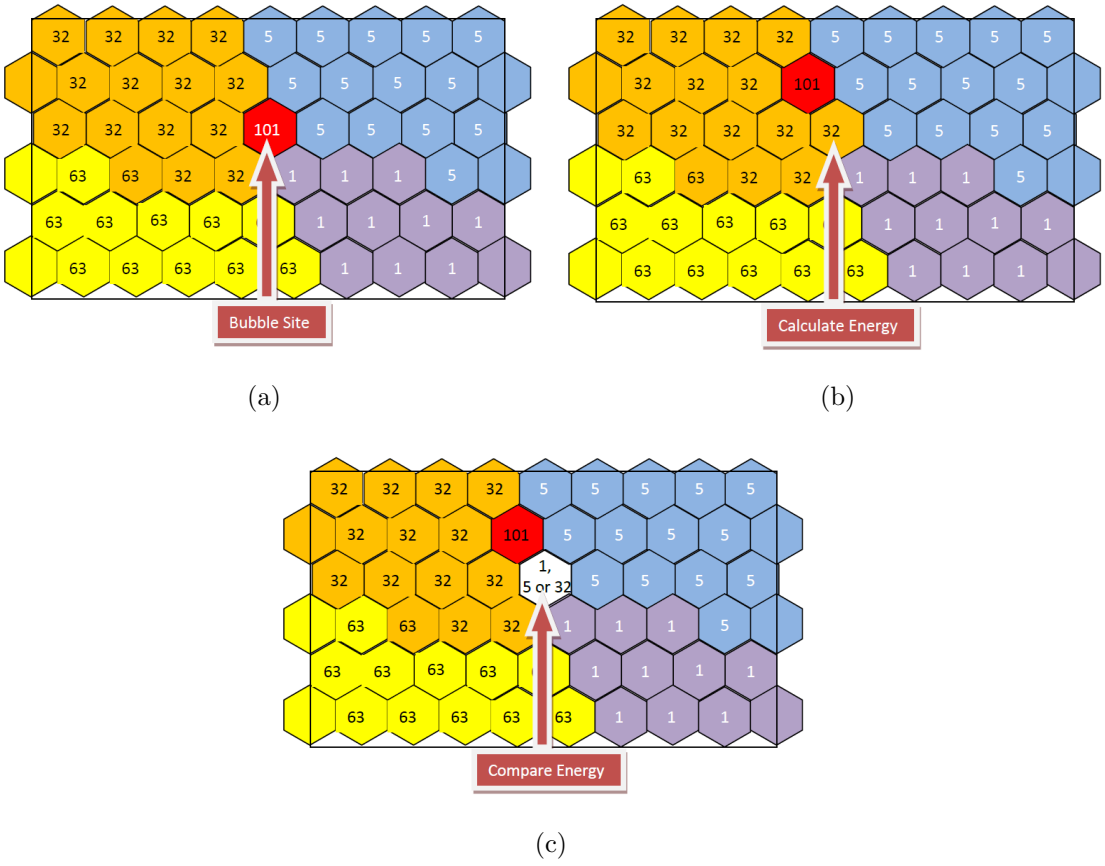

(a) (b) (c)

Figure 34: (a) A bubble site is chosen and the energy of the site is calculated. (b) A neighboring non-bubble site is chosen and the energy of the site is calculated before the states are switched. (c) A neighboring state is chosen so that the energy is minimized and the new energy of the system is calculated. The event is then accepted or rejected.

energy is then calculated. A pictorial representation of this process is presented in figure 34. The probability of a jump is then calculated using Eq 7 assuming the value for $k_BT = 0.7J$. In addition it is assumed that the mobility of bubbles is faster than that of grain growth. Specifically we attempt 10 bubble migrations for each cycle of grain growth events.

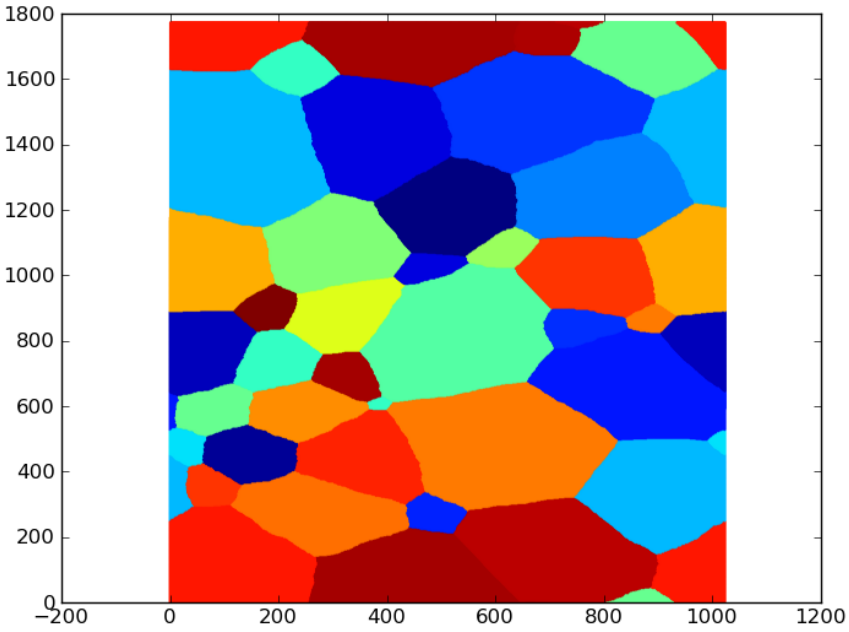

Figure 35: Virgin grain structure used for simulation of the Potts model in all subsequent simulations. The average grain size is between 9 and 10 μm

5.4 Results

5.4.1 High Burnup Structure Formation in Porous Uranium Dioxide

5.4.1.1 rejection kMC for uranium dioxide

We begin by validating the model by comparing it to a similar model. Oh *et al.* [138] created a Potts model to calculate the HBS formation in UO_2 using the same method for calculating the energy as we used. However, their model uses the change in lattice parameter due to annealing instead of the change due to irradiation. The equation for this lattice change is given by $\Delta a/a = 1.57 \times 10^{-5} Bu$. When we substitute this parameter into our model without the use of bubbles to simulate the evolution of the original UO_2 grain structure (figure 35) we get similar results to theirs (figure 36). However, in calculating this value we also needed to divide the value for the grain boundary energy by a factor of two. This may correspond to calculating the change in energy for the current site while ignoring the resulting change in energy

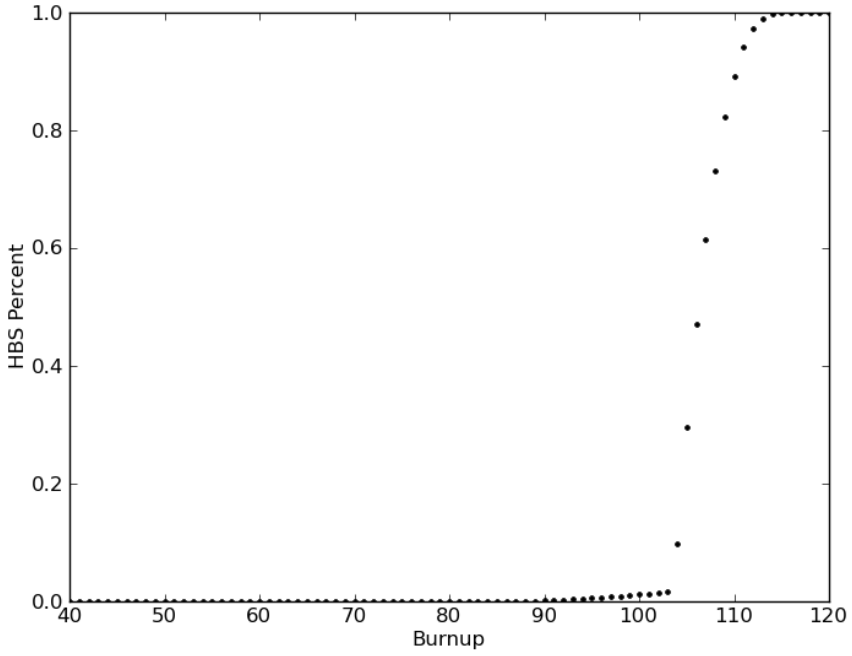

Figure 36: Comparison of Potts model of UO_2 with previously published literature[138]. In this simulation the bubble condition is turned off and the lattice parameter expansion equation used is for annealed fuels.

for neighboring sites. The reason this was done is unknown and the appropriate calculation of the system energy value is used in all subsequent simulations.

In examining this model we can see certain characteristics occurring, we note that no HBS is formed until Bu = 85. At this point the value of H is more than 2J which corresponds to the energy change required to make HBS formation energetically favorable at grain boundary tri-junctions, that this is indeed where the formation occurs can be seen in figure 37, which shows the grain structure at a local burnup of 95 GWD/MTU with HBS shaded black. At a burnup level of 104 GWD/MTU the value of H is now greater than 3J and HBS will begin to spread out from these junction sites and other grain boundaries to the rest of the grain (figure 38 at a burnup of 106 GWD/MTU).

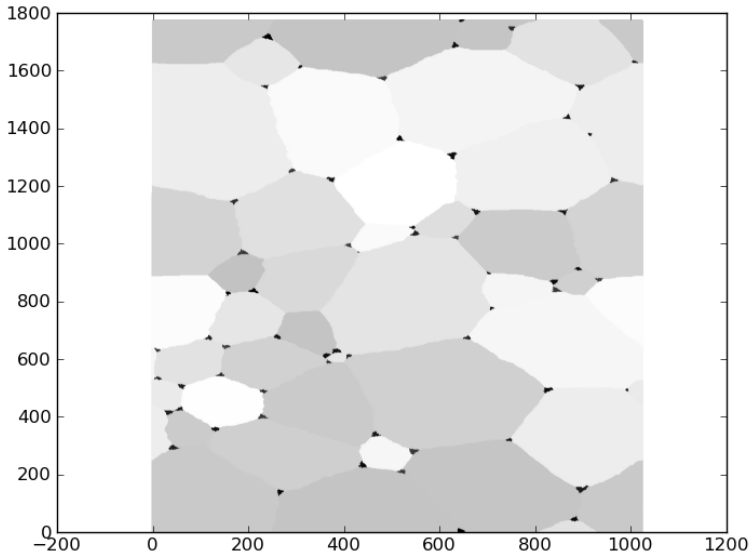

Figure 37: The grain structure at 95 GWD/MTU simulated burnup with no bubbles using parameter values found in literature. Note that the formation of HBS at this point is limited to the areas surrounding tri-junctions.

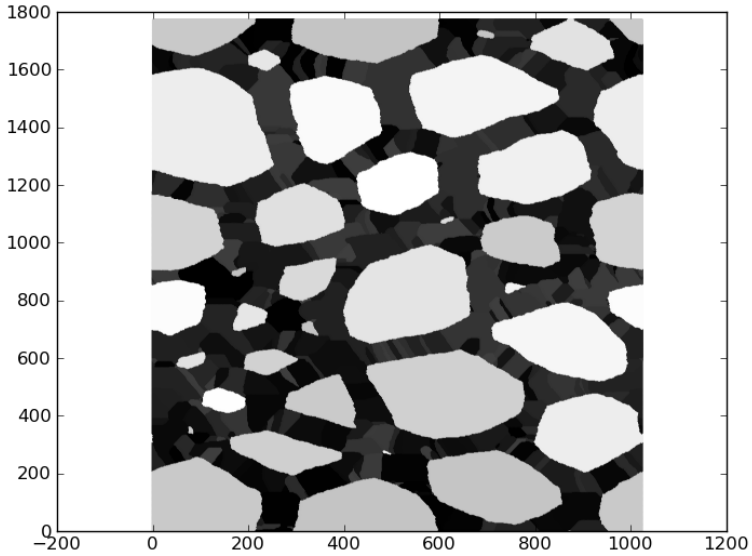

Figure 38: The grain structure at 106 GWD/MTU simulated burnup with no bubbles using parameter values found in literature. Note that the formation of HBS at this point has begun to spread out from all grain boundaries.

An attempt was made to replicate the bubble conditions found in Oh *et al.* . However, our model is unable to accurately reflect the exact behavior of this model. Instead we assume the bubble movement follows the procedure described by Tikare *et al.* [190] that was described in the previous section and we move to examine the behavior of UO_2 using the lattice parameter change representative of irradiation in a reactor [182].

Initially we examine the behavior of UO_2 with the conditions for bubble formation and migration turned off. The values of the input parameters used in this and all subsequent simulations, except where noted, are found in Table 14. For this simulation we ran to a local burnup of 115 GWD/MTU and tracked the percentage of the original grain structure that had turned to HBS as well as the average lattice parameter. The average lattice parameter is calculated assuming that ordinary grain sites would see an expansion of their lattice parameter based on fission damage (the first term in the equation for $\Delta a/a$ in Table 14) and the α damage (the second term

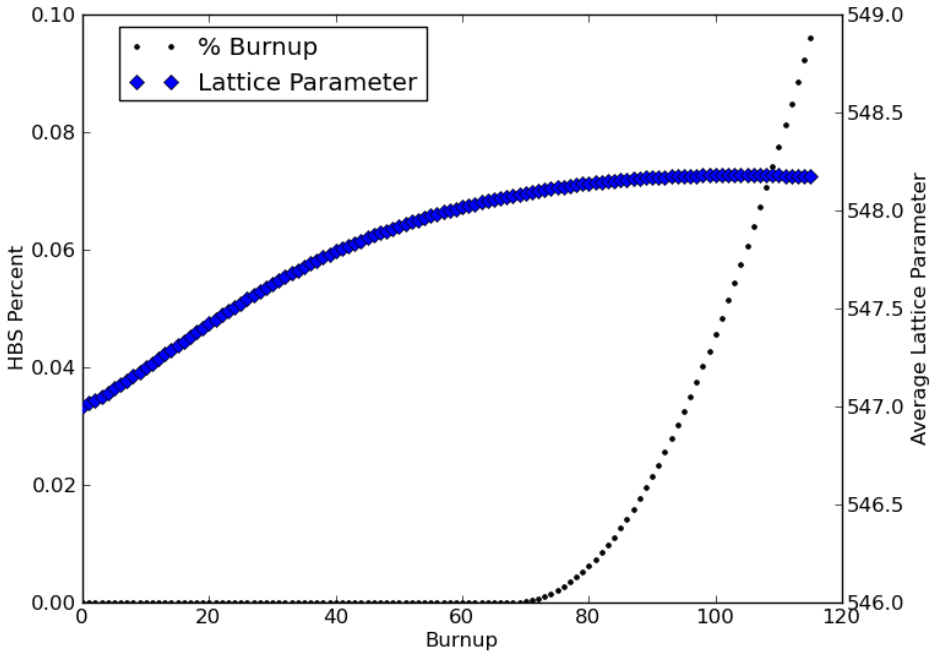

Figure 39: The simulation of UO_2 fuel under irradiation with no bubble growth. Note that the formation of HBS begins at approximately 70 GWD/MTU and progresses slowly to the point that the HBS fraction at 115 GWD/MTU is only about 10%, resulting in no lattice contraction as seen in experiment.

in the table), while HBS sites would have only the alpha damage contribution remain. Thus we would expect the behavior of the lattice parameter to mirror that found in Spino *et al.* [182]. The results of this simulation are presented in figure 39. It is clear that without the bubbles introduced into the simulation the HBS structure is unable to form until well past the local burnup expected based on experimental results.

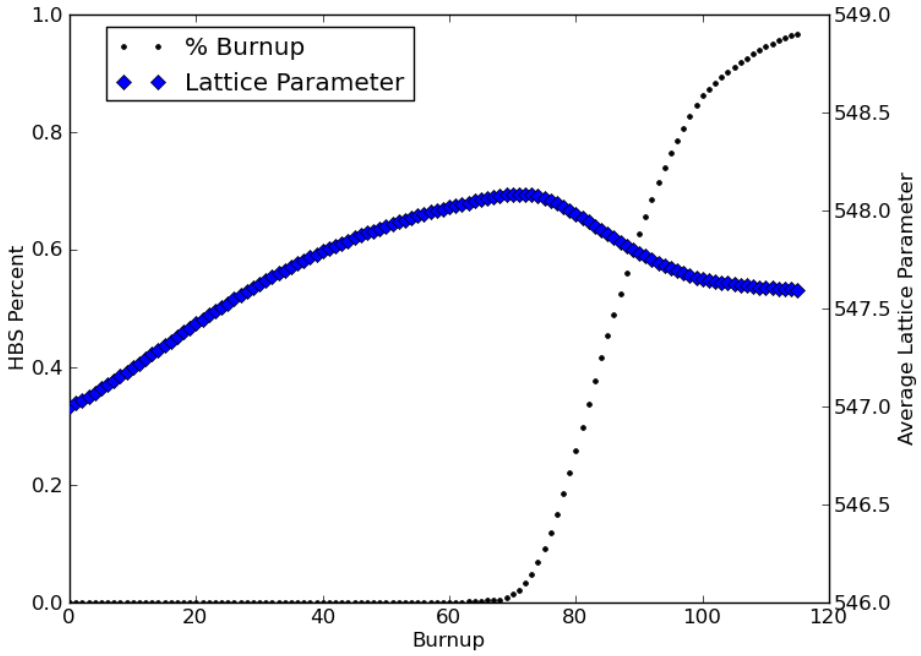

Figure 40: The simulation of UO_2 fuel under irradiation with no bubble growth. A small amount of HBS is formed due to local bubble geometry below 70 GWD/MTU. Unlike in the no bubble case, the increased grain boundaries due to the presence of bubbles causes an increase in the rate of HBS formation. This results in a drop in lattice parameter at 73 GWD/MTU local burnup similar to experiment.

We now turn to the full simulation including the introduction of bubbles in order to determine if this simulation is able to accurately model the behavior of the UO_2 fuel's HBS formation. Again we track the percent of the fuel that is now HBS structure as well as change in the average lattice parameter using the same assumptions as above. The results of the simulation are given in figure 40. From this we see that the introduction of bubbles results in a small amount of HBS structure forming between

60 and 70 GWD/MTU local burnup with the rest of the grain transforming rapidly above 73 GWD/MTU, resulting in a sudden decrease in the lattice parameter. These result agree with Spino *et al.* although further examination of the method that causes the change in lattice parameter may be needed as the decrease is potentially shallow when compared to experimental results.

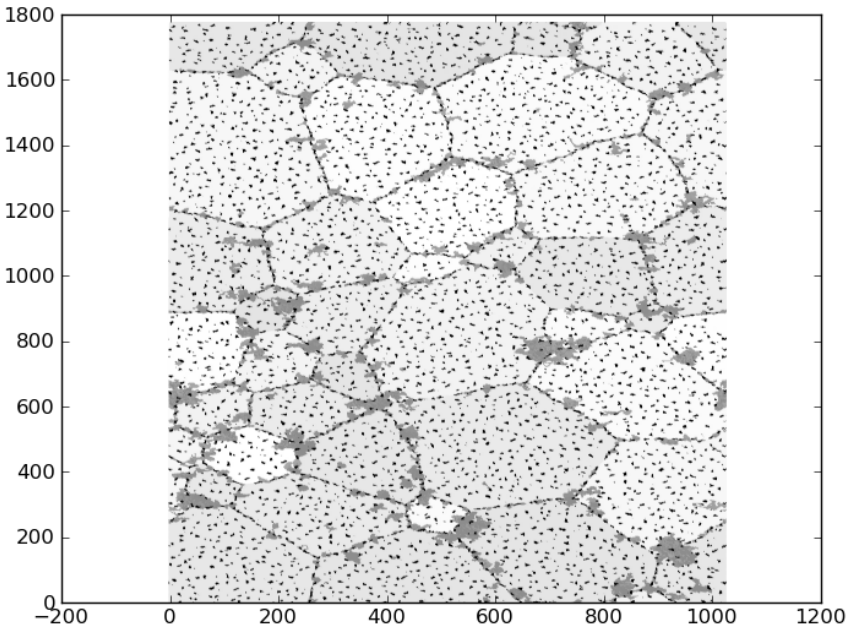

Figure 41: The grain structure at 75 GWD/MTU simulated burnup with no bubbles using parameter values for irradiated fuels. Not the formation of small bubbles on grain boundaries and in the fuel. The bubbles help to create HBS near grain boundaries and between bubble clusters.

Examining the structure of the bubble that have formed in the grain structure at 75 GWD/MTU (figure 41) we can see that a large number of small bubbles have formed in the structure. The distribution of bubbles at this burnup is given in figure 42. In this we have assumed the resolution of bubbles is 100nm, which is the resolution of an SEM with 1000x magnification. THus bubbles with smaller than six members were removed from the count. If we assume none of the smaller bubbles diffuse to other bubble sites post irradiation the average bubble diameter is $0.65\mu m$, below

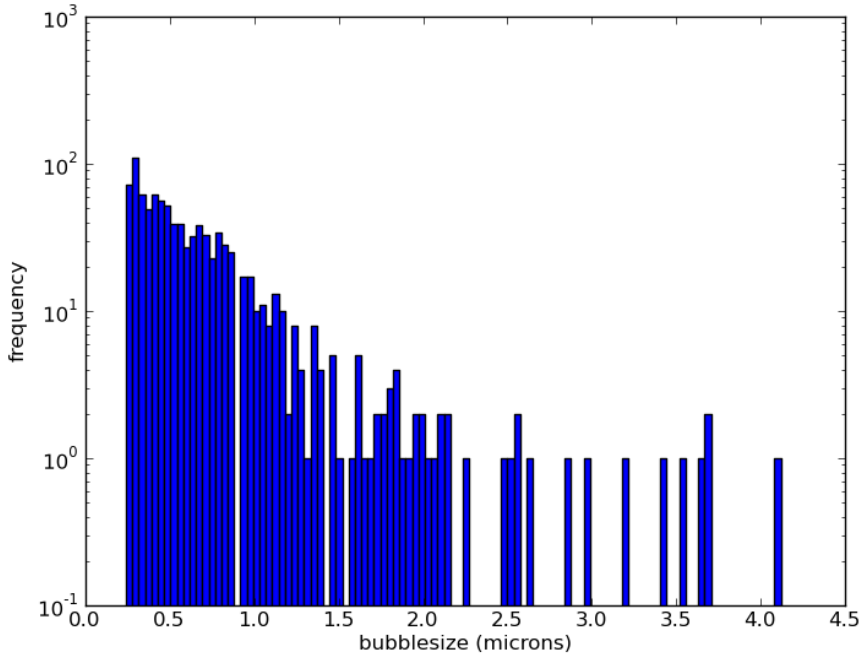

Figure 42: The bubble distribution at 75 GWD/MTU local burnup. It was assumed that the resolution of bubbles was approximately 100 nm, which is the resolution of an SEM with 1000x magnification. The resulting average cluster size is $0.65\mu m$.

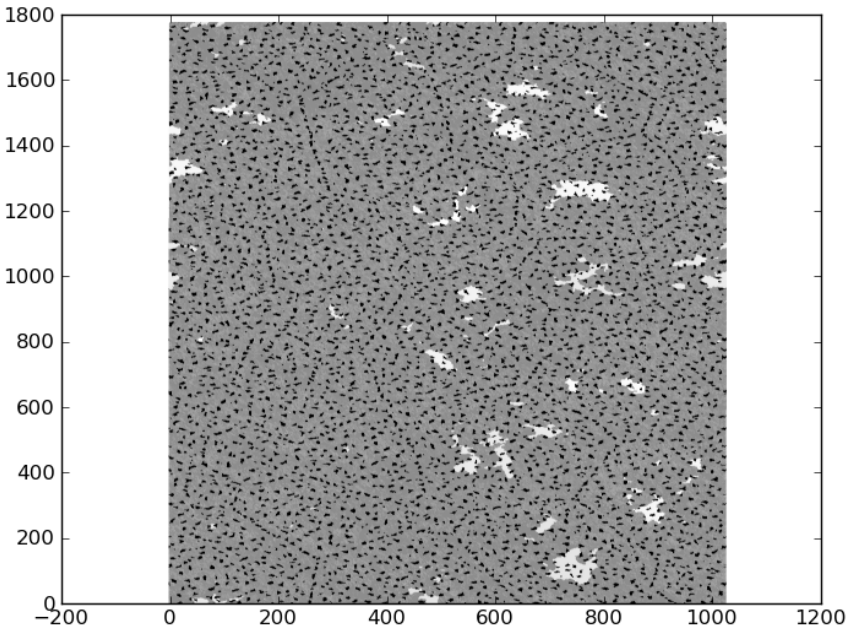

Figure 43: The grain structure at 115 GWD/MTU simulated burnup with no bubbles using parameter values for irradiated UO_2. Nearly the entire original grain structure is gone and the bubbles have begun to coarsen.

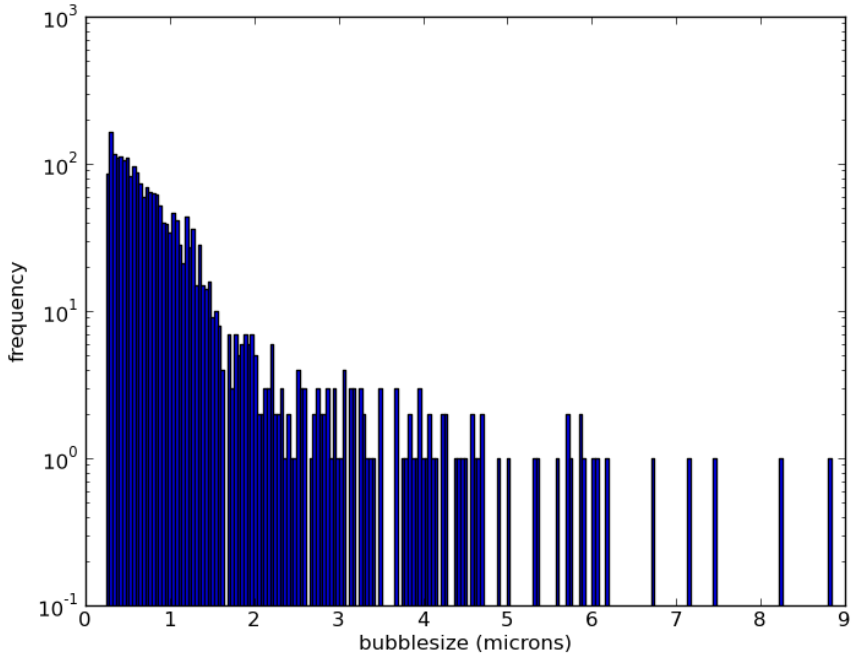

Figure 44: The bubble distribution at 115 GWD/MTU local burnup. It was assumed that the resolution of bubbles was approximately 100 nm, which is the resolution of an SEM with 1000x magnification. The resulting average cluster size is $0.87\mu m$.

the value given in Spino *et al.* [185] of $1.0\mu m$. However, it is believed that the bubbles coarsen after the HBS structure has formed so we again examine the structure after 115 GWD/MTU (figure 43) and find, again ignoring bubbles smaller than 100 nm, that the average bubble diameter is $0.87\mu m$ still below the value predicted by experiment but showing signs of coarsening bubbles. In addition the plots share characteristics with those of experiment including a tail of increasingly larger bubble diameters. Considering the rudimentary nature of bubble motion and processes in our simulation further agreement is not necessarily expected.

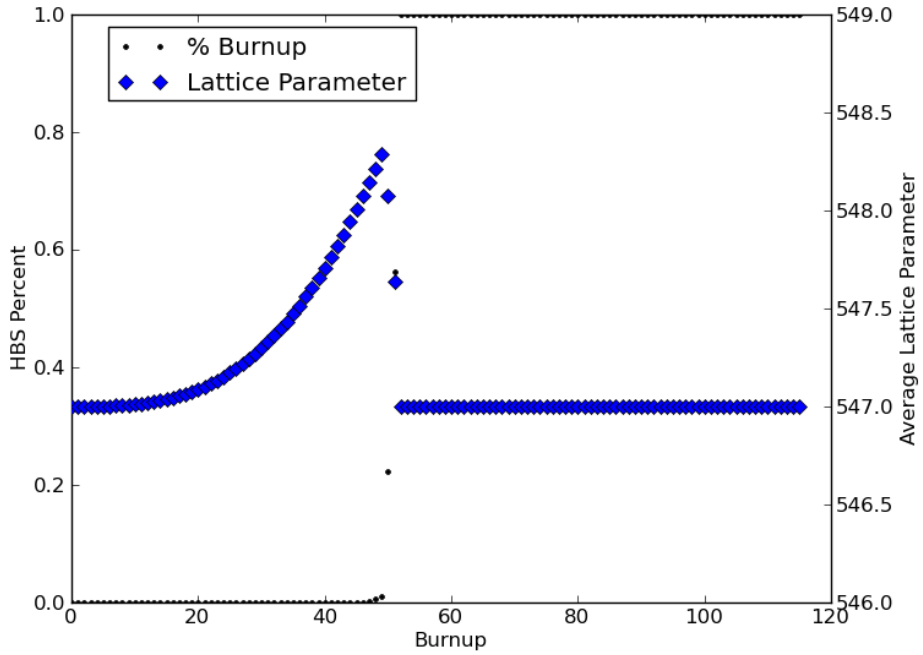

Figure 45: Simulation of UO_2 fuel under irradiation assuming dislocations size and density are the cause of the lattice parameter expansion. Note that the lattice expansion curve is exponential until it reaches a point where burnup is nearly immediate and then drops.

So far we have assumed the damage is a result of individual defects formed from the irradiation processes. Instead we examine an alternate theory [182] for the change in the lattice constant based on the formation of dislocation loops of increasing size in the grains. In this case the dislocation loops would expand continuously in the fuel

until they reach a saturation point at which they are of comparable size to that of the grains in which case they would no longer grow and the large size would result in the formation of HBS. Using the equation for the relative change in lattice parameter due to dislocation loops[182] and the values for dislocation loop and density found in Rest *et al.* [162] we found another equation for the change in lattice parameter:

$$\frac{\Delta a}{a} = \begin{cases} 2.19 \times 10^{-8} \cdot Bu^3 & \text{for Bu} \leq 60 \\ 0.00436 & \text{for Bu} > 60 \end{cases} \tag{48}$$

which we used in our simulation (figure 45). From this we see that the behavior of the lattice parameter at low temperatures is not consistent with experiment nor is the location of the start of large scale HBS formation which results in a lattice parameter contraction. This suggests that although the size and quantity of the dislocation loops is consistent with them causing the formation of HBS structure in this model they do not accurately represent the behavior of the lattice parameter and cannot be used to simulate the formation of HBS structure.

A third method for calculating the rate of lattice expansion in Spino *et al.* suggests the swelling is due to the increase in the number of excess vacancies in the fuel. From this, a linear relationship between the change in lattice parameter and the burnup is calculated based on swelling data in Olander [139] where if we assume a lack of gaseous elements in the solid fuel structure is given by:

$$\frac{\Delta a}{a} = 4.64 \times 10^{-5} \cdot Bu \tag{49}$$

The results of this simulation is given in figure 46. Again it is found that the fuel forms HBS too early and the resulting shape for the lattice parameter curve does not match experimental results. Thus an assumption that the change in lattice parameter is due to a combination of α and fission damage that saturates over time is the best fit for simulating the behavior of HBS formation in UO_2 fuels.

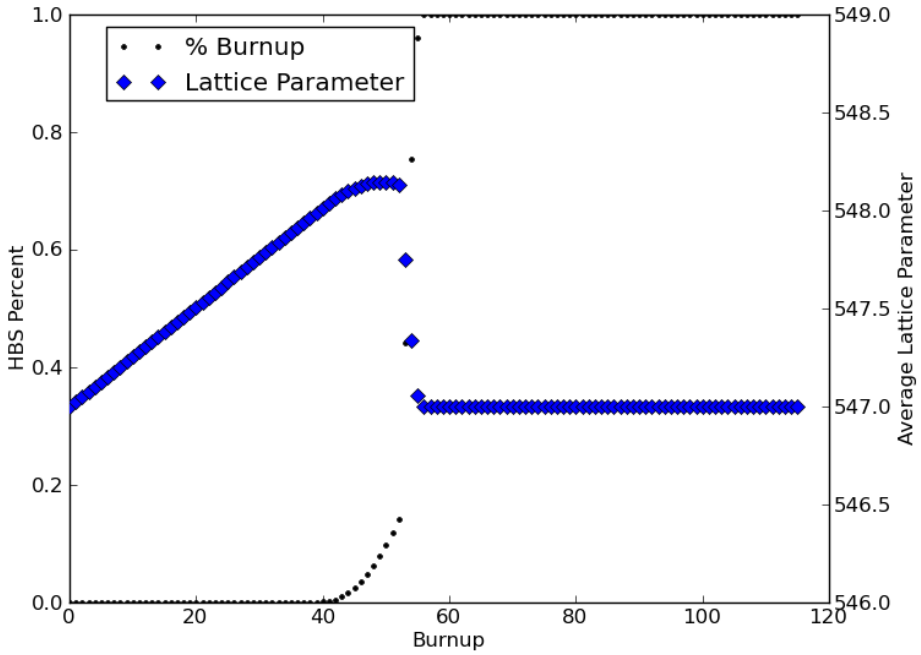

Figure 46: Simulation of UO_2 fuel under irradiation assuming excess vacancies are the cause of the lattice parameter expansion. Note that the lattice expansion curve is linear until it reaches a point where burnup is gradual before dropping nearly immediately.

5.4.1.2 rejection kMC for uranium silicide

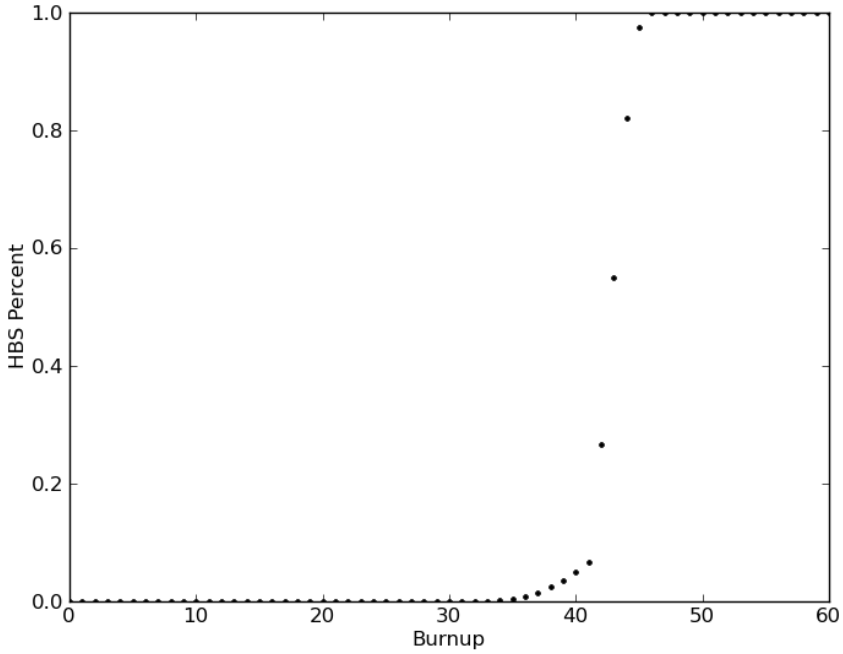

Figure 47: Simulation of U_3Si_2 fuel under irradiation with bubble growth. Note that HBS formation occurs at approximately 40 GWD/MTU. This corresponds roughly to an increase in porosity in experiment.

In order to examine accident tolerant fuels we run the simulation using U_3Si_2. The values of each of the parameters of the model used in this simulation are found in the second column of Table 14. Many of these values are approximate or assumptions based on limited experimental data. The results of the simulation at the same temperature as the previous UO_2 simulations is given in figure 47. From these results we see that HBS formation occurs between 35 and 45 GWD/MTU which is slightly lower than the point of fission gas release found in experiment[158]. Due to the cruder methods used for calculating the input parameters for U_3Si_2 these results seem reasonable , suggesting this model would work for other fuels.

5.4.2 Sensitivity Analysis

5.4.2.1 PRCC

In order to examine the effect of input parameters on the Potts model the PRCC between each input parameters and the local burnup at which lattice contraction began and the point at which 95% local burnup was reached were calculated. Each of the parameters were allowed to vary ±25% in their value at each burnup step and 100 trials were performed. The results of these calculations are contained in Table 15. Based on the results of these calculations it can be seen that each of the input parameters examined carries at least a moderately high importance. The dislocation density carries the least importance and this is probably due to the fact in UO_2 it is assumed to be constant after a local burnup of 44 GWD/MTU. In both models the lattice constant expansion behavior is deemed to be most important and is inversely correlated to the point at which the local burnup affects the output parameters. This result makes sense as we saw from examining the method for which the lattice constant expansion was calculated the way the value changed with the local burnup had a large impact on both the shape of the lattice expansion in the overall fuel and the HBS formation behavior. In looking at uranium silicide fuel this was also one of the parameters that required the most approximation therefore an in-depth study of the behavior of the lattice parameter in new fuels such as that performed by Spino *et al.* [182] on uranium dioxide would be beneficial for examining the HBS formation behavior of new fuels.

Table 15: The calculated PRCC values for the UO_2 grain growth and HBS formation Potts model. The gamma value is the importance of the input parameter with positive meaning a direct relationship and negative meaning an inverse relationship. The p value is a measure of the confidence of the value.

	Lattice Contraction	
Input Parameter	γ	p value
Site Area	-0.8243	5.9840×10^{-26}
Elastic Modulus	-0.8204	1.597×10^{-25}
Surface Energy	0.8480	9.041×10^{-29}
Lattice Expansion	-0.9442	4.592×10^{-49}
Dislocation Density	0.5305	1.373×10^{-08}
	95% Burnup Level	
Input Parameter	γ	p value
Site Area	-0.6699	2.494×10^{-14}
Elastic Modulus	-0.7104	1.263×10^{-16}
Surface Energy	0.6696	2.593×10^{-14}
Lattice Expansion	-0.8953	3.486×10^{-36}
Dislocation Density	0.2976	2.642×10^{-03}

5.5 Conclusions

In this section we have used kinetic Monte Carlo (kMC) simulations, within the SPPARKS framework, to examine the behavior of high burnup structure in uranium based fuels. The model examines the behavior of grain growth, recrystallization and bubble migration in a 2D grain structure meant to represent the rim region of a fuel pellet. Initially we examine UO_2 fuels with the goal of examining the behavior of the lattice parameter under irradiation. Three competing models for the swelling of the lattice parameter are studied based on previous experimental work [182]: fission damage due to an increase in simple defect concentration, increased dislocation loop density and size, and swelling due to excess vacancy concentrations. It is found that for this simulation fitting of the resulting behavior based on the formation of simple defects in the fuel from fission events produces lattice parameter behavior that is representative of the experimental results. The simulation is able to accurately predict an exponential growth in the lattice parameter up to a local burn up of 73 GWD/MTU followed by an sharp decrease in the lattice parameter as the formation of the HBS results in most of this damage being removed from the lattice.

The input parameters of the simulation are then adjusted to examine the behavior of U_3Si_2, a potential accident tolerant fuel for use in next generation reactors. Based on the results of this simulation we see that HBS formation occurs between 35 and 45 GWD/MTU which is slightly lower than the point of fission gas release found in experiment, suggesting this model would work for other fuels.

We performed sensitivity analysis on the UO_2 model while examining 5 of the input parameters. Based on the results of this study each of the 5 input parameters had at least a moderate importance on the local burnup at which lattice contraction began and when the grains were 95% HBS. However, the dislocation density was found to be least important for both outputs, which is likely caused by the fact it reaches a maximum value early in the evolution of the UO_2 structure. The lattice

parameter expansion was found to be the most important parameter for both outputs suggesting that in-depth analysis of the behavior of the lattice constant in potential fuel candidates would help to model the formation of HBS in the fuels.

CHAPTER VI

OTHER MODELS

6.1 Nano Porous Foams

6.1.1 Introduction

The use of nanoparticles in energy applications is of particular interest due to their large surface to volume ratios[108]. In particular nanofoams have characteristics far superior to those of dense metals, bulk metal foams, or ordinary nanoparticles. One method used for forming these nanofoams is through dealloying.

Dealloying is the selective dissolution of components in an alloy based on the eloctrochemical potentials of the constituent metals [118]. Upon dealloying select systems can exhibit nanoporous behavior. The formation of the nanoporrous metal is dependent on the relative electrochemical potentials on the different metal alloys[52]. In general the larger the difference the more likely that a nanoporous structure will form. In addition it is usually necessary for the dealloying metal components to be a dominant part of the system. In addition the structure in general should be homogenous with fast diffusion of the species that will be dealloyed.

Dealloying is an excellent problem to study using SPPARKS. The main components, the dissolution of a metal and diffusion, are already contained within the SPPARKS framework. Thus we have modified the SPPARKS diffusion application in order to create a model that simulates dealloying of a two system metal alloy in order to study the morphology of nanoporous foams.

6.1.2 Methodology

In general this model follows the diffusion application with the standard kMC algorithm in table 1 as described previously in this paper. The simulation contains two

metal types that are allowed to diffuse to empty lattice sites throughout the lattice structure. The rate of diffusion is given by[118]:

$$r_{diff} = \nu_1 e^{-\frac{nE_B}{k_B T}} \tag{50}$$

where n is the number of bonds, ν_1 is the prefactor constant assumed to be 10^{13}, which is the Debye frequency in most metals, and E_B is the binding energy.

In addition to the standard diffusion the model also allows one of the species to dissolve from a surface point. The act of dissolution is the inverse of the deposition mechanism already allowed as an option for diffusion simulations in the SPPARKS code. Thus it is modified to allow for the removal of atoms from the lattice with the following rate[118]:

$$r_{diss} = \nu_2 e^{-\frac{nE_B - \phi}{k_B T}} \tag{51}$$

where ν_2 is the rate of dissolution taken to be roughly 10 orders of magnitude smaller than that of diffusion and ϕ is the electrochemical potential.

6.1.3 Results

The model was tested with parameters similar to those used by Erlebacher [52] with $\nu_2 = 10^4$, $E_B = 0.15eV$, $T = 300K$, and $\phi = 0.98eV$. The results at times: 0, 100s, 1000s, and 10000s are shown in figure 48. Based on these results it can be seen that we have successfully replicated the results shown in Erlebacher [118]. We can see an initial roughening stage in short time intervals while the second metal is dealloyed from near the surface. A Wulf structure quickly forms after this until the dealloying metal begins to percolate to the surface resulting in nano pits being form in the surface.

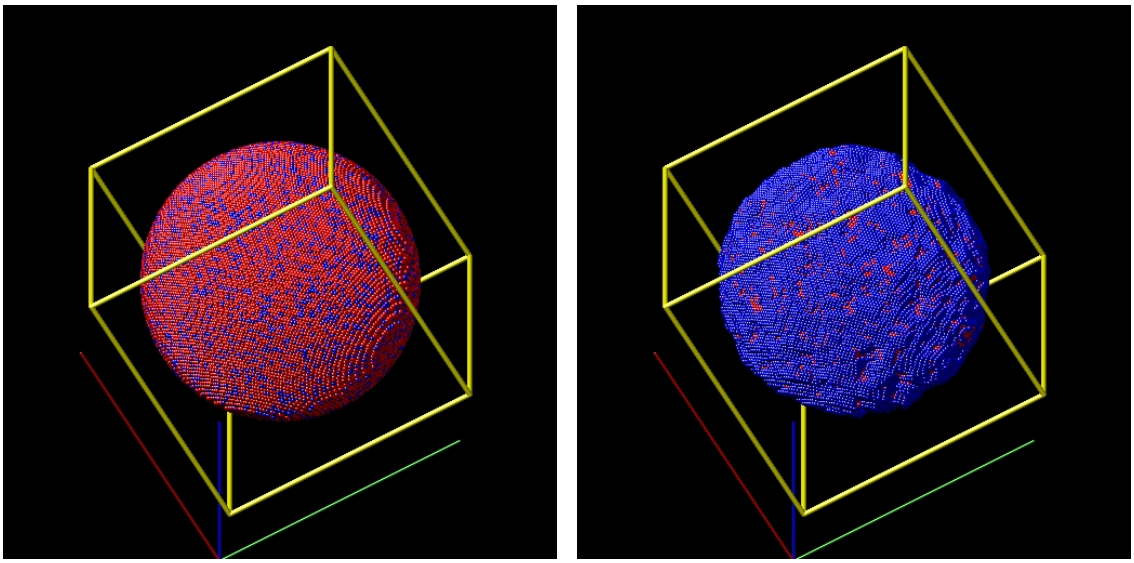

(a)

(b)

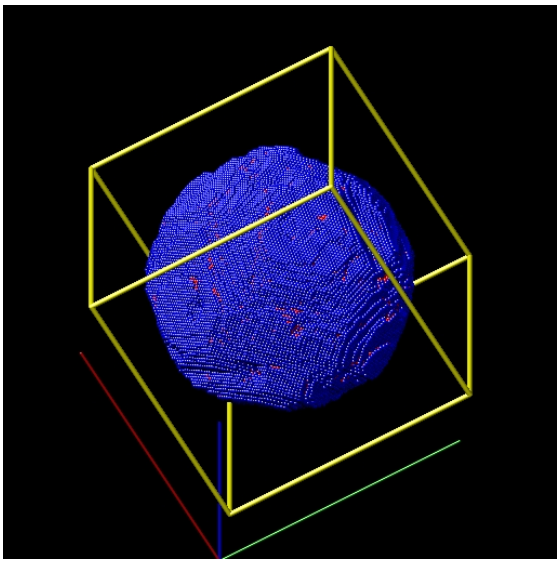

(c)

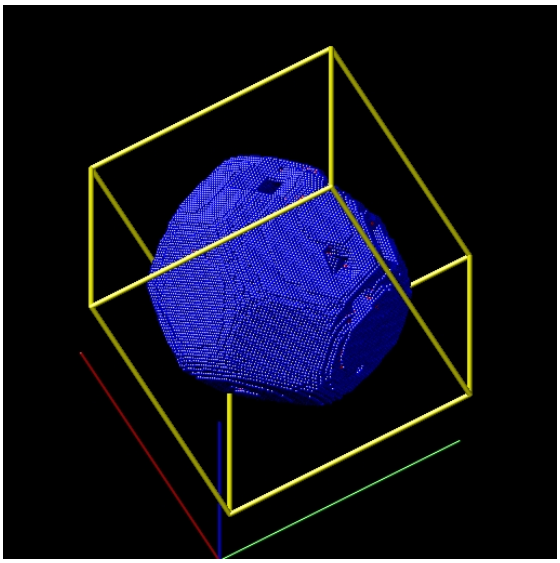

(d)

Figure 48: Evolution of the nanofoam dealloying model on a sphere of radius 30 lattice sites: (a) t = 0 the primary metal on the surface is the one that can dealloy due to its larger composition. (b) t = 100 The dealloying metal has been removed from the surface. (c) t = 1000 A wulf structure has begun to form. (d) t = 10000 Nano pits begin to form and expand as more of the dealloying metal is able to reach the surface.

6.1.4 Conclusions

We have successfully modified the SPPARKS diffusion application to examine the behavior of dealloying on nanostructures. We are able to replicate the results of

previous theoretical studies[52, 118]. However, there is evidence that the behavior described using pure dealloying is not found in the experimentally observed results of dealloying silicom from platinum to obtain a platinum nanofoam[108]. Based on this further work should be done on the model to attempt to replicate the results found in platinum. In particular it may be beneficial to examine the value of ϕ away from the surface of the metal and see if localized changes in this value would result in behavior that more closely matches experimental studies into the dealloying behavior of platinum.

6.2 Stochastic Cluster Dynamics

6.2.1 Introduction

In the field of nuclear materials the most common method for examining the effects of radiation damage on microstructure has been the use of cluster dynamics. However, with the increase in computational power in the past two decades there has been exploration of alternative methods that allow for more in depth examination of the microstructure. One of the most computationally intensive of these methods is kMC which examines the full geometric effects of the defects on the microstructure. This method can still be too computationally inefficient especially when dealing with the effects of large defect clusters. A relatively new method in the field of nuclear materials is the idea of stochastic cluster dynamics (SCD) which combines a stochastic algorithm similar to kMC with the statistical averaging methods of cluster dynamics[114].

Stochastic cluster dynamics provides the advantage of examining only the events that occur within the system at a given time avoiding the explosion of computational cost necessary for considering large scale defects required when using cluster dynamics. In general for each defect type considered in cluster dynamics a new ordinary differential equation must be added and solved for. Thus when considering large

clusters methods must be devised to account for the defect clusters without the need for an ever increasing number of equations. However, by eliminating the geometric constraints of the problems SCD provides the same benefit as cluster dynamics over KMC in that the amount of repeating high probability but low consequence events is no longer necessary and only events that affect the system in meaningful ways are performed.

The chemistry application, found in SPPARKS, allows for the simulation of events based on rates where any number of reactants can be turned into any number of products. This application is very similar in nature to the principles behind SCD thus we have modified it in order to be used for the application needed here.

6.2.2 Methodology

6.2.2.1 Stochastic Cluster Dynamics

In general the master equations for any of the three methods cluster dynamics, kMC, and SCD are the same for each species involved in the system:

$$\frac{dC_\mu}{dt} = K_0 + K_1 C_\mu C_\nu + S C_\mu \tag{52}$$

In converting these equations for use in SCD the only adjustment needed is to convert the concentrations to number densities by multiplying by the volume. These equations consist of four parts:

- 0^{th} order source terms: In general particles are introduced into the system through irradiation in the form of damage cascades. These events can be approximated through lower order simulations such as molecular dynamics or atomistic simulations. In this simulation defects were introduced exclusively as Frankel pairs. The rate of introduction of the defects must be in units of 1/s so in general must be converted from the more traditional dpa/s.

- 1^{st} order terms: The first order terms are the result of emission of defects from clusters. There is some disagreement as to the form of these terms in the literature. In particular there are different forms in papers by Marian *et al.* [114] and Barbu *et al.* [11]. However, several of the rate terms in the paper by Marian were ill defined so the form found in Barbu was used in this simulation:

$$\frac{4\pi}{\Omega} r_\mu^\nu D_\mu e^{\frac{-E_B}{k_B T}} \tag{53}$$

Where r_μ^ν is the capture radius of the defect in question and E_B is the binding energy given by:

$$E_B = \begin{cases} E_\mu^f + \frac{E_\nu^f - E_{2\nu}^B}{2^{2/3}-1}[(n+1)^{2/3} - n^{2/3}] & \mu \neq \nu \\ E_\mu^f + \frac{E_{2\nu}^B - E_\mu^f}{2^{2/3}-1}[(n+1)^{2/3} - n^{2/3}] & \mu = \nu \end{cases} \tag{54}$$

- 2^{nd} order terms: The second order terms are the result of combinations of defect species. In general these terms may be the result of one or two mobile species that may move in a range of different diffusion mechanisms. However, in our simulation the types of mobile defects were limited to the case of interstitials and vacancies moving in 3 dimensions. The form used as a result was:

$$\frac{4\pi}{V} r_\mu^\nu D_\mu \tag{55}$$

- Sink terms: The interaction of defects with irreducible sinks such as dislocations, grain boundaries and surfaces can in general be described as first order or second order terms. However, it is generally simpler to treat these effects as first order terms. In this case sinks were limited to effects due to surface terms with the assumption of a thin foil with no equilibrium dislocation density[29]:

$$\frac{(Z\rho_N)^{1/2}}{l}\left[coth(Z\rho_N)^{1/2}l - \frac{1}{(Z\rho_N)^{1/2}l}\right]^{-1} \quad (56)$$

Where ρ_N is the dislocation density of the metal, l is the thickness and Z is a bias factor.

6.2.2.2 SPPARKS

The general SPPARKS code provides a number of applications commonly used in kinetic Monte Carlo simulations. The majority of these applications are for on lattice simulations; however, there are options for off lattice and non lattice simulations. In particular for the formation of Stochastic Cluster Dynamics code there is a chemistry application that allows for the introduction of species and equations involving these species. In order to create the SCD application this general application was modified to better suit the exact purpose for which it was used.

The SPPARKS code in general uses the C++ programming language to create a series of classes that when used together build a specific application that is then used for the simulation. These classes can be loosely defined into three groups: overhead, solving, and application. There is some overlap in these groups and they each use information stored in other classes. However, in terms of modification requirements these groups generally will remain separated. For the case of SCD the application group was heavily modified and the other two groups were changed only in the way they interact with this group.

The first modification to the code was the introduction of C++ standard containers in place of C style arrays and strings. These containers have many advantages over the classic C counterparts including the fact that they include multiple types of containers that provide benefits for the SCD application. In particular the map container is a type similar to a hash table that is ordered so that it can be iterated over. This container was used to store the species and reaction information in order

to allow for faster access of the elements and to iterate over the list to build dependencies of the reactions. This has the potential to eliminate the high time cost of deleting elements from an array.

The use of the map allowed for the formation of data structures for the species and reactions in the simulation and keys that provided information on the species and reactions. In the previous chemistry application this information was stored in a series of arrays. The species data structure consists of the number of that type of defect in the simulation and the size of the defect. The reaction data structure was more complicated and consists of the reactions propensity, rate, and several vectors to store the reactants, products, and other reactions dependent on the selected reaction. The vector is another standard container and prior to the latest version of C++ was the container that most resembled the traditional C array. It has the advantages of internal memory management and a prebuilt size function.

One of the main components of an SCD simulation is the formation of larger and larger clusters of defects. In the traditional chemistry application this would be impossible to feasibly implement as each species and reaction need to be declared in the input file prior to the start of the simulation. Thus large scale changes needed to be made to the application in order to accommodate the creation of new species and their reactions as the simulation progressed. This was accomplished primarily by creating two new functions. The first was a method for introducing new reactions based on the size of a new species, the mobile species, and the species that are able to leave the new species. This task was aided by the use of a set structure to the strings to define each reaction and species as these strings contained the relevant information as to the species type and size of the new species or reaction. Thus they acted as building blocks for creating new reactions and species. This allowed for the formation of new species by the code during the simulation and the accompanying reactions to accompany each new species. Thus there is no longer an artificial limitation to the

number of species examined like needs to be imposed in traditional rate theory. The second was a method for generating the rates associated with each new reaction which was accomplished through a series of equations for the capture and emission events possible in the simulation. At the moment these equations are hard coded and need to be changed if the form or values are changed.

In the original chemistry application each reaction was stored in an array and given a number which indicated its order in the array. In order to accommodate the switch from arrays to maps for storage of the reactions a change was made in the way the chosen solver interacts with the application. In the original application the propensities, event to perform and time change were controlled by the solver and the information passed back and forth to the application as needed. With the use of the map reactions were stored as strings instead of numbers. Instead of modifying the solver to handle this change we instead limited the role of the solver to providing the time change and random number associated with the event choice to the application on demand. Now the propensity information is stored solely in the application and in the iteration function of the application the event to perform is chosen based on the random number returned by the solver.

6.2.3 Results

The SCD code was used to calculate the concentrations of defects and clusters in a thin iron film after 120 seconds of irradiation. The parameters used in the simulation are given in table 16 and the results are presented in figure 49. The results found were within an order of magnitude across a range of temperatures. Due to the fact that the concentrations of all vacancies and interstitials are nearly identical to the values found in other simulations this suggests that the issue is a discrepancy in the emission of defects from clusters or that the size is too small resulting in too few interstitials to properly interact with the vacancies.

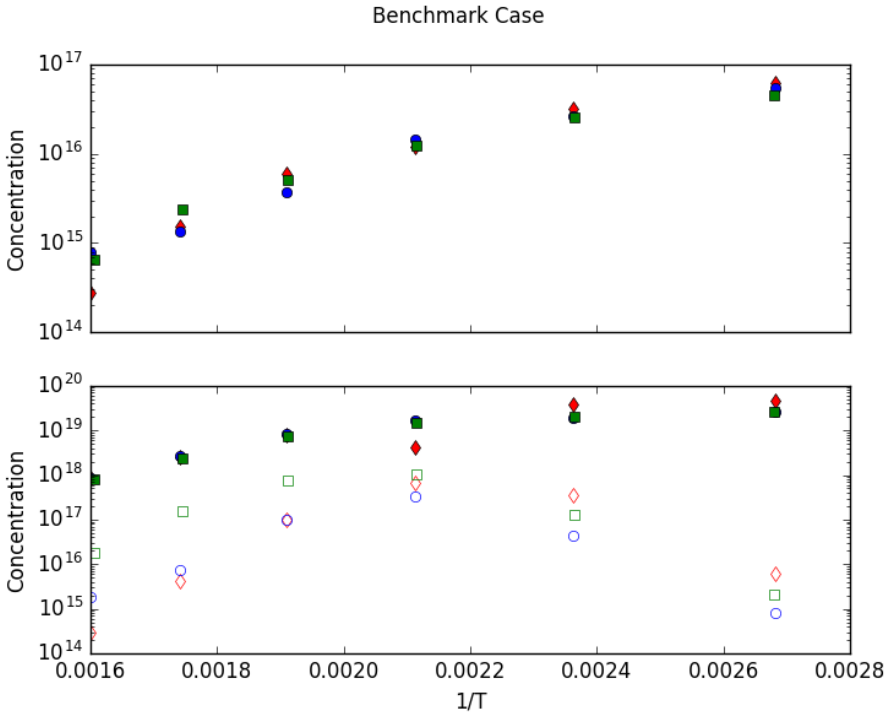

Figure 49: The results of the simulation are presented in green and the results of Marian et al (blue) and Barbu et al (red) are presented for comparison. The results for interstitials (top figure) and vacancies (solid bottom figure) seem to be in almost exact agreement. The results for voids (hollow bottom figure) seem to be high for high temperatures, the reason for this is unclear

6.2.4 Conclusions

The SCD code seems to be working properly based on the results achieved so far. The lack of consensus on the form of equations to be used suggests there is general disagreement or at least ambiguity as to the appropriate way to form the rates needed to perform SCD. In the future a sensitivity study can be performed on the parameters in the simulation in order to determine whether the discrepancy in the literature concerning the 1st order equations. In addition there is a need to optimize the code in its current form. The code has been setup to work specifically for the case examined in this paper. In addition there are methods that can be applied to increase the efficiency of the code.

Currently the code builds the number of species available based on whether the

Table 16: Input parameters for SCD model of defects in iron

Parameter	value
K_0	$1.5 \times 10^{-4} dpa/s$
l	$0.287 \mu m$
E_v^m	$1.3eV$
E_v^f	$1.6eV$
D_{v0}	$1cm^2/s$
E_i^m	$0.3eV$
E_i^f	$4.3eV$
D_{i0}	$4 \times 10^{-4} cm^2/s$
Z_v	1.0
Z_i	1.2
E_{2v}^B	$0.2eV$
E_{2i}^B	$0.9eV$
ρ_N	$1.5 \times 10^{15}/m^2$

species type has been used by the simulation up to that time. However, the code does not eliminate species that no longer have counts. Eliminating species as they are removed from the simulation may not be the most efficient method computationally for eliminating unused species, however, never eliminating them causes unnecessary memory storage. An algorithm can be created to maximize the efficiency of the code in terms of memory storage and computational efficiency. In the current form of the code the only available mobile species are interstitials and vacancies. In order to expand into more in depth and realistic simulations the use of more than two mobile species will be necessary. The final upgrade to the current code deals with the equations that determine the rates for different reactions. In the current form the values associated with the equations need to be hard coded in the C++ code. Based on research of C++ coding there is limitations to the extent these can be included in the input for an individual run but there is definitely room to eliminate the full hard coding currently required.

CHAPTER VII

CONCLUSIONS

Five kMC simulations have been developed within the SPPARKS framework for use with different applications related to nuclear and energy materials. The behavior of each of the models was examined and compared to relevant literature or other methods of modeling where available. The models are based on three of the built in simplistic models available in SPPARKS, diffusion, Potts, and chemistry, and required extensive modification of the original code.

Additionally sensitivity analysis was performed on three of the models in order to examine which of the input parameters are most important in the output of the simulation. Two types of sensitivity analysis were performed on the simulations. The first, MOAT examines changes in one parameter at a time while keeping the other parameters constant but performs this in an efficient manner that is known to approximate a global sensitivity analysis[197]. The second, PRCC uses LHS which is an efficient method of sampling the input parameter space in order to rank each of the input parameters based on the importance of the parameter in determining the resulting outcome variable[168].

The first of the models created examines the diffusion behavior of vacancies in a doped fluorite lattice. The goal of this study was to examine the behavior of the diffusivity and ionic conductivity as well as examine the behavior of vacancy-dopant pairs across a wide range of dopant atoms. A range of 3+ dopants (Ru, Lu, Yb, Er, Y, Gd, Eu, Sm, Nd, Pr, Ce, and La) which are found as fission products in UO_2 were examined in both a CeO_2 and UO_2 lattice structure. The input parameters were calculated in GULP using an interatomic potential fitted by the Grimes research

group based on the 6 nearest cation neighbors.

Based on our results we found that in ceria the largest ionic conductivity and diffusivity are found when the ceria is doped with samarium. In uranium dioxide, the largest diffusivity is found when cerium, praseodymium, or neodymium. In both cases the ratio of dopant ion to host ion is 1.12. In addition the clustering behavior of vacancies in uranium dioxide was examined. It was found that as the size of the dopant ion increased the vacancies were less likely to be found next to a dopant. This observation agrees with studies on the formation enthalpies of dopant vacancy clusters in UO_2 found in atomistic studies performed using DFT[177].

We performed sensitivity analysis on the 30 input parameters that constitute the different initial configurations. We discovered that MOAT was unable to produce meaningful results. However, our examination using PRCCs found that the non doped configuration is the most important configuration, that the majority of configurations were inversely related to the output variable, and that within each group of configurations with the same number of dopants there was no indication that any dopant location was consistently more important than any other positions suggesting that the 6 neighbors positions carry equal importance in determining the behavior of the system.

In the second model, the behavior of defects in bcc metals was examined. In particular we examined the effect of increasingly complex vacancy clusters on the resulting defect concentrations using both kMC simulations and rate equations. Initially vacancies were assumed not to form separate clusters but could only be annihilated by interstitials or generic sinks. Then it was assumed the vacancies the neighbored other vacancies were forming a void that could only be reversed if one of the vacancies was annihilated by a neighboring interstitial atom. Finally, vacancies were able to attach and detach from voids that were formed by vacancies moving to neighboring positions. It was assumed that the detachment rates were void-size independent and

dependent and the resulting concentrations of defects were compared.

The initial simple defect kMC model was compared to previously published results[166] and found to be satisfactory. However, when compared with rate equations the capture radius had to be adjust to get agreement between the two methods. The capture radius used was based on the definition published elsewhere and was therefore assumed to be appropriate. In the irreversible voids model the kMC results again agreed with available literature results with the exception of the capture radius.

The reversible voids models were compared with each other and with the irreversible voids model and it was found that there was little disagreement between the concentration of different defect concentrations as well as the size of the resulting vacancy clusters with the same initial conditions. Thus it is assumed that using the irreversible voids simulation is sufficient to model the behavior of voids in bcc metals.

Sensitivity analysis was performed using MOAT on both the rate equation and kMC models for the models involving only simple defects and simple defects with irreversible voids. While the results of each model varied there were some similarities between the models. In all cases the effect of the interstitial migration barrier on the concentration of interstitials was moderately to very important. In addition the sink density had a low importance in each of the models. Based on the results of MOAT analysis the rotational barrier was only highly important on any defect concentration in the irreversible voids model with kMC. Otherwise it was of moderate to little importance.

Additionally sensitivity analysis using PRCCs was performed on the simple defect model using rate equations as the MOAT analysis was unable to accurately separate the different input parameters' importance due to the small effect from the sink concentration. This analysis showed similar results to those of the MOAT analysis for the kMC model suggesting that the results from the MOAT when able to be performed correctly is an accurate measurement of the sensitivity of input parameters

in this model.

In the third simulation, a Potts model is developed to examine the evolution of gas bubbles and HBS formation in nuclear fuels. The model examines the behavior of the lattice constant under irradiation and the HBS formation over local burnups in the outer region of the fuel pellet consistent with use in a nuclear reactor. The model uses a 2D triangular lattice and would need to be modified to examine a more general lattice shape. Different methods for the proposed change in the lattice constant are examined with an $1 - e^x$ curve providing the best fit for the lattice constant behavior when compared to experiment. An attempt is made to fit the model to the behavior of uranium silicide as a potential accident tolerant fuel. It is found to cause HBS formation at a lower local burnup then experimental evidence would suggest. However, the experimental evidence is limited and therefore the input parameters are not as well known as in the case of UO_2.

We performed sensitivity analysis on the UO_2 model while examining 5 of the input parameters: lattice parameter expansion, site area, dislocation density, elastic modulus, and surface energy. Based on the results of this study each of the 5 input parameters had at least a moderate importance on the local burnup at which lattice contraction began and when the grains were 95% HBS. However, the dislocation density was found to be least important for both outputs, which is likely caused by the fact it reaches a maximum value early in the evolution of the UO_2 structure. The lattice parameter expansion was found to be the most important parameter for both outputs suggesting that in-depth analysis of the behavior of the lattice constant in potential fuel candidates would help to model the formation of HBS in the fuels.

The fourth model that has been developed examines the formation of nanoporous materials through a dealloying process. The model is a modification of the diffusion application in SPPARKS and uses an inverse deposition procedure for the dealloying. The model is able to replicate the results of other simulations. However, there is

evidence that for certain metal alloys the evolution of the dealloying metal is not consistent with these results. Further development of the model is necessary and may need to focus on the change in chemical potential due to the local environment.

The final model uses the chemistry application built into SPPARKS to create an SCD simulation. The application has been modified to allow for the creation of clusters of arbitrary size as they are formed in the course of the simulation. This is a major advantage over traditional cluster dynamics which requires the size of clusters to be truncated in order to create a set of equations to solve. The model has been applied to a similar problem as that of the second model. The model provides results which are consistent with those found in other models [114, 11]. Further development of the model should focus on improving the automation within the code and applying it to novel problems.

KMC models incorporate input parameters calculated from atomistic simulations and experiment and provide output that can then be applied to macroscopic simulations and higher level mesoscale simulations such as phase field modeling and crystal plasticity. The use of sensitivity analysis in this work has given a better understanding to the importance of the different energies that are used as input parameters in the various kMC models examined. This information can be used by other researchers to examine the uncertainty in these parameters and provide more refined values that will reduce the uncertainty when bridging scales. KMC modeling can be used as a comparison for phase field modeling across scales in which they are both applicable. In addition the output parameters from kMC simulations such as the concentration and diffusivity of defects and the size distribution and geometric behavior of clusters can be used by phase field models and crystal plasticity models to complete the bridge to a full multiscale modeling approach. The ability of the kMC simulation to provide information about the interaction and behavior of small scale material properties is of particular importance to enabling the evolution of macroscale models from qualitative

to quantitative results.

The use of SPPARKS to create a series of kMC applications that apply to nuclear and energy materials provides a method for bridging the simulation gap between atomistic and continuum models that is highly efficient and more easily incorporated by research groups. In addition the sensitivity analyses performed in this work provide a basis for understanding which input parameters are most important in order to reduce uncertainty in the model in the future by focusing research efforts on those parameters that would most reduce the uncertainty.

APPENDIX A

EXAMPLE INPUT FILES

A.1 Fluorite Diffusion

This model has two input files. One for the python script that runs the simulation and an input file for SPPARKS is generated for each run that is performed. This is an example of a working input file for the python script:

```
# Commented lines should have hash, slash, or parenthesis
#info # Comments at end of line should be ignored

# Run information
Steps 500000 # Specify number of steps or time for run
# Can have multiple step values for multiple output times

# Lattice dimension
15x15x15 #specify the lattice dimension in x,y,z

# Type of run Vacancy, Interstitial Fast,
# or Interstitial Full
Vacancy

# Include blocking options
#(either nonblock NONE, block NONE, or block barrier)
```

```
# Default is nonblock NONE
# block NONE means an infinite barrier
nonblock NONE

#Specify Output name
output CeSm

#Specify a temperature
Temp 673

#Percent  Dopant Run  Self Diff Run  Num of Runs
0.0035    Yes          Yes                10

# Here are the runs you can add as many as you like.
# The order doesn't matter
# The percent can be in terms of a percent or
# the number of vacancies
# Don't mix the two
# A Dopant Run is one with the dopant migration barriers
# A Self Diff Run is one where all migration barriers
# are the undoped configuration
# Number of runs will run multiple runs with different
# geometries and different seed numbers

# This file will run with the specified settings and
# produce 10runs that will store the full results into
```

```
# a directory called cesm and provide a file called
# difflength0.out that can be analyzed by a python script.
```

This is an example of the SPPARKS input file that is generated:

```
# This is a spparks input file for a doped fluorite lattice
# automatically created from a program by Richard Hoffman

seed            56789
# This is the seed for the random number generator

app_style       diffarg linear event nonblock NONE hop
# This is the app style
# Not the default nonblock NONE
# It is also an event based run time

dimension       3
# Dimensions of simulation

read_sites      read56789.diffapp
# a python created file with the site information

solve_style     linear
# Solve style
```

```
diag_style       energy
# Statistics output style

temperature      0.09246041
# Temperature in eV

dump     1 text 10000000000000000000 dump.0.3.56789.*.diffapp
id site i2 x y z i3 i4 i5
# Dump command note the frequency is a dummy

stats            10000000000000000000
# We don't want stats too often so dummy again

run 500000 upto
# Run time in steps. The upto allows multiple
# looks at different times

dump_one 1
# After it has run we produce a dump
```

In addition to a series of dumpfiles that provide the raw data on the results geometrical configurations of each simulation box, the python script produces a file containing the diffusivity and other relevant data on each of the runs. This data, for example, can be read by a python script to plot the values of the diffusivity across the calculated dopant concentrations in order to produce a plot similar to figure 10

A.2 Diffusion in bcc Metals

This model is run by calling the SPPARKS executable with the following input file with a command such as ./spk_serial<input_file and produces a series of dump files that can be read by a python script utilizing matplotlib to produce plots of the resulting defect concentrations similar to figure 23.

```
# SPPARKS Input for bcc Metal diffusion

seed                56789
#Seed for random number generator

app_style           diffdefecta 9.0 0.34 0.1 0.26 0.0001
# app information
# this is a run with simple defects only
# The first value is the production rate is seconds
# between pair production
# The second value is the vacancy barrier
# The third value is the interstitial barrier
# The fourth value is the rotational barrier
# The final value is the sink density

dimension           3
# Dimension of the simulation

lattice             bcc 1.0
# Informs the type of lattice is bcc with a=b=c=1.0
```

```
region            box block 0 100 0 100 0 100
# Creates the simulation space with x,y,z sizes

create_box        box
# Sets up the simulation box

create_sites      box
# Creates the sites in the region

set               site value 3 fraction 1
# Sets all values to occupied

solve_style       linearsim
# Sets the solve style

sector            no
# If using multiple processors this must be yes

diag_style        energy
# Diagnostic information for statistics

temperature       0.034469372
# Temperature of the simulation in eV

stats             100
```

```
# How often to print statistics on the run

dump              1 text 20 dump.diffvoid* id site i2 i3
# Sets up text dump files at a particular frequency,
# with a filename, and the information to provide
# The current dump gives the lattice site, particle type,
# direction(for interstitials), and cluster number

dump_modify 1 loglinfreq 20 10
# Change the dump frequency to log linear.
# This is vital for long runs

run 20000000
# The TIME to run
```

A.3 HBS Formation Potts Model

This model is run by calling the SPPARKS executable with the following input file with a command such as mpirun -np num_of_processors ./spk_linux<input_file and produces a series of dump files that can be read by a python script utilizing matplotlib to produce plots of the resulting burnup and lattice parameter like figure 40 or a plot of the grain structure at a particular burnup as in figure 41.

```
# SPPARKS Input file for 2D UO2 HBS formation simulation

seed              56789
#Seed for random number generator

app_style         pottsderive 100 2e13 1.7574e-7
# App information
# 100 is the number of spins
# The other two values are for fission rate and calculated
# burnup step time
# These are ignored in an rkMC simulation

dimension         2
#Number of dimensions

lattice           tri 1
#lattice type and normalized distance between sites
```

```
region            box block 0 1024 0 1024 0 1
# Create simulation size. In 2D simulation the z dimension
# must be 0 to 1.

create_box        box
# Creates simulation area

create_sites      box
# Creates the lattice sites

read_sites        output_cont2
# Read in the initial grain structure

sweep             raster
# Sweep style

sector            yes
# Allows for MPI runs

diag_style        energy
# Statistics to output

temperature       923
# Temperature. Modified to be in K.

stats             10
```

```
# Frequency to output statistics to the screen

dump            1 text 10 dump.pottsgood4.* id i1 i2 x y z
# Output text dumpfiles. i1 is the spin and i2 is whether
# it is bubble, HBS or grain

run             1250
# Time of run. Should be n times bu where n is the number
# of bubble steps per grain step
```

A.4 Nano Porous Foams

This model is run by calling the SPPARKS executable with the following input file with a command such as ./spk_serial<input_file and produces a series of dump image files that are similar to the images in figure 48.

```
# SPPARKS input file for Nano Porous Foams Models
# Refer to bcc metal model for explanation of
# redundant commands

seed              56753

app_style         diffalloy linear hop
# App command. Same as standard diffusion except app name.

dimension         3
lattice           fcc 1.0
boundary n n n
# Ensure non periodic boundaries for free surfaces

region            mysphere sphere 31 31 31 30
# Creates a sphere with a radius of 30

create_box        mysphere
create_sites      region mysphere
#set              site value 1 fraction 1
```

```
#set              site value 2 fraction 1.0
#set              site value 3 fraction 0.25
read_sites    input.txt
# Read in sites from text or input sites randomly

solve_style       linear
sector            no

diag_style        energy

temperature       0.17235

stats             0.01
dump  1 text 0.1 dump.*.diff3d
dump  2 image 0.01 dump3d.*.jpg site x sdiam 1.0 crange 0 3
view 150 30 axes yes 1 0.01 box yes 0.02
# An image file produced at the specified frequency

dump_modify       2 thresh site > 1 scolor 2*3 red/blue
# Modify the dump image to just show metals
# and specify colors

run               1.0
# Run time. Modify dumps if running for long times
```

A.5 SCD

This model is run by calling the SPPARKS executable with the following input file with a command such as ./spk_serial<input_file and produces a log file that includes the cluster types and amounts that can be read by a python script utilizing matplotlib to produce plots of the resulting defect concentrations similar to figure 49.

```
# SPPARKS input file for SCD application

seed            12345
# Seed for random number generator

app_style       scd
# App style is scd no other options needed

solve_style     linear
# Solve style

volume          2.3393656e-15
# Volume of box

temperature 623
# Temperature in K

add_species             1_v
add_species             1_i
```

```
add_species     Z
# Add initial species. In this cases vacancies,
# interstitials, and sinks
# Any species with equations are needed

add_reaction 1_i_v_c 1_i 1_v ?Eq3
add_reaction 1_v_i_c 1_v 1_i ?Eq4
add_reaction 1_v_v_c 1_v 1_v ?Eq1 2_v
add_reaction 1_i_i_c 1_i 1_i ?Eq2 2_i
add_reaction 5 +30000 1_i 1_v
# Reaction equations.
# The first value is the name. In order to allow for
# auto generation it must include the name of the
# reactants and what they are forming or number for
# production rates
# The next group of values is the reactants.
#Note: no reactants in the production equation.
# The next value is the rate for the reaction
# (+ is needed) or the equation number to generate
# the reaction rate (? is needed).
# Finally, the products if applicable are listed.
# More advanced reactions are generated by the code
# as they become needed.

count           1_i 0
count           1_v 0
```

```
count           Z 1000
# Initial counts


stats           10
# How often to print stats


run             120.0
# How long to run.
# Stats are saved in a file for later use.
```

REFERENCES

[1] Agro, K. E., Bradley, C. A., Mittmann, N., Iskedjian, M., Ilersich, A. L., and Einarson, T. R., "Sensitivity analysis in health economic and pharmacoeconomic studies," *PharmacoEconomics*, vol. 11, no. 1, pp. 75–88, 1997.

[2] Aizenshtein, M., Shvareva, T. Y., and Navrotsky, A., "Thermochemistry of lanthana- and yttria-doped thoria," *Journal of the American Ceramic Society*, vol. 93, no. 12, pp. 4142–4147, 2010.

[3] Alexandrov, V., Grønbech-Jensen, N., Navrotsky, A., and Asta, M., "First-principles computational study of defect clustering in solid solutions of tho_2 with trivalent oxides," *Phys. Rev. B*, vol. 82, p. 174115, Nov 2010.

[4] Anderson, M., Srolovitz, D., Grest, G., and Sahni, P., "Computer simulation of grain growthi. kinetics," *Acta metallurgica*, vol. 32, no. 5, pp. 783–791, 1984.

[5] Andersson, D. A., Simak, S. I., Skorodumova, N. V., Abrikosov, I. A., and Johansson, B., "Optimization of ionic conductivity in doped ceria," *Proceedings of the National Academy of Sciences of the United States of America*, vol. 103, no. 10, pp. 3518–3521, 2006.

[6] Arampatzis, G. and Katsoulakis, M. A., "Goal-oriented sensitivity analysis for lattice kinetic monte carlo simulations," *The Journal of Chemical Physics*, vol. 140, no. 12, 2014.

[7] Balasz, G. B. and Glass, R. S., "ac impedance studies of rare earth oxide doped ceria," *Solid State Ionics*, vol. 76, no. 12, pp. 155–162, 1995.

[8] Baniotopoulos, C., "A contribution to the sensitivity analysis of the sea-bed-structure interaction problem for underwater pipelines," *Computers & Structures*, vol. 40, no. 6, pp. 1421 – 1427, 1991.

[9] Barashev, A. and Bacon, D., "Monte carlo investigation of cascade damage effects in metals under low temperature irradiation," vol. 540, pp. 709–714, 1999. cited By 0.

[10] Barashev, A., Bacon, D., and Golubov, S., "Monte carlo modelling of damage accumulation in metals under cascade irradiation," *Journal of Nuclear Materials*, vol. 276, no. 1, pp. 243–250, 2000. cited By 8.

[11] Barbu*, A., Becquart, C., Bocquet, J., Dalla Torre, J., and Domain, C., "Comparison between three complementary approaches to simulate largefluence irradiation: application to electron irradiation of thin foils," *Philosophical Magazine*, vol. 85, no. 4-7, pp. 541–547, 2005.

[12] Barner, J., Cunningham, M., Freshley, M., and Lanning, D., "High burnup effects program: Final report," *HBEP-61*, 1990.

[13] Barney, W. and Wemple, B., *Metallography of Irradiated UO2-Containing Fuel Elements*. Knolls Atomic Power Laboratory, General Electric Company, 1958.

[14] Baron, D., "Porosity buildup in the fuel periphery at high burnup," in *HBEP Steering Committee Meeting, Wengen, Switzerland*, 1986.

[15] Baron, D., Hermitte, B., and Piron, J., "An attempt to simulate the porosity buildup in the rim at high burnup," tech. rep., 1998.

[16] Battaile, C. C., Srolovitz, D. J., and Butler, J. E., "A kinetic monte carlo method for the atomic-scale simulation of chemical vapor deposition: Application to diamond," *Journal of Applied Physics*, vol. 82, no. 12, pp. 6293–6300, 1997.

[17] Beck, M. B., Ravetz, J. R., Mulkey, L. A., and Barnwell, T. O., "On the problem of model validation for predictive exposure assessments," *Stochastic Hydrology and Hydraulics*, vol. 11, no. 3, pp. 229–254, 1997.

[18] Beck, P. A., Kremer, J. C., Demer, L., and Holzworth, M., "Grain growth in high-purity aluminum and in an aluminum-magnesium alloy," *Trans. Am. Inst. Min. Metall. Eng*, vol. 175, pp. 372–400, 1948.

[19] Becquart, C. and Domain, C., "Ab initio calculations about intrinsic point defects and he in w," *Nuclear Instruments and Methods in Physics Research Section B: Beam Interactions with Materials and Atoms*, vol. 255, no. 1, pp. 23–26, 2007.

[20] Becquart, C., Domain, C., Malerba, L., and Hou, M., "The influence of the internal displacement cascades structure on the growth of point defect clusters in radiation environment," *Nuclear Instruments and Methods in Physics Research, Section B: Beam Interactions with Materials and Atoms*, vol. 228, no. 1-4 SPEC. ISS., pp. 181–186, 2005. cited By 8.

[21] Behera, R. K., Watanabe, T., Andersson, D. A., Uberuaga, B. P., and Deo, C. S., "Diffusion of oxygen interstitials in uo2+x using kinetic monte carlo simulations: Role of o/m ratio and sensitivity analysis," *Journal of Nuclear Materials*, vol. 472, pp. 89 – 98, 2016.

[22] Belle, J., *Uranium dioxide: properties and nuclear applications*, vol. 7. Naval Reactors, Division of Reactor Development, US Atomic Energy Commission, 1961.

[23] Binks, D. J., *Ph.D. Thesis*. PhD thesis, University of Surrey, 1994.

[24] Bleiberg, M., Berman, R., and Lustman, B., "Effects of high burn-up on oxide ceramic fuels," in *Radiation Damage in Reactor Materials. Part of the Proceedings of the Symposium on Radiation Damage in Solids and Reactor Materials*, 1963.

[25] Bogicevic, A. and Wolverton, C., "Nature and strength of defect interactions in cubic stabilized zirconia," *Phys. Rev. B*, vol. 67, p. 024106, Jan 2003.

[26] Bogicevic, A., Wolverton, C., Crosbie, G. M., and Stechel, E. B., "Defect ordering in aliovalently doped cubic zirconia from first principles," *Phys. Rev. B*, vol. 64, p. 014106, Jun 2001.

[27] Bortz, A., Kalos, M., and Lebowitz, J., "A new algorithm for monte carlo simulation of ising spin systems," *Journal of Computational Physics*, vol. 17, no. 1, pp. 10–18, 1975. cited By 1295.

[28] Brailsford, A. and Bullough, R., "The rate theory of swelling due to void growth in irradiated metals," *Journal of Nuclear Materials*, vol. 44, no. 2, pp. 121–135, 1972.

[29] Bullough, R., Hayns, M., and Wood, M., "Sink strengths for thin film surfaces and grain boundaries," *Journal of Nuclear Materials*, vol. 90, no. 1-3, pp. 44–59, 1980.

[30] Busker, G., Chroneos, A., Grimes, R. W., and Chen, I.-W., "Solution mechanisms for dopant oxides in yttria," *Journal of the American Ceramic Society*, vol. 82, no. 6, pp. 1553–1559, 1999.

[31] Busker, G., Grimes, R. W., and Bradford, M. R., "The solution and diffusion of ruthenium in uo2x," *Journal of Nuclear Materials*, vol. 312, no. 23, pp. 156 – 162, 2003.

[32] Cai, W., Bulatov, V. V., Justo, J. F., Argon, A. S., and Yip, S., "Kinetic monte carlo approach to modeling dislocation mobility," *Computational materials science*, vol. 23, no. 1, pp. 124–130, 2002.

[33] Cai, W., Bulatov, V. V., Yip, S., and Argon, A. S., "Kinetic monte carlo modeling of dislocation motion in bcc metals," *Materials Science and Engineering: A*, vol. 309, pp. 270–273, 2001.

[34] Catlow, C. R. A., "Fission gas diffusion in uranium dioxide," *Proceedings of the Royal Society of London. A. Mathematical and Physical Sciences*, vol. 364, no. 1719, pp. 473–497, 1978.

[35] Caturla, M., Soneda, N., Diaz de la Rubia, T., and Fluss, M., "Kinetic monte carlo simulations applied to irradiated materials: The effect of cascade damage in defect nucleation and growth," *Journal of Nuclear Materials*, vol. 351, no. 1-3, pp. 78–87, 2006. cited By 24.

[36] Chamati, H., Papanicolaou, N., Mishin, Y., and Papaconstantopoulos, D., "Embedded-atom potential for fe and its application to self-diffusion on fe (100)," *Surface Science*, vol. 600, no. 9, pp. 1793–1803, 2006.

[37] Chen, L.-Q. and Yang, W., "Computer simulation of the domain dynamics of a quenched system with a large number of nonconserved order parameters: The grain-growth kinetics," *Phys. Rev. B*, vol. 50, pp. 15752–15756, Dec 1994.

[38] Chen, W. and Navrotsky, A., "Thermochemical study of trivalent-doped ceria systems: Ceo2mo1.5 (m = la, gd, and y)," *Journal of Materials Research*, vol. 21, pp. 3242–3251, 2006.

[39] CHENG, T., "EPQ WITH PROCESS CAPABILITY AND QUALITY ASSURANCE CONSIDERATIONS," *JOURNAL OF THE OPERATIONAL RESEARCH SOCIETY*, vol. 42, pp. 713–720, AUG 1991.

[40] Christopher Frey, H. and Patil, S. R., "Identification and review of sensitivity analysis methods," *Risk analysis*, vol. 22, no. 3, pp. 553–578, 2002.

[41] Cleave, A. R., *Atomic scale simulations for waste form applications*. PhD thesis, Department of Materials, Imperial College, London, 2006.

[42] Cleave, A., *, R. W. G., and Sickafus, K., "Plutonium and uranium accommodation in pyrochlore oxides," *Philosophical Magazine*, vol. 85, no. 9, pp. 967–980, 2005.

[43] Cullen, A. C. and Frey, H. C., *Probabilistic techniques in exposure assessment: a handbook for dealing with variability and uncertainty in models and inputs*. Springer Science & Business Media, 1999.

[44] Deo, C. S., Okuniewski, M. A., Srivilliputhur, S. G., Maloy, S. A., Baskes, M. I., James, M. R., and Stubbins, J. F., "Helium bubble nucleation in bcc iron studied by kinetic monte carlo simulations," *Journal of Nuclear Materials*, vol. 361, no. 23, pp. 141 – 148, 2007. {TMS} 2007:Wechsler SymposiumProceedings of the Symposium on Radiation Effects, Deformation and Phase Transformations in Metals and Ceramics, organized in honor of Prof. Monroe S. Wechsler.

[45] Dholabhai, P. P. and Adams, J. B., "A blend of first-principles and kinetic lattice monte carlo computation to optimize samarium-doped ceria," *Journal of Materials Science*, vol. 47, no. 21, pp. 7530–7541, 2012.

[46] Dholabhai, P. P., Adams, J. B., Crozier, P. A., and Sharma, R., "In search of enhanced electrolyte materials: a case study of doubly doped ceria," *Journal of Materials Chemistry*, vol. 21, no. 47, pp. 18991–18997, 2011.

[47] Dholabhai, P. P., Shahriar, A., James, B. A., Peter, A. C., and Renu, S., "Predicting the optimal dopant concentration in gadolinium doped ceria: a kinetic lattice monte carlo approach," *Modelling and Simulation in Materials Science and Engineering*, vol. 20, no. 1, p. 015004, 2012.

[48] Domain, C., Becquart, C., and Malerba, L., "Simulation of radiation damage in fe alloys: An object kinetic monte carlo approach," *Journal of Nuclear Materials*, vol. 335, no. 1, pp. 121–145, 2004. cited By 142.

[49] Du, Y. A., Rogal, J., and Drautz, R., "Diffusion of hydrogen within idealized grains of bcc fe: a kinetic monte carlo study," *Physical Review B*, vol. 86, no. 17, p. 174110, 2012.

[50] Dunn, A., Dingreville, R., and Capolungo, L., "Multi-scale simulation of radiation damage accumulation and subsequent hardening in neutron-irradiated -fe," *Modelling and Simulation in Materials Science and Engineering*, vol. 24, no. 1, p. 015005, 2016.

[51] Eguchi, K., Setoguchi, T., Inoue, T., and Arai, H., "Electrical properties of ceria-based oxides and their application to solid oxide fuel cells," *Solid State Ionics*, vol. 52, no. 13, pp. 165–172, 1992.

[52] Erlebacher, J., "An atomistic description of dealloying porosity evolution, the critical potential, and rate-limiting behavior," *Journal of the Electrochemical Society*, vol. 151, no. 10, pp. C614–C626, 2004.

[53] Fraedrich, D. and Goldberg, A., "A methodological framework for the validation of predictive simulations," *European Journal of Operational Research*, vol. 124, no. 1, pp. 55 – 62, 2000.

[54] Frost, B. R. T., "Nuclear fuels," *R. Inst. Chem., Rev.*, vol. 2, pp. 163–205, 1969.

[55] Fu, C.-C., Willaime, F., and Ordejón, P., "Stability and mobility of mono-and di-interstitials in α-fe," *Physical review letters*, vol. 92, no. 17, p. 175503, 2004.

[56] Gale, J. D. and Rohl, A. L., "The general utility lattice program (gulp)," *Molecular Simulation*, vol. 29, no. 5, pp. 291–341, 2003.

[57] Gao, F., Bacon, D., Barashev, A., and Heinisch, H., "Kinetic monte carlo annealing simulation of damage produced by cascades in alpha-iron," vol. 540, pp. 703–708, 1999. cited By 3.

[58] Garner, F., Toloczko, M., and Sencer, B., "Comparison of swelling and irradiation creep behavior of fcc-austenitic and bcc-ferritic/martensitic alloys at high neutron exposure," *Journal of Nuclear Materials*, vol. 276, no. 13, pp. 123 – 142, 2000.

[59] Gillespie, D. T., "Exact stochastic simulation of coupled chemical reactions," *The Journal of Physical Chemistry*, vol. 81, no. 25, pp. 2340–2361, 1977.

[60] Govers, K., Lemehov, S., Hou, M., and Verwerft, M., "Comparison of interatomic potentials for uo2. part i: Static calculations," *Journal of Nuclear Materials*, vol. 366, no. 12, pp. 161 – 177, 2007.

[61] Grest, G. S., Anderson, M. P., and Srolovitz, D. J., "Domain-growth kinetics for the q-state potts model in two and three dimensions," *Phys. Rev. B*, vol. 38, pp. 4752–4760, Sep 1988.

[62] Grieshammer, S., Grope, B. O. H., Koettgen, J., and Martin, M., "A combined dft + u and monte carlo study on rare earth doped ceria," *Physical Chemistry Chemical Physics*, vol. 16, no. 21, pp. 9974–9986, 2014.

[63] Grimes, R. W., "Solution of mgo, cao, and tio2 in -ai2o3," *Journal of the American Ceramic Society*, vol. 77, no. 2, pp. 378–384, 1994.

[64] Grimes, R. W., Binks, D. J., and Lidiard, A. B., "The extent of zinc oxide solution in zinc chromate spinel," *Philosophical Magazine A*, vol. 72, no. 3, pp. 651–668, 1995.

[65] Grimes, R. W., Busker, G., McCoy, M. A., Chroneos, A., Kilner, J. A., and Chen, S.-P., "The effect of ion size on solution mechanism and defect cluster geometry," *Berichte der Bunsengesellschaft fur physikalische Chemie*, vol. 101, no. 9, pp. 1204–1210, 1997.

[66] Grimes, R. W., Konings, R. J., and Edwards, L., "Greater tolerance for nuclear materials.," *Nature materials*, vol. 7, no. 9, 2008.

[67] Grimes, R. and Chen, S., "The influence of ion size on the binding of a charge compensating cobalt vacancy to m3+ dopant ions in coo," *Journal of Physics and Chemistry of Solids*, vol. 61, no. 8, pp. 1263 – 1268, 2000.

[68] Grope, B. O. H., Zacherle, T., Nakayama, M., and Martin, M., "Oxygen ion conductivity of doped ceria: A kinetic monte carlo study," *Solid State Ionics*, vol. 225, no. 0, pp. 476–483, 2012.

[69] Guo, X., Zhang, X., Xue, J., and Li, W., "Kmc simulation of helium bubble formation in alpha-fe," *Nuclear Instruments and Methods in Physics Research Section B: Beam Interactions with Materials and Atoms*, vol. 307, pp. 77–80, 2013.

[70] Hall, R., Mortimer, M., and Mortimer, D., "Surface energy measurements on uo2a critical review," *Journal of Nuclear Materials*, vol. 148, no. 3, pp. 237–256, 1987.

[71] Hamby, D., "A review of techniques for parameter sensitivity analysis of environmental models," *Environmental monitoring and assessment*, vol. 32, no. 2, pp. 135–154, 1994.

[72] Heinisch, H. and Singh, B., "Kinetic monte carlo simulations of void lattice formation during irradiation," *Philosophical Magazine*, vol. 83, no. 31-34, pp. 3661–3676, 2003. cited By 31.

[73] Heinisch, H., Singh, B., and Golubov, S., "Kinetic monte carlo studies of the effects of burgers vector changes on the reaction kinetics of one-dimensionally gliding interstitial clusters," *Journal of Nuclear Materials*, vol. 276, no. 1, pp. 59–64, 2000. cited By 23.

[74] Heinisch, H. L., Trinkaus, H., and Singh, B. N., "Kinetic monte carlo studies of the reaction kinetics of crystal defects that diffuse one-dimensionally with occasional transverse migration," *Journal of Nuclear Materials*, vol. 367, pp. 332–337, 2007.

[75] Helton, J. C., "Uncertainty and sensitivity analysis techniques for use in performance assessment for radioactive waste disposal," *Reliability Engineering & System Safety*, vol. 42, no. 2, pp. 327 – 367, 1993.

[76] Helton, J. C. and Breeding, R. J., "Calculation of reactor accident safety goals," *Reliability Engineering & System Safety*, vol. 39, no. 2, pp. 129 – 158, 1993.

[77] Hoffman, F. O. and Miller, C. W., "Uncertainties in environmental radiological assessment models and their implications," in *Proceedings of the Nineteenth Annual Meeting of the National Council on Radiation Protection and Measurements*, pp. 6–7, 1983.

[78] Holm, E., Miodownik, M., and Rollett, A., "On abnormal subgrain growth and the origin of recrystallization nuclei," *Acta Materialia*, vol. 51, no. 9, pp. 2701 – 2716, 2003.

[79] Holm, E. A. and Battaile, C. C., "The computer simulation of microstructural evolution," *Jom*, vol. 53, no. 9, pp. 20–23, 2001.

[80] Holm, E. A., Glazier, J. A., Srolovitz, D. J., and Grest, G. S., "Effects of lattice anisotropy and temperature on domain growth in the two-dimensional potts model," *Phys. Rev. A*, vol. 43, pp. 2662–2668, Mar 1991.

[81] Huang, S., Worthington, D. L., Asta, M., Ozolins, V., Ghosh, G., and Liaw, P. K., "Calculation of impurity diffusivities in α-fe using first-principles methods," *Acta Materialia*, vol. 58, no. 6, pp. 1982–1993, 2010.

[82] Iman, R. L., Helton, J. C., and Campbell, J. E., "An approach to sensitivity analysis of computer models: Part iiranking of input variables, response surface validation, distribution effect and technique synopsis," *Journal of Quality Technology*, vol. 13, no. 4, pp. 232–240, 1981.

[83] Inaba, H. and Tagawa, H., "Ceria-based solid electrolytes," *Solid State Ionics*, vol. 83, no. 12, pp. 1 – 16, 1996.

[84] Ivasishin, O., Shevchenko, S., Vasiliev, N., and Semiatin, S., "A 3-d monte-carlo (potts) model for recrystallization and grain growth in polycrystalline materials," *Materials Science and Engineering: A*, vol. 433, no. 12, pp. 216 – 232, 2006.

[85] Jiang, J., Shen, W., and Hertz, J. L., "Structure and ionic conductivity of nanoscale gadolinia-doped ceria thin films," *Solid State Ionics*, vol. 249250, no. 0, pp. 139–143, 2013.

[86] Johnson, R., "Interstitials and vacancies in α iron," *Physical Review*, vol. 134, no. 5A, p. A1329, 1964.

[87] Ju, J., Chen, F., and Xia, C., "Ionic conductivity of impregnated samaria doped ceria for solid oxide fuel cells," *Electrochimica Acta*, vol. 136, pp. 422 – 429, 2014.

[88] Kaxiras, E. and Erlebacher, J., "Adatom diffusion by orchestrated exchange on semiconductor surfaces," *Phys. Rev. Lett.*, vol. 72, pp. 1714–1717, Mar 1994.

[89] Kewley, R. H., Embrechts, M. J., and Breneman, C., "Data strip mining for the virtual design of pharmaceuticals with neural networks," *IEEE Transactions on Neural Networks*, vol. 11, pp. 668–679, May 2000.

[90] Khakpour, Z., Yuzbashi, A., Maghsodipour, A., and Ahmadi, K., "Electrical conductivity of sm-doped ceo2 electrolyte produced by two-step sintering," *Solid State Ionics*, vol. 227, no. 0, pp. 80–85, 2012.

[91] Killeen, J. C., "Fission gas release and swelling in uo2 doped with cr2o3," *Journal of Nuclear Materials*, vol. 88, no. 23, pp. 177–184, 1980.

[92] Kinoshita, M., "Towards the mathematical model of rim structure formation," *Journal of nuclear materials*, vol. 248, pp. 185–190, 1997.

[93] Kinoshita, M., "High burnup rim project:(iii) properties of rim-structured fuel," in *Proceedings of ANS International Meeting on LWR Fuel Performance, Florida, September 19-22, 2004*, 2004.

[94] Kinoshita, M., Sonoda, T., Kitajima, S., Sasahara, A., Kolstad, E., Matzke, H., Rondinella, V., Stalios, A., Walker, C., Ray, I., and

OTHERS, "High burn-up rim project (ii) irradiation and examination to investigate rim-structured fuel," in *Proc. Int. Conf. on LWR Fuel Perfomance, Amer. Nucl. Soc., Park City*, pp. 590–603, 2000.

[95] KINOSHITA, M., CHEN, Y., KANETA, Y., GENG, H. Y., IWASAWA, M., OHNUMA, T., ICHINOMIYA, T., NISHIURA, Y., ITAKURA, M., NAKAMURA, J., and OTHERS, "Study of fission and high-burnup induced restructuring of nuclear fuel ceramics-applying computer science to investigate kinetic process," in *MRS Proceedings*, vol. 1043, pp. 1043–T12, Cambridge Univ Press, 2007.

[96] KLEIJNEN, J. P., "Verification and validation of simulation models," *European Journal of Operational Research*, vol. 82, no. 1, pp. 145 – 162, 1995.

[97] KLEIJNEN, J. P. and SARGENT, R. G., "A methodology for fitting and validating metamodels in simulation1," *European Journal of Operational Research*, vol. 120, no. 1, pp. 14 – 29, 2000.

[98] KOFSTAD, P., *Nonstoichiometry, diffusion, and electrical conductivity in binary metal oxides*. Wiley series on the science and technology of materials, Wiley-Interscience, 1972.

[99] KOIZUMI, S., UMEHARA, H., and WAKASHIMA, Y., "Study on fission gas release from high burnup fuel," tech. rep., 1991.

[100] KRISHNAMURTHY, R., YOON, Y. G., SROLOVITZ, D. J., and CAR, R., "Oxygen diffusion in yttria-stabilized zirconia: A new simulation model," *Journal of the American Ceramic Society*, vol. 87, no. 10, pp. 1821–1830, 2004.

[101] LAM, N. Q., ROTHMAN, S. J., and SIZMANNS, R., "Steady-state point-defect diffusion profiles in solids during irradiation," *Radiation Effects*, vol. 23, no. 1, pp. 53–59, 1974.

[102] LASSMANN, K., WALKER, C., VAN DE LAAR, J., and LINDSTRÖM, F., "Modelling the high burnup uo 2 structure in lwr fuel," *Journal of Nuclear Materials*, vol. 226, no. 1, pp. 1–8, 1995.

[103] LEE, B.-J., BASKES, M., KIM, H., and CHO, Y. K., "Second nearest-neighbor modified embedded atom method potentials for bcc transition metals," *Physical Review B*, vol. 64, no. 18, p. 184102, 2001.

[104] LEE, T. A., NAVROTSKY, A., and MOLODETSKY, I., "Enthalpy of formation of cubic yttria-stabilized zirconia," *Journal of Materials Research*, vol. 18, pp. 908–918, 2003.

[105] LEE, T. A. and NAVROTSKY, A., "Enthalpy of formation of cubic yttria-stabilized hafnia," *Journal of Materials Research*, vol. 19, pp. 1855–1861, 2004.

[106] Lee, T., Baskes, M. I., Valone, S. M., and Doll, J., "Atomistic modeling of thermodynamic equilibrium and polymorphism of iron," *Journal of Physics: Condensed Matter*, vol. 24, no. 22, p. 225404, 2012.

[107] Leenaers, A., de Tollenaere, L., Delafoy, C., and Van den Berghe, S., "On the solubility of chromium sesquioxide in uranium dioxide fuel," *Journal of Nuclear Materials*, vol. 317, no. 1, pp. 62–68, 2003.

[108] Li, Y. and Antoniou, A., "Synthesis of transversely isotropic nanoporous platinum," *Scripta Materialia*, vol. 66, no. 8, pp. 503–506, 2012.

[109] Li, Z.-P., Mori, T., Zou, J., and Drennan, J., "Defects clustering and ordering in di- and trivalently doped ceria," *Materials Research Bulletin*, vol. 48, no. 2, pp. 807–812, 2013.

[110] Limat, S., Woronoff-Lemsi, M., Deconinck, E., Racadot, E., Jacquet, M., Herve, P., and Cahn, J., "Cost-effectiveness of cd 34+ dose in peripheral blood progenitor cell transplantation for non-hodgkins lymphoma patients: a single centre study," *Bone marrow transplantation*, vol. 25, no. 9, pp. 997–1002, 2000.

[111] M. D. McKay, R. J. Beckman, W. J. C., "A comparison of three methods for selecting values of input variables in the analysis of output from a computer code," *Technometrics*, vol. 21, no. 2, pp. 239–245, 1979.

[112] Manheim, L. M., "Health services research clinical trials: Issues in the evaluation of economic costs and benefits," *Controlled Clinical Trials*, vol. 19, no. 2, pp. 149 – 158, 1998.

[113] Manzel, R. and Walker, C., "{EPMA} and {SEM} of fuel samples from {PWR} rods with an average burn-up of around 100 mwd/kghm," *Journal of Nuclear Materials*, vol. 301, no. 23, pp. 170 – 182, 2002.

[114] Marian, J. and Bulatov, V. V., "Stochastic cluster dynamics method for simulations of multispecies irradiation damage accumulation," *Journal of Nuclear Materials*, vol. 415, no. 1, pp. 84–95, 2011.

[115] Matsui, T. and Naito, K., "Electrical conductivity measurement and thermogravimetric study of pure and niobium-doped uranium dioxide," *Journal of Nuclear Materials*, vol. 136, no. 1, pp. 59–68, 1985.

[116] Mccoy, M. A., Grimes, R. W., and Lee, W. E., "Phase stability and interfacial structures in the srosrtio3 system," *Philosophical Magazine A*, vol. 75, no. 3, pp. 833–846, 1997.

[117] McCoy, M. A., Grimes, R. W., and Lee, W. E., "Planar intergrowth structures in the zno-in2o3 system," *Philosophical Magazine A*, vol. 76, no. 6, pp. 1187–1201, 1997.

[118] McCue, I., Snyder, J., Li, X., Chen, Q., Sieradzki, K., and Erlebacher, J., "Apparent inverse gibbs-thomson effect in dealloyed nanoporous nanoparticles," *Physical review letters*, vol. 108, no. 22, p. 225503, 2012.

[119] Mendelev, M. I., Han, S., Srolovitz, D. J., Ackland, G. J., Sun, D. Y., and Asta, M., "Development of new interatomic potentials appropriate for crystalline and liquid iron," *Philosophical Magazine*, vol. 83, no. 35, pp. 3977–3994, 2003.

[120] Merz, J. F., Small, M. J., and Fischbeck, P. S., "Measuring decision sensitivity: A combined monte carlo - logistic regression approach," *Medical Decision Making*, vol. 12, no. 3, pp. 189–196, 1992.

[121] Metropolis, N., Rosenbluth, A. W., Rosenbluth, M. N., Teller, A. H., and Teller, E., "Equation of state calculations by fast computing machines," *The Journal of Chemical Physics*, vol. 21, no. 6, pp. 1087–1092, 1953.

[122] Metzger, K., Knight, T., and Williamson, R., "Model of u3si2 fuel system using bison fuel code," in *Proceedings of the International Congress on Advances in Nuclear Power Plants–ICAPP 2014, Charlotte, NC*, 2014.

[123] Mills, G. and Jónsson, H., "Quantum and thermal effects in h 2 dissociative adsorption: Evaluation of free energy barriers in multidimensional quantum systems," *Physical review letters*, vol. 72, no. 7, p. 1124, 1994.

[124] Mills, G., Jónsson, H., and Schenter, G. K., "Reversible work transition state theory: application to dissociative adsorption of hydrogen," *Surface Science*, vol. 324, no. 2, pp. 305–337, 1995.

[125] Minervini, L., Zacate, M. O., and Grimes, R. W., "Defect cluster formation in m2o3-doped ceo2," *Solid State Ionics*, vol. 116, no. 3-4, pp. 339–349, 1999.

[126] Minervini, L., Grimes, R. W., and Sickafus, K. E., "Disorder in pyrochlore oxides," *Journal of the American Ceramic Society*, vol. 83, no. 8, pp. 1873–1878, 2000.

[127] Minervini, L., Grimes, R. W., Tabira, Y., Withers, R. L., and Sickafus, K. E., "The oxygen positional parameter in pyrochlores and its dependence on disorder.," *Philosophical Magazine A*, vol. 82, no. 1, p. 123, 2002.

[128] Mishin, Y. and Lozovoi, A., "Angular-dependent interatomic potential for tantalum," *Acta materialia*, vol. 54, no. 19, pp. 5013–5026, 2006.

[129] Morishita, K. and Sugano, R., "Modeling of he-bubble migration in bcc fe," *Nuclear Instruments and Methods in Physics Research Section B: Beam Interactions with Materials and Atoms*, vol. 255, no. 1, pp. 52–56, 2007.

[130] Morris, M. D., "Factorial sampling plans for preliminary computational experiments," *Technometrics*, vol. 33, no. 2, pp. 161–174, 1991.

[131] Mundy, J., Ockers, S., and Smedskjaer, L., "Vacancy migration enthalpy in tungsten at high temperatures," *Philosophical Magazine A*, vol. 56, no. 6, pp. 851–860, 1987.

[132] Nakayama, M. and Martin, M., "First-principles study on defect chemistry and migration of oxide ions in ceria doped with rare-earth cations," *Physical Chemistry Chemical Physics*, vol. 11, no. 17, pp. 3241–3249, 2009.

[133] Nogita, K. and Une, K., "Radiation-induced microstructural change in high burnup uo2 fuel pellets," *Nuclear Instruments and Methods in Physics Research Section B: Beam Interactions with Materials and Atoms*, vol. 91, no. 1-4, pp. 301–306, 1994.

[134] Oaks, A. and Stubbins, J. F., "Kmc clustering model comparison in bcc iron," *Journal of Nuclear Materials*, vol. 442, no. 1, pp. S639–S642, 2013.

[135] Oaks, A., Yun, D., Ye, B., Chen, W.-Y., and Stubbins, J. F., "Kinetic monte carlo model of defect transport and irradiation effects in la-doped ceo2," *Journal of Nuclear Materials*, vol. 414, no. 2, pp. 145–149, 2011.

[136] Odette, G., Alinger, M., and Wirth, B., "Recent developments in irradiation-resistant steels," *Annual Review of Materials Research*, vol. 38, no. 1, pp. 471–503, 2008.

[137] Oh, B. H. and Yang, I. H., "Sensitivity analysis of time-dependent behavior in psc box girder bridges," *Journal of Structural Engineering*, vol. 126, no. 2, pp. 171–179, 2000.

[138] Oh, J.-Y., Koo, Y.-H., and Lee, B.-H., "Simulation of high burnup structure in uo2 using potts model," *Nucl. Eng. Technol*, vol. 41, no. 8, pp. 1109–1114, 2009.

[139] Olander, D., *Fundamental aspects of nuclear reactor fuel elements: solutions to problems*. Jan 1976.

[140] Olsson, P. A., "Semi-empirical atomistic study of point defect properties in {BCC} transition metals," *Computational Materials Science*, vol. 47, no. 1, pp. 135 – 145, 2009.

[141] Pasianot, R. and Ramunni, V., "Small interstitials clusters migration in bcc metals: A molybdenum model," *Computational Materials Science*, vol. 48, no. 4, pp. 783–789, 2010.

[142] Pati, S. and Garde, A., "Fission gas release from pwr fuel rods at extended burnups," in *Proceedings of the American Nuclear Society Topical Meeting on Light Water Reactor Fuel Performance, Orlando, Florida, Aprfl*, pp. 21–24, 1985.

[143] Phillips, A., Janies, D., and Wheeler, W., "Multiple sequence alignment in phylogenetic analysis," *Molecular Phylogenetics and Evolution*, vol. 16, no. 3, pp. 317 – 330, 2000.

[144] Plimpton, S., Battaile, C., Chandross, M., Holm, L., Thompson, A., Tikare, V., Wagner, G., Webb, E., Zhou, X., Cardona, C. G., and others, "Crossing the mesoscale no-mans land via parallel kinetic monte carlo," *Sandia Report SAND2009-6226*, 2009.

[145] Plyasunov, S. and Arkin, A. P., "Efficient stochastic sensitivity analysis of discrete event systems," *Journal of Computational Physics*, vol. 221, no. 2, pp. 724 – 738, 2007.

[146] Pornprasertsuk, R., Ramanarayanan, P., Musgrave, C. B., and Prinz, F. B., "Predicting ionic conductivity of solid oxide fuel cell electrolyte from first principles," *Journal of Applied Physics*, vol. 98, no. 10, pp. 1–2, 2005.

[147] Potts, R. B. and Domb, C., "Some generalized order-disorder transformations," *Proceedings of the Cambridge Philosophical Society*, vol. 48, p. 106, 1952.

[148] Prado-Gonjal, J., Schmidt, R., Espindola-Canuto, J., Ramos-Alvarez, P., and Moran, E., "Increased ionic conductivity in microwave hydrothermally synthesized rare-earth doped ceria ce1xrexo2(x/2)," *Journal of Power Sources*, vol. 209, no. 0, pp. 163–171, 2012.

[149] Prasad, D. H., Kim, H.-R., Park, J.-S., Son, J.-W., Kim, B.-K., Lee, H.-W., and Lee, J.-H., "Superior sinterability of nano-crystalline gadolinium doped ceria powders synthesized by co-precipitation method," *Journal of Alloys and Compounds*, vol. 495, no. 1, pp. 238 – 241, 2010.

[150] Predith, A., Ceder, G., Wolverton, C., Persson, K., and Mueller, T., "*Ab initio* prediction of ordered ground-state structures in $zro_2{-}y_2o_3$," *Phys. Rev. B*, vol. 77, p. 144104, Apr 2008.

[151] Pryde, A. K. A., Vyas, S., Grimes, R. W., Gardner, J. A., and Wang, R., "Cadmium and indium defects in ceria and their interaction with oxygen vacancies and small polarons," *Phys. Rev. B*, vol. 52, pp. 13214–13222, Nov 1995.

[152] Rest, J., "Application of a mechanistic model for radiation-induced amorphization and crystallization of uranium silicide to recrystallization of uo 2," *Journal of nuclear materials*, vol. 248, pp. 180–184, 1997.

[153] Rest, J., "A generalized model for radiation-induced amorphization and crystallization of {U3Si} and {U3Si2} and recrystallization of {UO21}," *Journal of Nuclear Materials*, vol. 240, no. 3, pp. 205 – 214, 1997.

[154] Rest, J., "A model for fission-gas-bubble behavior in amorphous uranium silicide compounds," *Journal of Nuclear Materials*, vol. 325, no. 23, pp. 107 – 117, 2004.

[155] Rest, J., "A model for the influence of microstructure, precipitate pinning and fission gas behavior on irradiation-induced recrystallization of nuclear fuels," *Journal of nuclear materials*, vol. 326, no. 2, pp. 175–184, 2004.

[156] Rest, J., "A model for the effect of the progression of irradiation-induced recrystallization from initiation to completion on swelling of uo 2 and u–10mo nuclear fuels," *Journal of nuclear materials*, vol. 346, no. 2, pp. 226–232, 2005.

[157] Rest, J., "Derivation of analytical expressions for the network dislocation density, change in lattice parameter, and for the recrystallized grain size in nuclear fuels," *Journal of nuclear materials*, vol. 349, no. 1, pp. 150–159, 2006.

[158] Rest, J. and Hofman, G., "Dynamics of irradiation-induced grain subdivision and swelling in u 3 si 2 and uo 2 fuels," *Journal of Nuclear materials*, vol. 210, no. 1, pp. 187–202, 1994.

[159] Rest, J. and Hofman, G., "Effect of recrystallization in high-burnup u0 2 on gas release during ria-type transients," *Journal of nuclear materials*, vol. 223, no. 2, pp. 192–195, 1995.

[160] Rest, J. and Hofman, G., "Dart model for irradiation-induced swelling of uranium silicide dispersion fuel elements," *NUCLEAR TECHNOLOGY*, vol. 126, pp. 88–101, APR 1999.

[161] Rest, J. and Hofman, G., "Irradiation-induced recrystallization of cellular dislocation networks in uranium-molybdenum alloys," in *MRS Proceedings*, vol. 650, pp. R1–7, Cambridge Univ Press, 2000.

[162] Rest, J. and Hofman, G., "An alternative explanation for evidence that xenon depletion, pore formation, and grain subdivision begin at different local burnups," *Journal of nuclear materials*, vol. 277, no. 2, pp. 231–238, 2000.

[163] Rollett, A., Srolovitz, D., Anderson, M., and Doherty, R., "Computer simulation of recrystallizationiii. influence of a dispersion of fine particles," *Acta metallurgica et materialia*, vol. 40, no. 12, pp. 3475–3495, 1992.

[164] Ronchi, C., Sheindlin, M., Staicu, D., and Kinoshita, M., "Effect of burn-up on the thermal conductivity of uranium dioxide up to 100.000 mwdt-1," *Journal of Nuclear Materials*, vol. 327, no. 1, pp. 58–76, 2004.

[165] Rondinella, V. V. and Wiss, T., "The high burn-up structure in nuclear fuel," *Materials today*, vol. 13, no. 12, pp. 24–32, 2010.

[166] Rottler, J., Srolovitz, D. J., and Car, R., "Point defect dynamics in bcc metals," *Phys. Rev. B*, vol. 71, p. 064109, Feb 2005.

[167] Rowinski, M. K., White, T. J., and Zhao, J., "Small and medium sized reactors (smr): A review of technology," *Renewable and Sustainable Energy Reviews*, vol. 44, pp. 643 – 656, 2015.

[168] S. M. Blower, H. D., "Sensitivity and uncertainty analysis of complex models of disease transmission: An hiv model, as an example," *International Statistical Review / Revue Internationale de Statistique*, vol. 62, no. 2, pp. 229–243, 1994.

[169] Sahni, P. S., Grest, G. S., Anderson, M. P., and Srolovitz, D. J., "Kinetics of the q-state potts model in two dimensions," *Phys. Rev. Lett.*, vol. 50, pp. 263–266, Jan 1983.

[170] Sakib Khan, M., Saiful Islam, M., and R. Bates, D., "Cation doping and oxygen diffusion in zirconia: a combined atomistic simulation and molecular dynamics study," *J. Mater. Chem.*, vol. 8, pp. 2299–2307, 1998.

[171] Saltelli, A. and Annoni, P., "How to avoid a perfunctory sensitivity analysis," *Environmental Modelling & Software*, vol. 25, no. 12, pp. 1508 – 1517, 2010.

[172] Satta, A., Willaime, F., and de Gironcoli, S., "First-principles study of vacancy formation and migration energies in tantalum," *Physical Review B*, vol. 60, no. 10, p. 7001, 1999.

[173] Satta, A., Willaimel, F., and de Gironcoli, S., "Vacancy properties in 5d bcc transition metals: Ab initio study at finite electron temperature," in *MRS Proceedings*, vol. 481, p. 189, Cambridge Univ Press, 1997.

[174] Shimomura, Y., Sugio, K., Kogure, Y., and Doyama, M., "Point defects and their clusters in bcc metals," *Computational materials science*, vol. 14, no. 1, pp. 36–42, 1999.

[175] Sizmann, R., "The effect of radiation upon diffusion in metals," *Journal of Nuclear Materials*, vol. 69, pp. 386–412, 1978.

[176] Solomon, J., Alexandrov, V., Sadigh, B., Navrotsky, A., and Asta, M., "Computational study of the energetics and defect clustering tendencies for y- and la-doped {UO2}," *Acta Materialia*, vol. 78, pp. 282 – 289, 2014.

[177] Solomon, J., Navrotsky, A., and Asta, M., "Energetics and defect clustering trends for trivalent rare earth cations substituted in {UO2}," *Journal of Nuclear Materials*, vol. 457, pp. 252 – 255, 2015.

[178] Soneda, N. and De La Rubia, T. D., "Defect production, annealing kinetics and damage evolution in α-fe: an atomic-scale computer simulation," *Philosophical Magazine A*, vol. 78, no. 5, pp. 995–1019, 1998.

[179] Soneda, N., Ishino, S., Takahashi, A., and Dohi, K., "Modeling the microstructural evolution in bcc-fe during irradiation using kinetic monte carlo computer simulation," *Journal of nuclear materials*, vol. 323, no. 2, pp. 169–180, 2003.

[180] Sonoda, T., Kinoshita, M., Ray, I., Wiss, T., Thiele, H., Pellottiero, D., Rondinella, V., and Matzke, H., "Transmission electron microscopy observation on irradiation-induced microstructural evolution in high burn-up uo 2 disk fuel," *Nuclear Instruments and Methods in Physics Research Section B: Beam Interactions with Materials and Atoms*, vol. 191, no. 1, pp. 622–628, 2002.

[181] Spino, J., Cobos-Sabate, J., and Rousseau, F., "Room-temperature microindentation behaviour of lwr-fuels, part 1: fuel microhardness," *Journal of nuclear materials*, vol. 322, no. 2, pp. 204–216, 2003.

[182] Spino, J. and Papaioannou, D., "Lattice parameter changes associated with the rim-structure formation in high burn-up uo 2 fuels by micro x-ray diffraction," *Journal of nuclear materials*, vol. 281, no. 2, pp. 146–162, 2000.

[183] Spino, J., Papaioannou, D., and Glatz, J.-P., "Comments on the threshold porosity for fission gas release in high burn-up fuels," *Journal of nuclear materials*, vol. 328, no. 1, pp. 67–70, 2004.

[184] Spino, J., Rest, J., Goll, W., and Walker, C., "Matrix swelling rate and cavity volume balance of {UO2} fuels at high burn-up," *Journal of Nuclear Materials*, vol. 346, no. 23, pp. 131 – 144, 2005.

[185] Spino, J., Stalios, A., Santa Cruz, H., and Baron, D., "Stereological evolution of the rim structure in pwr-fuels at prolonged irradiation: Dependencies with burn-up and temperature," *Journal of nuclear materials*, vol. 354, no. 1, pp. 66–84, 2006.

[186] Srivastava, M., Kumar, K., Jaiswal, N., Singh, N. K., Kumar, D., and Parkash, O., "Enhanced ionic conductivity of co-doped ceria solid solutions and applications in it-sofcs," *Ceramics International*, vol. 40, no. 7, Part B, pp. 10901–10906, 2014.

[187] Srolovitz, D., Grest, G., and Anderson, M., "Computer simulation of recrystallizationi. homogeneous nucleation and growth," *Acta metallurgica*, vol. 34, no. 9, pp. 1833–1845, 1986.

[188] Srolovitz, D., Grest, G., Anderson, M., and Rollett, A., "Computer simulation of recrystallizationii. heterogeneous nucleation and growth," *Acta metallurgica*, vol. 36, no. 8, pp. 2115–2128, 1988.

[189] Stanek, C. R., Minervini, L., and Grimes, R. W., "Nonstoichiometry in $a_2b_2o_7$ pyrochlores," *Journal of the American Ceramic Society*, vol. 85, no. 11, pp. 2792–2798, 2002.

[190] Tikare, V. and Holm, E. A., "Simulation of grain growth and pore migration in a thermal gradient," *Journal of the American Ceramic Society*, vol. 81, no. 3, pp. 480–484, 1998.

[191] Van Uffelen, P., Konings, R. J., Vitanza, C., and Tulenko, J., "Analysis of reactor fuel rod behavior," in *Handbook of Nuclear Engineering*, pp. 1519–1627, Springer, 2010.

[192] Ventelon, L., Willaime, F., Fu, C.-C., Heran, M., and Ginoux, I., "Ab initio investigation of radiation defects in tungsten: Structure of self-interstitials and specificity of di-vacancies compared to other bcc transition metals," *Journal of Nuclear Materials*, vol. 425, no. 1, pp. 16–21, 2012.

[193] Vincent, E., Becquart, C., and Domain, C., "Ab initio calculations of self-interstitial interaction and migration with solute atoms in bcc fe," *Journal of Nuclear Materials*, vol. 359, no. 3, pp. 227 – 237, 2006.

[194] Voter, A. F., "Classically exact overlayer dynamics: Diffusion of rhodium clusters on rh (100)," *Physical review B*, vol. 34, no. 10, p. 6819, 1986.

[195] Voter, A. F., "Introduction to the kinetic monte carlo method," in *Radiation Effects in Solids*, pp. 1–23, Springer, 2007.

[196] Vyas, S., Grimes, R. W., Gay, D. H., and Rohl, A. L., "Structure, stability and morphology of stoichiometric ceria crystallites," *J. Chem. Soc., Faraday Trans.*, vol. 94, pp. 427–434, 1998.

[197] Wainwright, H. M., Finsterle, S., Jung, Y., Zhou, Q., and Birkholzer, J. T., "Making sense of global sensitivity analyses," *Comput. Geosci.*, vol. 65, pp. 84–94, Apr. 2014.

[198] Wang, T., Qiu, N., Wen, X., Tian, Y., He, J., Luo, K., Zha, X., Zhou, Y., Huang, Q., Lang, J., and others, "First-principles investigations on the electronic structures of u 3 si 2," *Journal of Nuclear Materials*, vol. 469, pp. 194–199, 2016.

[199] Ward, M. and Carpenter, T., "Simulation modeling of the effect of climatic factors on bluetongue virus infection in australian cattle herds. i. model formulation, verification and validation," *Preventive Veterinary Medicine*, vol. 27, no. 1, pp. 1 – 12, 1996.

[200] Was, G. S., *Fundamentals of radiation materials science: metals and alloys*. Springer Science & Business Media, 2007.

[201] Wright, S. A., Plimpton, S. J., Swiler, T. P., Fye, R. M., Young, M. F., and Holm, E. A., "Potts-model grain growth simulations: Parallel algorithms and applications," *SAND Report*, p. 1925, 1997.

[202] Xiao, H. and Long, C., "Modeling of pore coarsening in the rim region of high burn-up {UO2} fuel," *Nuclear Engineering and Technology*, vol. 48, no. 4, pp. 1002 – 1008, 2016.

[203] Xu, W., Zhang, Y., Cheng, G., Jian, W., Millett, P. C., Koch, C. C., Mathaudhu, S. N., and Zhu, Y., "In-situ atomic-scale observation of irradiation-induced void formation," *Nature communications*, vol. 4, 2013.

[204] Zacate, M. O., Minervini, L., Bradfield, D. J., Grimes, R. W., and Sickafus, K. E., "Defect cluster formation in m2o3-doped cubic zro2," *Solid State Ionics*, vol. 128, no. 14, pp. 243 – 254, 2000.

[205] Zha, S., Xia, C., and Meng, G., "Effect of gd (sm) doping on properties of ceria electrolyte for solid oxide fuel cells," *Journal of Power Sources*, vol. 115, no. 1, pp. 44 – 48, 2003.